HOKKAIDO UNIVERSITY

| | |
|---|---|
| Title | Experimental and numerical investigations on cantilever failures for cohesive riverbanks |
| Author(s) | Patsinghasanee, Supapap |
| Degree Grantor | 北海道大学 |
| Degree Name | 博士(工学) |
| Dissertation Number | 甲第12459号 |
| Issue Date | 2016-09-26 |
| DOI | https://doi.org/10.14943/doctoral.k12459 |
| Doc URL | https://hdl.handle.net/2115/67165 |
| Type | doctoral thesis |
| File Information | Supapap_Patsinghasanee.pdf |

Hokkaido University Collection of Scholarly and Academic Papers : HUSCAP

# Experimental and numerical investigations on cantilever failures for cohesive riverbanks

By

Supapap Patsinghasanee

A thesis submitted in partial fulfillment of the requirements for the degree of Doctor of Philosophy in Engineering

Examination Committee: Prof. Yasuyuki Shimizu
Prof. Norihiro Izumi
Prof. Toshihiko Yamashita
Assoc. Prof. Ichiro Kimura

Doctor's Thesis
Division of Field Engineering for Environment
Graduate School of Engineering, Hokkaido University
September 2016

*Dedicated to my beloved family, Paisarn Patsinghasanee, Sarapee Patsinghasanee, Pensri Rattanamusi, Ratda Patsinghasanee, and Wareerat Patsinghasanee*

# ACKNOWLEDGEMENT

This dissertation would not have been possible without the supports, guidance, and encouragements of special people who contributed their assistance in this work.

My first and most earnest acknowledgement must go to my advisor, Associate Professor Ichiro Kimura, for his scientific contributions throughout the work. I wish to express my appreciate to all his contributions of time, ideas, and suggestions. During my experimental work, numerical development, manuscript-writing, and dissertation-writing period, he provided encouragements, valuable suggestions, and lots of good ideas. Additionally, I owe my most sincere gratitude to my supervisor, Professor Yasuyuki Shimizu, for his scientific contributions, sound advices, and laboratory facilities to make my dissertation. Moreover, I also would like to great gratitude to Professor Kazuyoshi Hasegawa, Professor Norihiro Izumi, and Professor Toshihiko Yamashita for their suggestions, comments, advices, and giving me direction.

I would like to thank Dr.Mohamed Nabi and Dr.Tomoko Kyuka for their continuous help, giving me new ideas and discussions. My warm thanks go to Takamasa Todate for assisting me in the experimental measurements.

I am indebted to many colleagues for supporting me during my work. I am grateful to Assistant Professor Tanan Chub-uppakarn and Surat Semmad from Department of Civil Engineering, Prince of Songkla University, Thailand for providing geotechnical data in the U-Tapao River. In addition, I would like to thank Anand Panta for supporting me in the soil mechanics laboratory tests. Furthermore, I am grateful to the Obihiro Regional Office of Hokkaido Development Bureau for providing acceleration sensors using in my experimental works. At this point, I am grateful to the Department of Water Resources, Ministry of Natural Resources and Environment, Bangkok, Thailand for supporting me to study doctoral degree in Hokkaido University. Moreover, I would like to acknowledge other colleagues, whose fruitful discussions.

The financial support for this Ph.D. work came from the Japanese Government Scholarship. I would like to appreciate their support.

My parent and family have been a important motivation for supporting my emotion and moral during my Ph.D. time.

Finally, I am forever indebted to my wife for her understanding, encouragement, motivation, companionship, endless patience, and giving love during whole three years.

# ABSTRACT

Riverbank failure results in extensive sediment production in an alluvial channel, and it can cause severe environmental and economic problems such as loss of fertilization in agriculture areas and destruction of infrastructure. However, because a cantilever failure involves a rapid channel widening and delivers a large volume of sediment into a channel, such a failure is a serious issue in a river engineering. Difference types of riverbank failures have been investigated in the previous studies, but these works have limitations in understanding the complex mechanisms of cantilever failure regarding the coupling of fluvial erosion with that failure. Elucidating the underlying mechanism of a cantilever failure by means of experimental works and numerical studies are therefore the challenging tasks for complete understanding of fluvial erosion, cantilever failure, slump block effect, and bedload sedimentation along an alluvial channel.

Firstly, the simple bank failure model was employed to simulate bank failure and bed deformation, using a two dimensional depth-averaged model and an equilibrium sediment transport model, for homogeneous and heterogeneous grain size conditions. Moreover, the numerical conditions were similar with those used in the previous experimental works. The numerical models under homogeneous and heterogeneous conditions can reproduce the experimental results using an appropriate angle of repose and a suitable transversal grid size. For homogeneous condition, the temporal changes in an averaged cross-sectional profile over longitudinal direction were in a relatively good agreement with the experimental results. However, the numerical results of the bed deformation were not satisfactory in heterogeneous condition. The main reason is that the armoring effect is developed to reinforce the top layer of bank-toe in the experimental results but the simple bank failure model is limited in its ability to simulate the armoring effect.

Next, the cantilever failure mechanisms were investigated by means of small-scale experiments and numerical modeling. In laboratory experiments, three types of cohesive materials with different percentages of silt-clay content were carried out in seven cases by varying the hydraulic conditions. The small-scale experiments showed that fluvial erosion of the submerged zone progressively undermines the riverbank during the initial stage of a cantilever failure. Tension cracks then develop at the upper surface of the cohesive banks and beam-type failure occurs thereafter. Moreover, the numerical modeling of a cantilever failure implemented by a triple-grid approach within the framework of fluvial erosion and the cantilever's subsequent failure were validated by the small-scale experimental results. The simulated results showed good agreement with the small-scale experimental results in terms of spatial-averaged bank width and water level along cohesive banks. Additionally, the small-scale experimental results were compared to both the failure mechanisms of the cantilever failure model and simple bank failure model. The comparisons showed that the simple bank failure model cannot reproduce the complex mechanism of cantilever failure regarding the limitation of the coupling failure mechanisms.

After that, the previous empirical and analytical equations of the actual shear stress, critical shear stress, erodibility coefficient, and factor of safety of shear-type and beam-type failures were employed to validate the temporal variations of spatially averaged bank width, overhanging block dimensions, and dominant cantilever failure type with the existing small-scale experimental works and the U-Tapao River, Thailand. For fluvial erosion, the actual shear stresses of the small-scale experimental works range from 0.68 to 1.23 Pa, whereas those of the U-Tapao River are within the range of 18.51 to 22.52 Pa. Moreover, the critical shear stresses estimated by the percentage of silt-clay content of

the small-scale experimental banks are within the range of 0.38 to 0.57 Pa, whereas those of the U-Tapao River range from 9.44 to 12.99 Pa. Additionally, a comparison results of the erodibility coefficient between the previous relationships with the small-scale experimental results and U-Tapao River showed a poor agreement. Therefore, the relationship between the erodibility coefficient and critical shear stress are needed to be measured locally. For overhanging block stability, the results showed that the dominant cantilever failure mechanisms of the experiment and the U-Tapao River are the beam-type and shear-type failure, respectively. Furthermore, the comparison results of the temporal variations of spatially averaged bank width between the numerical and small-scale experimental results illustrated a high degree of confidence. Significant errors occurred after the cantilever failure stage because the failure material was dropped into the channel and protected against further fluvial erosion at the bank-toe. Therefore, the slump block effect must be considered in the new numerical modeling. In addition, the numerical results of the U-Tapao River can reproduce the accurate dominant failure mechanism and overhanging block dimensions in terms of width and height.

Finally, to deal with the limitations of the previous small-scale experimental works and numerical studies of the process of a cantilever failure with the slump block effect, a series of large-scale experimental works were conducted with the objective to fully understand the complex mechanism of a cantilever failure by considering the geometrical and material scaling, and sidewall correction effect. Additionally, the slump block failures during the progress of a cantilever failure and its decomposition phenomena were discussed in the laboratory experiments. Moreover, a novel coupled numerical model by considering the effect of fluvial erosion, cantilever failure, slump block, and bedload sedimentation was developed to simulate the cantilever failure mechanism. The large-scale experimental results expressed that fluvial erosion at the submerged zone generates an overhanging block in the upper part of the cohesive banks. Tension cracks then developed on the upper surface of the cohesive banks, and the cantilever failure after that occurs along the tension crack line. The dominant failure mechanism was observed to be beam-type failure, which was clarified by using the acceleration sensors installed inside the cohesive banks. In addition, the large-scale experimental results indicated that cohesive banks with higher silt-clay contents are more susceptible to failure than those with lower silt-clay contents. Moreover, slump blocks were observed on the bed channel in front of the bank, where they formed a sediment buffer that reinforced banks and reduced fluvial erosion. The slump block phenomena for the formation and deformation showed a significant effect on the cohesive force of the banks and affected the bank geometry. Therefore, a reduction of the silt-clay content leads to smaller slump block dimensions as well as faster decomposition. The relationship between the slump block volumes and their decomposition times in the this large-scale experimental study seems to be almost random, without any identifiable rules governing this phenomena. Furthermore, the numerical model with slump block effect satisfactorily reproduced the fluvial erosion, cantilever failure, and bank protection by the slump blocks. Additionally, the numerical results showed good agreement with the large-scale experimental results in terms of the spatial-averaged bank width. On the other hand, the numerical results without slump block effects showed the excessive fluvial erosion and cantilever failure rates more than the large-scale experimental results. Therefore, the effect of the bank protection due to the slump block were clearly demonstrated in this study. In addition, this study can conclude that this numerical model is a powerful tool to analyze and predict the complex mechanism of a cantilever failure with slump blocks.

# TABLE OF CONTENTS

DEDICATION i

ACKNOWLEGEMENTS ii

ABSTRACT iii

TABLE OF CONTENTS v

LIST OF TABLES ix

LIST OF FIGURES x

CHAPTER 1 INTRODUCTION 1

1.1 PROBLEM AND CHALLENGES 1

1.2 OPEN QUESTIONS AND REFINED OBJECTIVE OF THIS WORK 4

1.3 THESIS OUTLINE 6

CHAPTER 2 COMPUTATIONAL MODELING OF THE SIMPLE BANK FAILURE BY A TWO DIMENSIONAL DEPTH AVERAGED MODEL UNDER HOMOGENEOUS AND HETEROGENEOUS CONDITIONS 9

2.1 INTRODUCTION 9

2.2 GOVERNING EQUATIONS 10

2.2.1 Flow Equations 10

2.2.2 Equilibrium Sediment Transport Equations 11

2.2.3 Simple Bank Failure Model 13

2.2.4 Computational Procedures 14

2.3 RESULTS AND DISCUSSION 15

2.3.1 The Existing Experiment Flume Conditions 15

2.3.2 The Optimization Results for the Angle of Repose 15

2.3.3 The Results of Transversal Grid Sensitivity Analysis and Simulation Time 17

2.3.4 The Computational Results of Riverbank Failure 19

2.4 SUMMARY 23

CHAPTER 3 CANTILEVER FAILURE INVESTIGATIONS FOR COHESIVE RIVERBANKS 26

3.1 INTRODUCTION 26

3.2 METHODOLOGY 27

3.2.1 Experimental Setup 27

3.2.2 Numerical Model 31

3.2.2.1 Fluvial erosion 31

3.2.2.2 Cantilever failure 35

3.2.2.3 Bedload transport and bed deformation 36

3.3 RESULTS AND DISCUSSION 37

3.3.1 Experimental Results 37

3.3.2 Numerical Results 38

3.3.3 Discussion 43

3.4 SUMMARY 45

CHAPTER 4 COUPLED STUDIES OF FLUVIAL EROSION AND CANTILEVER FAILURE FOR COHESIVE RIVERBANKS: CASE STUDIES IN THE EXPERIEMNTAL FLUMES AND U-TAPAO RIVER 47

4.1 INTRODUCTION 47

4.2 METHODOLOGY 48

4.2.1 Laboratory Experiment 48

4.2.2 The U-Tapao River 51

4.2.3 The Coupled Study of Fluvial Erosion and Cantilever Failure 51

4.2.3.1 Fluvial erosion 53

4.2.3.2 Cantilever failure 58

4.2.3.3 Bedload transport and bed deformation 59

4.3 RESULTS AND DISCUSSION 60

4.3.1 Overhanging Block Properties 60

4.3.2 Fluvial Erosion 61

4.3.3 Cantilever Failure 62

4.3.4 Numerical Results 66

4.4 SUMMARY 69

CHAPTER 5 EXPERIMENTAL INVESTIGATION ON CANTILEVER FAILURES FOR COHESIVE RIVERBANKS 71

5.1 INTRODUCTION 71

5.2 METHODOLOGY 72

5.3 RESULTS 75

5.3.1 Case 1 79

5.3.2 Case 2 80

5.4 DISCUSSION 81

5.5 SUMMARY 85

CHAPTER 6 NUMERICAL SIMULATION OF A CANTILEVER FAILURE WITH THE EFFECT OF SLUMP BLOCKS FOR COHESIVE RIVERBANKS 86

6.1 INTRODUCTION 86

6.2 METHODOLOGY 87

6.2.1 Fluvial Erosion Rate 89

6.2.2 Cantilever Failure 92

6.2.3 Slump Block Effect 93

6.2.4 Bedload Transport and Bed Deformation 94

6.3 RESULTS AND DISCUSSION 95

6.4 SUMMARY 100

CHAPTER 7 CONCLUSIONS AND SUGGESTIONS FOR FUTURE RESEARCH 101

7.1 CONCLUSIONS 101

7.2 SUGGESTIONS FOR FUTURE RESEARCH 103

7.2.1 Laboratory Measurement 103

7.2.2 Numerical Modeling 103

APPENDIX A- PUBLICATION LISTS 104

REFERENCES 106

# LIST OF TABLES


Table 2.1 The existing experiment flume conditions. 17

Table 3.1 Summary of experimental conditions. 29

Table 3.2 Summary of the failure time and failure block dimensions. 40

Table 4.1 Summary of the existing experimental conditions. 50

Table 4.2 Coordinates of the study sites in the U-Tapao River. 51

Table 4.3 Properties, actual shear stress, critical shear stress, erodibility coefficient, and factor of safety of the reference overhanging blocks of the experimental cohesive banks. 63

Table 4.4 Properties, actual shear stress, critical shear stress, erodibility coefficient, and factor of safety of the reference overhanging blocks of the U-Tapao River. 64

Table 5.1 Summary of the large-scale experimental conditions. 74

Table 5.2 Acceleration sensor specifications. 75

Table 5.3 Summary of failure times, failure block dimensions, failure block volumes and decomposition times (Case 1). 80

Table 5.4 Summary of failure times, failure block dimensions, failure block volumes and decomposition times (Case 2). 81

Table 6.1 Summary of the existing large-scale experimental conditions. 96

# LIST OF FIGURES


**Fig. 1.1** (a) Fluvial erosion at the bank-toe in the formation of overhanging failure block of the Kordan River, Iran. (b) Destruction of the overhanging block from cantilever failure. 1

**Fig. 1.2** Cantilever failure and destruction of the overhanging block of four cross-sectional data of the U-Tapao River, Thailand. 2

**Fig. 1.3** The three types of possible cantilever failure. 5

**Fig. 1.4** The framework of research and its correspondence of each chapter. 8

**Fig. 2.1** A simplified bank failure process. 14

**Fig. 2.2** A simplified bank failure model (Nakanishi et al., 2005). 16

**Fig. 2.3** The grain size distribution of heterogeneous condition. 16

**Fig. 2.4** The optimization results of angle of repose in homogeneous (Case 2) and heterogeneous (Case 5) conditions. 18

**Fig. 2.5** The results of transversal grid sensitivity analysis. 19

**Fig. 2.6** The results of computational time in difference transversal grid size. 19

**Fig. 2.7** The comparison results between numerical computation and experimental data in homogeneous condition. 21

**Fig. 2.8** The comparison results between numerical computation and experimental data in heterogeneous condition. 22

**Fig. 2.9** The dimensionless shear stress profile of heterogeneous condition. 24

**Fig. 2.10** The mean diameter profile of armoring effect in heterogeneous condition. 25

**Fig. 3.1** The dimensions of experimental flume. 28

**Fig. 3.2** Direct shear test results of cohesive materials. 30

**Fig. 3.3** Framework of triple-grid approach of cantilever failure model. 32

**Fig. 3.4** Overhanging geometry and forces exerted on the incipient failure block. 32

**Fig. 3.5** Logic diagram of the computational sequence. 33

**Fig. 3.6** Two schemes used to adopt the boundary nodes by the effect of fluvial erosion (a) unmodified boundary nodes; (b) modified boundary nodes. 35

**Fig. 3.7** Experimental image results of spatial bank width in Case 6. 38

**Fig. 3.8** Schematic diagrams of spatial bank width. 39

**Fig. 3.9** Cross-sectional views of fluvial erosion and beam-type failure mechanism of Case 3. (Zone I, II and III are water, failure material and cohesive riverbank, respectively.) 41

**Fig. 3.10** Comparison of numerical results and spatially averaged experimental results. 42

**Fig 3.11** Validation results for spatial bank width in Case 6. 43

**Fig 3.12** Validation results for spatial water level in Case 6. 44

**Fig 3.13** Comparison results between the experimental and numerical results with the different cohesive force of Case 3 (SC = 30%) and Case 5 (SC = 20%). 46

**Fig. 4.1** Dimensions of a straight experimental channel. 49

**Fig. 4.2** Experimental image results and schematic diagrams of temporal bank width of Case 5. 50

**Fig. 4.3** Study locations along the U-Tapao River, Songkhla Province, Thailand. 52

**Fig. 4.4** Grain size distribution of UT.3. 53

**Fig. 4.5** Framework of triple-grid approach of a coupling model. 54

**Fig. 4.6** Overhanging geometry and forces exerted on the incipient failure block in a coupling model. 54

**Fig. 4.7** Logic diagram of the computational sequence of the coupled modeling. 55

**Fig. 4.8** Illustration of the two schemes used to adopt the boundary nodes by the effect of fluvial. 58

**Fig. 4.9** Relationship between overhanging block height and overhanging block width at the critical failure stage. 65

**Fig. 4.10** Cross-sectional views of fluvial erosion and beam-type failure mechanism at two time stages for Case 5. 67

**Fig. 4.11** Validation results of the temporal variations of spatially averaged bank width. 68

**Fig. 5.1** Dimensions of the large-scale experimental channel. 73

**Fig. 5.2** Example results of data interpretations in Case 1. 76

**Fig. 5.3** Example results of the experimental works in Cases 1 and 2. 77

**Fig. 5.4** Schematic diagrams of spatial bank width in Cases 1 and 2. 78

**Fig. 5.5** Example results of Case 2 (SC = 20%) using the acceleration sensors. 79

**Fig. 5.6** Comparison results of fluvial erosion rate in the experimental studies with the different silt-clay contents. 83

**Fig. 5.7** Variation of slump block dimensions with the different cohesive forces. 83

**Fig. 5.8** Slump decomposition of the various volumes with the different cohesive forces. 84

**Fig. 5.9** Armoring effect of the experimental results (Case 2). 84

**Fig. 6.1** Framework of triple-grid approach of cantilever failure model with the slump block consideration. 88

**Fig. 6.2** Overhanging geometry with the slump block consideration and forces exerted on the incipient failure block. 88

**Fig. 6.3** Slump block locations and dimensions. 89

**Fig. 6.4** Logic diagram of the computational sequence of a cantilever failure with slump block effect. 91

**Fig. 6.5** Illustration of the two schemes used to adopt the boundary nodes by the effect of fluvial erosion. 92

**Fig. 6.6** Comparison between numerical and experimental results in the streamwise averaged bank width. 97

**Fig. 6.7** Riverbank geometry of the numerical results. 97

**Fig. 6.8** Comparison of spatial-averaged bank width with and without slump block consideration, together with the experimental results. 98

**Fig. 6.9** Cross-sectional views of computational results in Case 1 with slump block effect (a and c), and without slump block effect (b and d) (brown: undisturbed cohesive material, gray: non-cohesive bedload, blue: water). 99

# Chapter 1

# INTRODUCTION

## 1.1 PROBLEM AND CHALLENGES

Schumm (1971) has classified the natural rivers into two major types depended on their freedom to change the channel geometries. The first type is bedrock channels, which are formed by rock outcrops on the bed channel and riverbanks. The another type is alluvial channels, which are free to deform their dimensions, shapes, patterns and gradients. Alluvial channels are composed of cohesive and non-cohesive sediments that are eroded and transported by flow on the bed channel and riverbanks. Therefore, the alluvial channels are high susceptibility on the lateral migration (Hagerty et al., 1985; Hooke, 1980; Schumm, 1985). It means that the occurrence of the riverbank failure are more active in the alluvial channels than the bedrock channels.

Riverbank failure is a key process in the river morphodynamics, affecting a wide range of physical, ecological and socioeconomic issues in an alluvial channel, for instance, a loss of agriculture areas and destruction of infrastructures (Rinaldi & Darby, 2008; Rinaldi et al., 2008), turbidity problems (Eaton et al., 2004) and sediment, nutrient, and contaminant problems (Reneau et al., 2004). However, because a cantilever failure involves a rapid channel widening and delivers a large volume of sediment into an alluvial channel, such a failure is a serious issue in a river engineering (Dapporto et al., 2003; Nardi et al., 2012; Taghavi et al., 2010) as shown the cantilever failures along the natural rivers in **Figs. 1.1 and 1.2**. Elucidating the underlying mechanism of cantilever failure, and numerical modeling are therefore important for a complete understanding of fluvial erosion and cantilever failure with slump block effect along an alluvial channel before any new construction works such as ripraps, gabions, mattresses and pipeline crossing.

(a) (b)

**Fig. 1.1** (a) Fluvial erosion at the bank-toe in the formation of overhanging failure block of the Kordan River, Iran. (b) Destruction of the overhanging block from cantilever failure.

(Samadi et al., 2013)

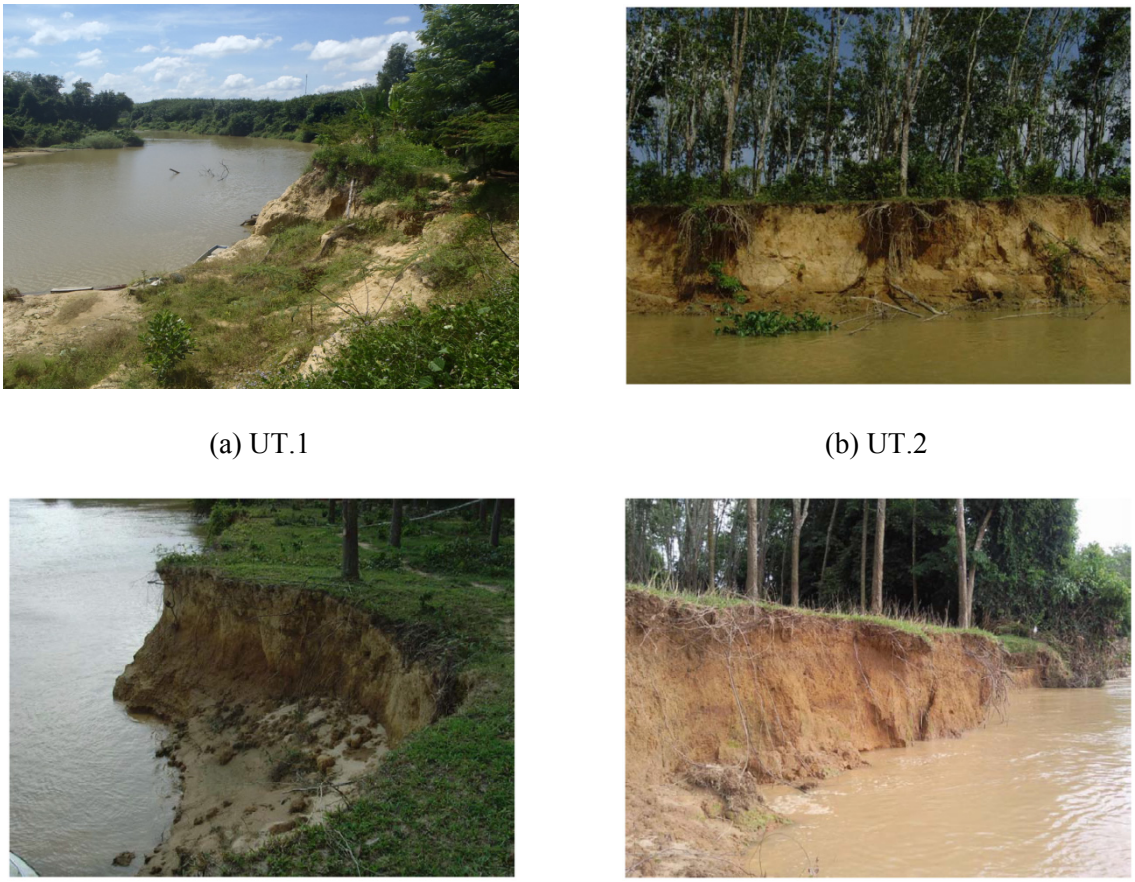

(a) UT.1 (b) UT.2

(c) UT.3 (d) UT.4

**Fig. 1.2** Cantilever failure and destruction of the overhanging block of four cross-sectional data of the U-Tapao River, Thailand. (Semmad, 2010)

In terms of riverbank stability analyses, previous researchers have been unable to analyze cantilever failure and have focused mainly on simple bank failures. This is defined as the ratio between stabilizing and destabilizing forces, such as rotational slip failure, toppling failure, planar failure and mass wasting failure (ASCE, 1998; Daun, 2005; Osman & Thorne, 1988). Additionally, estimations of the failure plane angle and tension crack depth have been analyzed using a combination of field and experimental data (Taghavi et al., 2010). A limited number of studies have applied stability analyzes based on the safety factor of portion with cantilever failure. From this, three types of possible cantilever failure mechanisms — shear-type, beam-type, and tensile-type failures — have been defined (Abam, 1997; Thorne & Tovey, 1981). Moreover, the effects of the potential presence of water within tension crack, pore water and hydrostatic confining pressures were accounted for in the stability analysis of overhanging block in the shear-type failure (Samadi et al., 2011). In addition, the functions of compressive strength and tensile strength were taken into account for the beam-type failure based on the Thorne and Tovey's formula (Thorne & Tovey, 1981) derived by Micheli & Kirchner (2002). Furthermore, the tensile strength equation on the tension crack at the failure time was expressed in the terms of the overhanging block weight and geometrical dimensions (Fukuoka, 1994). For cantilever failure mechanism, shear-type failure is dominated by the shear stress along the vertical failure plane. Such failure is expected to occur when the shear stress along the failure plane from the weight of the overhanging block ($W$) exceeds the resisting force (cohesive force, $C$), as shown in **Fig. 1.3(a)**. Additionally, beam-type failure is related to the unstable overhanging blocks by

rotation from the cohesive riverbank forward into the channel. This occurs when the rotational moment at the neutral axis from the weight of the block subject to overhanging failure exceeds the restoring moment of cohesive force as illustrated in **Fig. 1.3(b)**. Moreover, tensile-type failure across a horizontal plane at some height above the base causes the lower part of the overhanging block to fall away as shown in **Fig. 1.3(c)**. This occurs when the tensile stress due to weight of the lower part of the overhanging block overcomes the tensile strength of the cohesive riverbank.

Several previous experimental works have reported small-scale cantilever failure experiments, including experimental works examining fluvial erosion rate and cantilever mechanisms (Fukuoka et al., 1999), investigating flow velocity and fluvial erosion rate (Fukuoka et al., 2000) and measuring flow characteristics near and inside eroded cantilever riverbank (Bahar & Fukuoka, 2002). Experimental works on the failure mechanism of cantilevers have also been reported in the large-scale experimental works, which are considered as the scale and sidewall correction effects. For instance, an experimental work of curved natural channels with the artificial overhanging block were conducted to determine the flow characteristics, fluvial erosion rate, and bed deformation (Fukuoka et al., 1996). Additionally, Nardi et al., (2012) carried out experimental works to investigate mass wasting failure in the sandy gravel riverbank and showed the occurrence of a variety of failure processes, such as cantilever, slap, and side failures. Samadi et al., (2013) conducted the experimental studies to determine the dominant cantilever failure mechanisms, which were found to be the beam-type and tensile-type failures. Moreover, Francalanci et al., (2013) carried out the experimental works to observe the riverbank retreat processes during the tidal cycle and showed the varieties of processes including particle erosion, cantilever failure, and slide failure. However, the recent large-scale experiments (Francalanci et al., 2013; Nardi et al., 2012; Samadi et al., 2013) focused solely on processes related to cantilever failures and the interaction between stagnant water and cohesive materials; fluvial erosion was not taken into account.

Previous numerical works have studied riverbank failure mechanisms by using simple bank failure models (ASCE, 1998; Iwasaki et al., 2012; Jang & Shimizu, 2005; Nagata et al., 2000). In addition, a coupled model of fluvial erosion and mass wasting failure was developed to reproduce fluvial erosion in the bank-toe, degradation in bed channel, and destabilization by only considering shear-type failure of an upper bank (Darby et al., 2007; Duan & Julien, 2010; Langendoen et al., 2008; Motta et al., 2014; Rinaldi et al., 2008).

For cantilever failure modeling, several numerical models have been developed to gain an understanding of the complex mechanisms of cantilever failure. For example, Bahar & Fukuoka (2002) developed two-dimensional depth-averaged model using the semi-implicit method, applying a pressure-link equation algorithm to reproduce flow characteristics near and inside eroded riverbank. Recently, shear-type and beam-type failure mechanisms were studies to identify the significant effects of uncertainty parameters on the reliability of a riverbank stability model in determining a cantilever failure. The results showed that the overhanging block dimensions and the cohesive force are highly significant for an analysis of cantilever stability (Samadi et al., 2011). A stress-strain behaviour model for a cantilever failure was also applied to simulate the subsequent failure of an overhanging block by limited equilibrium method, which is defined as the ratio between stabilizing and destabilizing forces (Samadi et al., 2013). Following cantilever failure, the overhanging blocks crumble down in a shape like slump blocks and cover the bank-toe. It is thought that the fluvial erosion rate decreased as a result of the failure of slump blocks (Crosato, 2008; Dulal et al., 2010). The simplified process of slump blocks was developed for reproducing the meandering evolution process in small-scale experiments (Dulal et al., 2010) and natural rivers (Langendoen et al., 2008; Motta et al., 2014; Parker

et al., 2011). These previous studies employed the simple bank failure concept with the slump block effect based on submerged angle of repose. In such model, when the riverbed near the riverbank erodes and the cross sectional gradient of the riverbank slope becomes steeper than the angle of repose, the slump block is assumed to be generated. Follow this, the slump block is deposited at the bank-toe and the riverbank is then armored. However, these previous studies have limitations in coupling fluvial erosion with cantilever failure and simulations coupling fluvial erosion and cantilever failure therefore need to be conducted.

To deal with the limitations of the previous experimental works and numerical studies of the process of a cantilever failure, a series of small-scale and large-scale experimental works were conducted with the objective to fully understand the complex mechanism of a cantilever failure. Moreover, a novel coupled numerical model by considering the effect of fluvial erosion, cantilever failure, slump block, and bedload sedimentation was developed to simulate the cantilever failure mechanism.

## 1.2 OPEN QUESTIONS AND REFINED OBJECTIVE OF THIS WORK

The challenges of the underlying mechanism of cantilever failure by means of the experimental works and numerical modeling for cohesive riverbanks can be divided into three groups, namely process understanding, theory and numerical modeling. Basically, elucidating the underlying mechanism of the coupling process of fluvial erosion, cantilever failure, slump block effect and bedload sedimentation for cohesive riverbanks is the challenging issues in all three mentioned disciplines.

Under the process understanding, further research is required on the following issues:

- Fluvial erosion process and its interaction between flow and cohesive riverbank,
- Riverbank failure processes (including undermining the cohesive riverbanks, tension crack, tension crack location and cantilever failure), their interaction in respect to flow, riverbank geometry, silt-clay content and water content,
- Deposition, decomposition and distribution of failed riverbank material (slump block) at the bank-toe in fort of the cohesive riverbanks.

In the theory of the coupling fluvial erosion and cantilever failure for cohesive riverbanks proper answers should be proposed for the following questions:

- How to include the effects of the riverbank geometry, flow, cohesive material properties in the analysis of a cantilever failure?
- Are the existing analytical approaches and empirical equations sufficient to analyze fluvial erosion, cantilever failure, slump block effect and bedload sedimentation and determine the critical overhanging block dimensions for cohesive riverbanks?

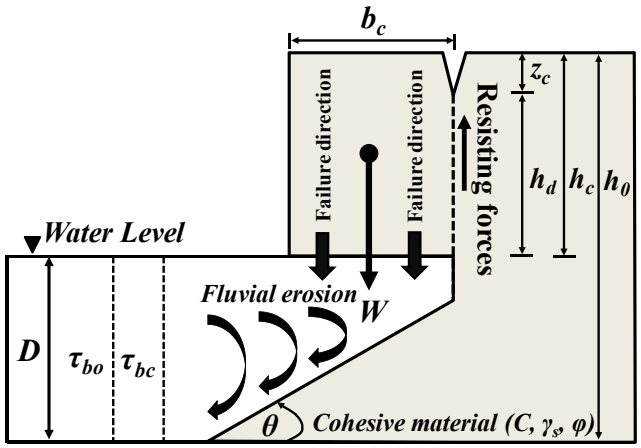


(a) Shear-type failure.

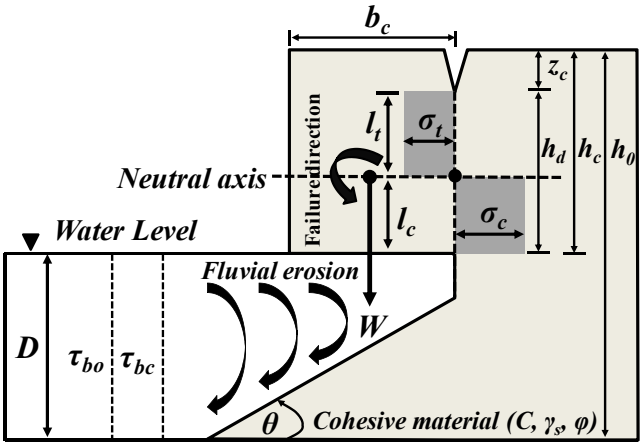


(b) Beam-type failure.

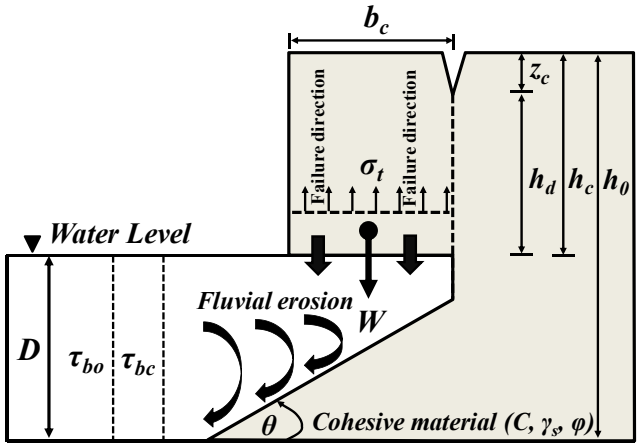


(c) Tensile-type failure.

**Fig. 1.3** The three types of possible cantilever failure. $h_0$ is the initial bank height (m), $h_c$ is the overhanging block height (m), $h_d$ is the effective length of vertical failure surface (m), $b_c$ is the overhanging block width (m), $z_c$ is the tension crack depth (m), $D$ is the water depth (m), $\tau_{bo}$ and $\tau_{bc}$ are the actual shear stress and critical shear stress (Pa), $l_t$ and $l_c$ are the tensile zone length and compressive zone length (m), $W$ is the overhanging block weight (kN), $\sigma_t$ and $\sigma_c$ are the tensile stress and compressive stress (kN/m$^2$), $\theta$ is the angle of repose, $C$ is the cohesive force (Pa), $\phi$ is the internal friction angle, and $\gamma_s$ is the unit weight of soil (kN/m$^3$).

Cantilever failure modeling encounter the main following challenges:

- Proper coupling modeling of cantilever failure for cohesive riverbanks including the effect of fluvial erosion, cantilever failure, mesh adaptation, slump block effect and bedload sedimentation,

- Simulation of fluvial erosion (undercutting), tension crack, cantilever failure, slump block decomposition, bedload transport and bed deformation.

This dissertation is to investigate the main physical processes of cantilever failure for cohesive riverbanks. To address the gap between experiments and numerical modeling of the process of a cantilever failure, experimental studies and numerical model were developed by considering the effect of fluvial erosion, cantilever failure, slump block and bedload sedimentation.

The objectives of this dissertation can be described as follow:

1) Developing and validating a 2D depth-averaged model that is able to simulate simple bank failure model under homogeneous and heterogeneous conditions for understanding the fundamental concept of riverbank failure.

2) Assessing the underlying complex mechanisms of cantilever failure by means of experimental study using cohesive materials classified on the basis of their percentage of silt-clay content and water content and investigating the effects of cohesive properties of the fluvial erosion, cantilever's subsequent failure, and slump block effect.

3) Analyzing the overhanging block properties (e.g., overhanging block dimension and geotechnical parameters), fluvial erosion rate and dominant failure mechanism of the experimental scale, and the natural river (the U-Tapao River, Songkhla Province, Thailand) using the previous empirical and analytical equations.

4) Developing and validating a numerical model of a coupling fluvial erosion and cantilever failure with the slump block effect for the cohesive riverbanks. This numerical approch involves applying for four submodels — fluvial erosion, cantilever failure, slump block, and bedload sedimentation — at each of a series of discrete timesteps. However, the effect of other parameter such as pore water pressure, seepage gradient force, and secondary currents is assumed to be negligible.

## 1.3 THESIS OUTLINE

The dissertation is consisted of seven chapters. The framework of this dissertation and its correspondence of each chapter is shown in **Fig. 1.4.** The synopsis of each chapter is described as follows:

In Chapter 1, the main problems and challenges of cantilever failure for cohesive riverbanks are expressed by the ambiguities and limitations of previous experimental studies and numerical modeling. The open questions and main objectives of this dissertation are also described.

In Chapter 2, this chapter is focused on numerical modeling of bed deformation and riverbank failure model under unsteady flow using a 2D depth-averaged model on a curvilinear boundary-fitted coordinate system, a sediment transport model, and a simple bank failure model for homogeneous and

heterogeneous conditions. The numerical conditions were similar with the previous experimental conditions under homogeneous and heterogeneous conditions. The purpose of this numerical modeling is to understand the simple riverbank failure mechanism of non-cohesive material. The numerical results and effect of both grain size conditions are discussed.

In Chapter 3, this chapter elucidates the mechanisms of cantilever failure by means of laboratory experiments and numerical modeling. In the laboratory experiments, the small-scale experimental studies related to fluvial erosion and cantilever failure were carried out using fixed bed in a straight rectangular channel with Plexiglas walls to allow for real-time observation and recording. Three types of cohesive materials with different percentages of silt-clay content were investigated in seven cases by varying the hydraulic condition. Furthermore, the novel numerical modeling of a cantilever failure implemented by a triple-grid approach, consisting of a coarse 1D grid for flow field in the lateral direction, a fine 1D grid for sediment transport and bed deformation in the lateral direction, and a 2D grid for cantilever failure in the vertical and lateral directions, was validated by the small-scale experimental results.

In Chapter 4, the purpose of this chapters is to introduce new coupling processes for simulating the fluvial erosion and cantilever failure of the small-scale experimental studies (Chapter 3) as well as the natural riverbanks at the U-Tapao River, Thailand. The new numerical modeling employed the previous empirical and analytical equations of the actual shear stress, critical shear stress, erodibility coefficient, factor of safety of shear-type failure and factor of safety of beam-type failure to determine the fluvial erosion rate and overhanging block stability in the existing small-scale experiments and the U-Tapao River. Furthermore, the existing numerical model (Chapter 3) was modified by the appropriate equations and new mesh adaptation scheme. Moreover, the new numerical model was validated with the temporal variations of spatially averaged bank width of the existing small-scale experimental studies and the U-Tapao River.

In Chapter 5, this chapter presents an large-scale experimental study of coupling fluvial erosion and cantilever failure with the slump block effect for cohesive banks by considering the geometrical and material scaling, and sidewall correction effect. Two types of cohesive materials with different percentages of silt-clay content were investigated under similar hydraulic conditions using high-resolution video cameras and acceleration sensors to clarify failure mechanism. The slump block formation and decomposition were the new phenomena observed in this experiments. Furthermore, the effect and role of the slump block on cantilever failure were described for the first time at the experimental scale on channel flow.

In Chapter 6, the slump block effect in coupling fluvial erosion and cantilever failure was considered for developing a numerical modeling of a cantilever failure that uses a triple-grid approach to simulate the behavior of a cantilever within the framework of fluvial erosion, the cantilever's subsequent failure, slump block effect and bedload sedimentation. Two cases of cohesive materials with the different percentages of silt-clay content (Chapter 5) were simulated under the similar hydraulic conditions with and without slump block consideration. Additionally, the effect of slump block consideration were expressed and discussed in this chapter.

In Chapter 7, the conclusions and suggestions for future research are stated.

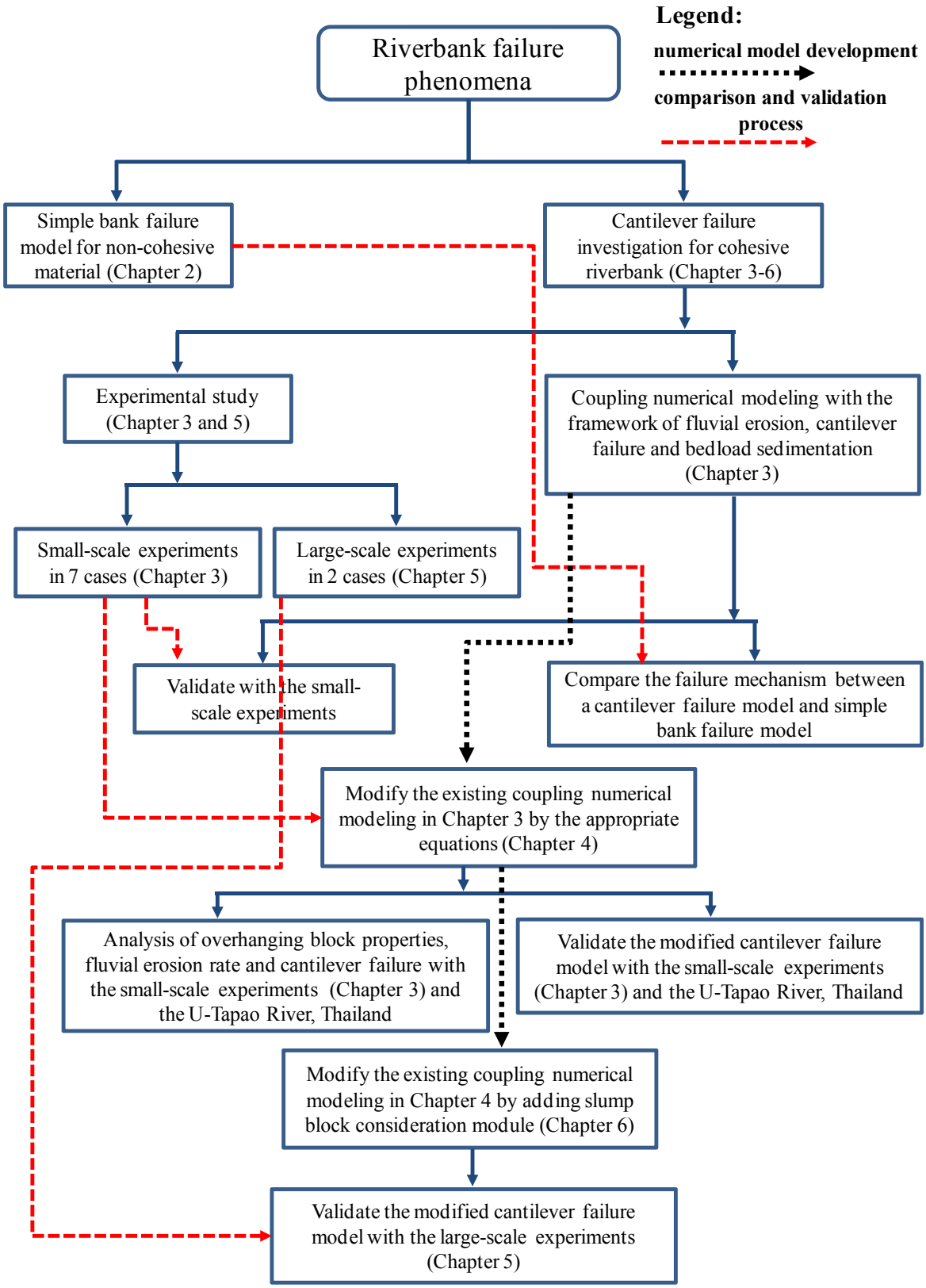


**Fig. 1.4** The framework of research and its correspondence of each chapter.

# Chapter 2

# COMPUTATIONAL MODELING OF THE SIMPLE BANK FAILURE BY A TWO DIMENSIONAL DEPTH AVERAGED MODEL UNDER HOMOGENEOUS AND HETEROGENEOUS CONDITIONS

## 2.1 INTRODUCTION

Many river engineering problems have been caused by riverbank failure and bed deformation in the alluvial channels. These are important mechanisms by which a channel width adjustment, riverbank geometry change, and slope convey water and sediment supplied to an alluvial channel. Therefore, an effective prediction of riverbank failure and bed deformation is urgent issues to understand the complicated alluvial channel mechanism.

In channel development processes, several researchers have concerned the riverbank failure and bed deformation using theoretical study such as the analytical stability analysis of steep riverbanks, the concept of critical shear stress of riverbank erosion, and the riverbank retreat mechanism caused by fluvial erosion and mass wasting under gravity. For instance, Osman & Thorne (1988) have analyzed slope stability in steep slopes for calculating lateral erosion and predicting riverbank stability. ASCE (1998) have considered the riverbank retreat mechanism caused by fluvial erosion and mass wasting under gravity. Moreover, the previous studies motioned that the temporal and spatial averaged boundary shear stress are important parameters for predicting the equilibrium of channel width (ASCE, 1998; Osman & Thorne, 1988).

The previous simple bank failure models have been employed to predict and validate the riverbank failure, and bed deformation with the experimental results under homogeneous conditions. For example, Nagata et al., (2000) and Onda et al., (2010) showed the numerical riverbank failure results in terms of channel processes using the governing equations of flow field in generalized curvilinear coordinate system, non-equilibrium sediment transport model, and intermittent riverbank-collapse model. Arimitsu et al., (2010) investigated the characteristics of the sediment transport and riverbank failure processes in the steep slope curve channel. In addition, Jang & Shimizu (2005) developed a two dimensional numerical model to simulate relatively wide, shallow rivers with an erodible bed and banks. They employed a moving boundary-fitted coordinate system with cubic interpolated pseudoparticle method (CIP) to calculate flow field. Moreover, riverbank failure was simulated when the gradient in the cross-sectional direction of riverbanks was steeper than the submerged angle of repose.

Recently, several researchers simulated the riverbank failure and bed deformation in the natural rivers. For instance, Iwasaki et al., (2012) applied two dimensional depth-averaged model in a general

curvilinear coordinate system with the simple bank failure model to simulate bed deformation of the Otofuke river, Hokkaido, Japan. Moreover, Li et al., (2013) introduced a new norm related to an alluvial riverbank stability assessment. The new model was incorporated into one and two dimensional flow filed and sediment equations in orthogonal boundary-fitted coordinates for simulating river evolution in the Yangtze River, China.

In addition, the exiting experimental flumes were conducted in a straight channel to reveal the effect of bank failure on the temporal change in cross-sectional profile averaged on longitudinal direction under homogeneous and heterogeneous conditions by Nakanishi et al., (2005) and Abe et al., (2006), respectively.

In this regard, the main objectives of this chapter are 1) to develop numerical riverbank failure model under heterogeneous condition because a large number of riverbank failure models are already available on homogeneous condition and 2) to simulate channel processes with riverbank failure and bed deformation in a straight channel under homogeneous and heterogeneous conditions examined by applying a 2D depth averaged model in a general curvilinear coordinate system, an equilibrium sediment transport model and a simple bank failure model. Furthermore, the simple bank failure model is assumed that riverbank erodes when the gradient in the cross-sectional direction of the riverbanks is steeper than the angle of repose.

## 2.2 GOVERNING EQUATIONS

This study applied a plane two-dimensional based morphodynamic model to simulate the riverbank failure and bed deformation. This section describes the main concepts of numerical models and governing equations used into four parts.

### 2.2.1 Flow Equations

A depth-averaged model in a general curvilinear coordinate system was employed to calculate the flow field. The equations were described as follows, Jang & Shimizu (2005).

#### 2.2.1.1 Continuity equation

$$\frac{\partial}{\partial t}\left(\frac{h}{J}\right)+\frac{\partial}{\partial \xi}\left(\frac{hu^{\xi}}{J}\right)+\frac{\partial}{\partial \eta}\left(\frac{hu^{\eta}}{J}\right)=0 \tag{2.1}$$

where $\xi$ and $\eta$ are the spatial coordinate components in general curvilinear coordinate system, $h$ is water depth, $u^{\xi}$ and $u^{\eta}$ are depth averaged flow velocity component in $\xi$ and $\eta$ directions defined as $u^{\xi} = \xi_x u + \xi_y v$ and $u^{\eta} = \eta_x u + \eta_y v$, $u$ *and* $v$ are depth averaged velocity component in $x$ and $y$ directions, $x$ *and* $y$ are the spatial coordinate components in Cartesian coordinate system, and $J$ is the Jacobian of coordinate transformation ($=1/(x_{\xi}\, y_{\eta} - x_{\eta}\, y_{\xi})$).

#### 2.2.1.2 Momentum equations

$$\frac{\partial u^{\xi}}{\partial t}+u^{\xi}\frac{\partial u^{\xi}}{\partial \xi}+u^{\eta}\frac{\partial u^{\xi}}{\partial \eta}+\alpha_1 u^{\xi}u^{\xi}+\alpha_2 u^{\xi}u^{\eta}+\alpha_3 u^{\eta}u^{\eta}=-g\left[\left(\xi_x^2+\xi_y^2\right)\frac{\partial H}{\partial \xi}+\left(\xi_x\eta_x+\xi_y\eta_y\right)\frac{\partial H}{\partial \eta}\right] \\ -\frac{C_f u^{\xi}}{hJ}\sqrt{\left(\eta_y u^{\xi}-\xi_y u^{\eta}\right)^2+\left(-\eta_x u^{\xi}-\xi_x u^{\eta}\right)^2}+D^{\xi} \tag{2.2}$$

$$\frac{\partial u^{\eta}}{\partial t}+u^{\xi}\frac{\partial u^{\eta}}{\partial \xi}+u^{\eta}\frac{\partial u^{\eta}}{\partial \eta}+\alpha_4 u^{\xi}u^{\xi}+\alpha_5 u^{\xi}u^{\eta}+\alpha_6 u^{\eta}u^{\eta}=-g\left[\left(\xi_x\eta_x+\xi_y\eta_y\right)\frac{\partial H}{\partial \xi}+\left(\eta_x^2+\eta_y^2\right)\frac{\partial H}{\partial \eta}\right] \\ -\frac{C_f u^{\eta}}{hJ}\sqrt{\left(\eta_y u^{\xi}-\xi_y u^{\eta}\right)^2+\left(-\eta_x u^{\xi}-\xi_x u^{\eta}\right)^2}+D^{\eta} \tag{2.3}$$

where $t$ is time, $H$ is water surface elevation ($=h+Z_b$), $Z_b$ is bed elevation, $g$ is gravitation acceleration, $C_f$ is the coefficient of riverbed shearing force ($=gn_m^2/h^{1/3}$), $n_m$ is the Manning's roughness coefficient by using the Manning-Stricker equation ($=k_s^{1/6}/7.66g^{1/2}$), $k_s$ is the relative roughness height which is defines as 1-3 $d_{50}$, $d_{50}$ is a mean sediment diameter, and $D^{\xi}$ and $D^{\eta}$ are the diffusion terms in $\xi$ and $\eta$ directions.

The diffusion terms which are expressed the turbulence diffusion were calculated as follows:

$$D^{\xi}=\frac{\partial}{\partial \xi}\left(\nu_t \xi_r^2\frac{\partial u^{\xi}}{\partial \xi}\right)+\frac{\partial}{\partial \eta}\left(\nu_t \eta_r^2\frac{\partial u^{\xi}}{\partial \eta}\right) \tag{2.4}$$

$$D^{\xi}=\frac{\partial}{\partial \xi}\left(\nu_t \xi_r^2\frac{\partial u^{\eta}}{\partial \xi}\right)+\frac{\partial}{\partial \eta}\left(\nu_t \eta_r^2\frac{\partial u^{\eta}}{\partial \eta}\right) \tag{2.5}$$

where $\xi_r$ and $\eta_r$ are the ratios of local grid size in general curvilinear coordinate system to the full-scale length of the grid, $\nu_t$ is the eddy viscosity coefficient, which is estimated by using a zero equation turbulent model ($=\kappa u_* h/6$), $\kappa$ is Von Karman constant (0.4), and $u_*$ is shear velocity.

### 2.2.2 Equilibrium Sediment Transport Equations

#### 2.2.2.1 Homogeneous condition

The two-dimension sediment continuity equation in a general curvilinear coordinate system was described as follows.

$$\frac{\partial}{\partial t}\left(\frac{z_b}{J}\right)+\frac{1}{1-\lambda}\left[\frac{\partial}{\partial \xi}\left(\frac{q_{b\xi}}{J}\right)+\frac{\partial}{\partial \eta}\left(\frac{q_{b\eta}}{J}\right)\right]=0 \tag{2.6}$$

where $\lambda$ is porosity of bed channel material (0.4), $q_{b\xi}$ and $q_{b\eta}$ are the contravariant components of the bedload transport rate per unit width in $\xi$ and $\eta$ directions, respectively.

The sediment transport rate in streamwise direction was calculated using Ashida & Michiue's formula (Ashida & Michiue, 1972), and it is given as :

$$q_{bs} = 17\tau_*^{3/2}\left(1-\frac{\tau_{*c}}{\tau_*}\right)\left(1-\sqrt{\frac{\tau_{*c}}{\tau_*}}\right)\sqrt{Ggd^3} \tag{2.7}$$

where $q_{bs}$ is the sediment-transport rate in streamwise direction, $\tau_*$ is the non-dimensional bed shear stress ($=n_m^2V^2/Gdh^{1/3}$), $V$ is the composite velocity ($=u^2+v^2$), $G$ is the specific weight of sediment in fluid (2.65) and $\tau_{*c}$ is the non-dimensional critical bed shear stress, which is obtained from Iwakagi's formula (Iwakagi, 1956).

The sediment transport rate in transversal direction was calculated using Hasegawa's formula (Hasegawa, 1984), given as:

$$q_{bn} = q_{bs}\left(\frac{u_{nb}}{u_{sb}} - \sqrt{\frac{\tau_{*c}}{\mu_s\mu_k\tau_*}}\frac{\partial z_b}{\partial n}\right) \tag{2.8}$$

where $q_{bn}$ is the sediment transport rate in transversal direction, $u_{sb}$ and $u_{nb}$ are the velocity components in the streamwise and transversal directions near the bed, respectively, and $\mu_s$ and $\mu_k$ are the static and kinetic friction coefficients of bed material, respectively.

When the streamline is curved, secondary flow is generated because of the variation in the centrifugal forces. The near-bed velocity perpendicular to streamwise direction is written as:

$$u_{nb} = u_{sb}N^*\frac{h}{r_s} \tag{2.9}$$

where $r_s$ is the radius of curvature of the streamwise, and $N^*$ is the coefficient of the strength of the secondary flow, which is assumed to be 7.0, as propose by Engelund (1974).

The sediment transport rate in $\xi$ and $\eta$ directions, $q_{b\xi}$ and $q_{b\eta}$, are given as Watanabe et al., (2001).

$$q_{b\xi} = q_{bs}\left[\frac{u_b^\xi}{V_b} - \gamma\left(\frac{\partial z_b}{\partial \xi} + \cos\theta\frac{\partial z_b}{\partial \eta}\right)\right] \tag{2.10}$$

$$q_{b\eta} = q_{bs}\left[\frac{u_b^\eta}{V_b} - \gamma\left(\frac{\partial z_b}{\partial \eta} + \cos\theta\frac{\partial z_b}{\partial \xi}\right)\right] \tag{2.11}$$

where $u_b^\xi$ and $u_b^\eta$ are the flow velocity near the bed in the $\xi$ and $\eta$ directions, respectively, $V_b$ is the resultant velocity near the bed, $\theta$ is the intersection angle between $\xi$ and $\eta$ axes, $\gamma$ is a correction coefficient of sediment transport for slope gradient and $\gamma=(\tau_{*c}/\mu_s\ \mu_k\ \tau_*)^{1/2}$ as proposed by Hasegawa (1984).

#### 2.2.2.2 Heterogeneous condition

The concept of size faction transport is dividing the bed material into size fractions, and considering each size fractions as a uniform material. The bed material transport rate can be calculated by multiplying the potential transport rate corresponded to the given size fraction with the percentage of material, which can be expressed as follows:

$$q_b = \sum_{k=1}^{nk} P_k q_{bk} \tag{2.12}$$

where $q_b$ is the bedload transport rate per unit width, $q_{bk}$ is the potential transport rate for a given size friction $k$, $P_k$ is the concentration of sediment size fraction $k$, and the subscripts $k$ and $nk$ are the number and the total number of size friction, respectively.

The sediment transport rate in streamwise direction under heterogeneous condition can be express by Ashida & Michiue's formula (Ashida & Michiue, 1972) as follows:

$$q_{bk} = 17\tau_{*k}^{3/2}\left(1-\frac{\tau_{*ck}}{\tau_{*k}}\right)\left(1-\sqrt{\frac{\tau_{*ck}}{\tau_{*k}}}\right)\sqrt{Ggd_k^3} \tag{2.13}$$

where $\tau_{*k}$ is the dimensionless shear stress acting on grain of the size in layer $k$ ($=u_*^2/Ggd_k$), $\tau_{*ck}$ is the dimensionless critical shear stress for grain size in layer $k$, and $d_k$ is the representative grain size of layer $k$.

The shielding effect has to be considered for calculating the dimensionless critical shear stress. Therefore, modify version of Asada's formula (Asada, 1972) was employed as follow:

$$\tau_{*ck} = \tau_{*cm}\left[\frac{\log_{10} 23}{\log_{10}\left(21\frac{d_k}{d_{50}}+2\right)}\right]^2 \tag{2.14}$$

where $\tau_{*cm}$ is the dimensionless critical shear stress of median diameter $d_{50}$.

Then, the bed deformation was computed by using the sediment continuity equation as follow:

$$\frac{\partial}{\partial t}\left(\frac{z_b}{J}\right)+\frac{1}{1-\lambda}\left[\frac{\partial}{\partial \xi}\left(\frac{\sum q_{bk}^{\xi}}{J}\right)+\frac{\partial}{\partial \eta}\left(\frac{\sum q_{bk}^{\eta}}{J}\right)\right]=0 \tag{2.15}$$

where $q_{bk}^{\xi}$ and $q_{bk}^{\eta}$ are the bedload transport in $\xi$ and $\eta$ directions of layer $k$. Eqs. (2.10) and (2.11) is applied to calculate $q_{bk}^{\xi}$ and $q_{bk}^{\eta}$ for each grain size layer in the $\xi$ and $\eta$ directions.

### 2.2.3 Simple Bank Failure Model

A simple bank failure model is employed for this study, consistent with several researchers e.g. Arimitsu et al., (2010), Iwasaki et al., (2010), Jang & Shimizu (2005), Nagata et al., (2000), and Onda et al., (2010).

Bank failure occurs when bed slope among four neighbor cells becomes steeper than the angle of repose of the bed material after bed scouring. **Fig. 2.1** illustrates a simple bank failure model in which bank slope adjustment is set to be milder than the angle of repose and the volume of bank failure is set equal to the volume of deposition.

A simple bank failure equations can be expressed as follows:

$$\Delta\zeta_0 = \frac{L(\tan\theta - \tan\varphi)}{1 + \frac{A_0}{A_1}} \tag{2.16}$$

$$\Delta\zeta_1 = \frac{L(\tan\theta - \tan\varphi)}{1 + \frac{A_1}{A_0}} \tag{2.17}$$

where $L$ is gird cell width, $\zeta_0$ and $\zeta_1$ are bank and bed elevations, $\Delta\zeta_0$ and $\Delta\zeta_1$ are bank and bed elevation changes, and $A_0$ and $A_1$ are the width of bank and bed grid surface area, respectively.

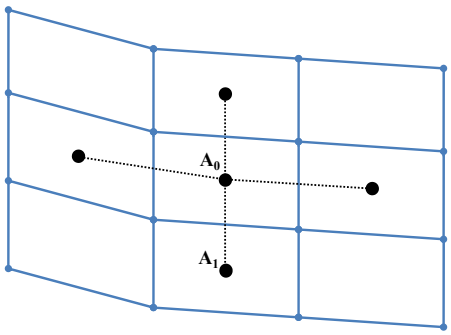


(a) Top view of a simple bank failure model.

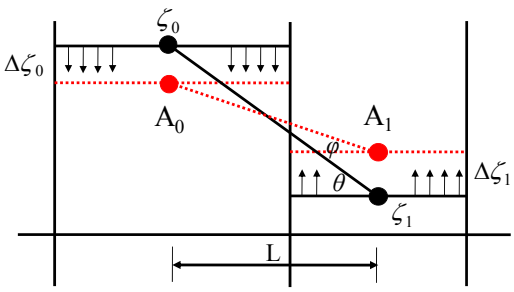


(b) Side view of a simple bank failure model.

**Fig. 2.1** A simplified bank failure process.

### 2.2.4 Computational Procedures

The computational model applies the following processes to simulate channel processes with bed deformation and bank failure in a straight channel under homogeneous and heterogeneous conditions with time at infinitesimal interval up to the designated time for the given initial conditions:

(1) Compute the 2D depth-average flow in a general curvilinear system of experimental channel. The governing equations (i.e., the continuity and momentum equations for flow field) are numerically calculated using finite difference method with computational grid in general coordinate systems $(\xi,\eta)$.

In order to solve the governing equations, the Cubic Interpolated Pseudoparticle Method (CIP) is used.

(2) Compute the secondary flow perpendicular to the streamwise direction of a 2D depth-average flow model.

(3) Compute sediment transportation rate and river bed deformation.

(4) Determine how bank failure and sediment deposition alter the shape of channel.

(5) Set a coordinate system using the new boundary and update the computational data set.

(6) Update the computational time.

## 2.3 RESULTS AND DISCUSSION

This section separates the results and discussion into four parts, namely: (1) the existing experiment flume conditions, (2) the optimization results for the angle of repose, (3) the results of transversal grid sensitivity analysis and the simulation time, and (4) the computational results of bank failure.

### 2.3.1 The Existing Experiment Flume Conditions

This study employed the existing experiment flume data which revealed the effects of bank failure on the temporal change in cross-sectional profile and averaged in longitudinal direction, for homogeneous condition by Nakanishi et al., (2005) and heterogeneous condition by Abe et al., (2006) for computational model setup and calibration. The flume experiments were conducted in a straight trapezoidal channel with 11 m. in length and 0.45 m. in width. The bank failure occurred only on the left bank, illustrated as the experiment flume characteristics in **Fig. 2.2**. The grain size distribution diagram of heterogeneous condition is illustrated in **Fig. 2.3**. Moreover, the exiting experiment flume conditions are summarized of both grain sizes in **Table 2.1**. The gradation coefficient ($\sigma_g$) of heterogeneous condition ($=[d_{84}/ d_{16}]^{1/2}$) with $d_{16}$= 0.029 mm and $d_{84}$ = 3.627 mm shows a high gradation coefficient value (11.18), which is described as a well-graded mixture in the existing heterogeneous grain size condition.

### 2.3.2 The Optimization Results for the Angle of Repose

This process is very important to adjust the angle of repose of bank materials, which is generally reported to be 30$^o$ to 32$^o$ for sand (0.25 mm $\leq d_{50} <$ 1 mm) (Julien, 2002) because the angle of repose with bank failure mainly depends on the characteristics of bank materials. Therefore, the appropriate angle of repose can be found from the computational model by varying the angle of repose in the range of 20$^o$ to 45$^o$ in the homogeneous condition and from of 30$^o$ to 50$^o$ in the heterogeneous condition. As a result, the optimized angles of repose, from the computational model, were found to be 35$^o$ in both grain size conditions, which are larger than the standard value 30$^o$ to 32$^o$, providing a suitable computational results compared with the existing experiment flume data. In addition, the results for the angle of repose by trial and error showed good agreement with the empirical formula by Zhang et al., (1989).

$$\varphi = 32.5 + 1.27 d_{50} \tag{2.18}$$

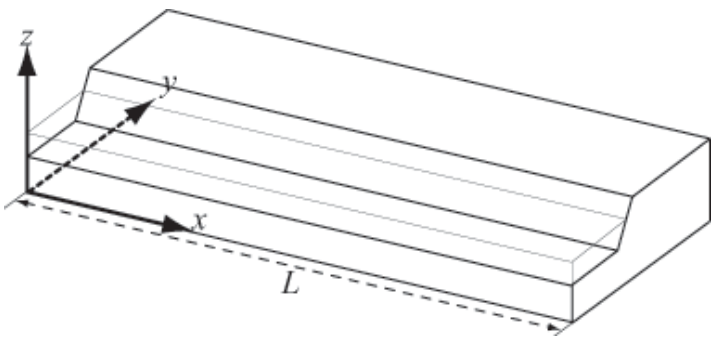


(a) The experiment flume in plain view.

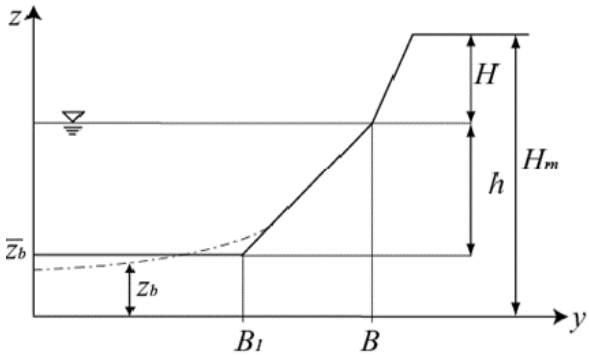


(b) The initial cross-sectional profile.

**Fig. 2.2** A simplified bank failure model (Nakanishi et al., 2005).

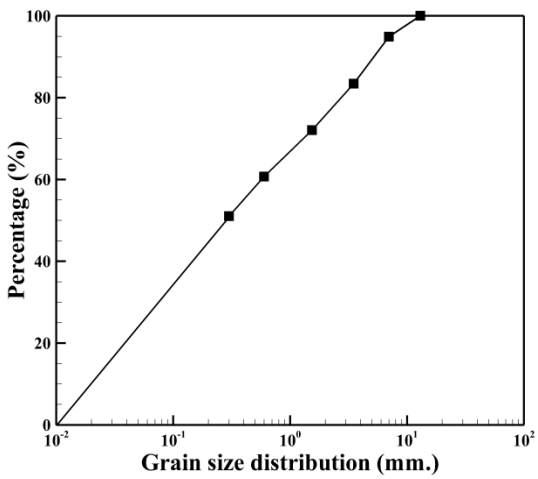


**Fig. 2.3** The grain size distribution of heterogeneous condition.

Table 2.1 The existing experiment flume conditions.

| Case | Flow (l/s) | Bank height (cm.) | Bed slope | Mean diameter (mm.) | Simulation time (hrs.) |
|---|---|---|---|---|---|
| (1) Homogeneous condition: | | | | | |
| 1. | 6 | 10.5 | 1/200 | 0.5 | 1 |
| 2. | 6 | 10.5 | 1/500 | 0.5 | 1 |
| 3. | 6 | 12.5 | 1/200 | 0.5 | 1 |
| (2) Heterogeneous condition: | | | | | |
| 4. | 6.7 | 8.5 | 1/100 | 1.56 | 2 |
| 5. | 2.6 | 7.5 | 1/100 | 1.56 | 4 |
| 6. | 2.6 | 8.5 | 1/100 | 1.56 | 2 |

where $\phi$ is the angle of repose. This empirical formula yields angle of repose that are equal to 33.1$^{o}$ and 34.5$^{o}$ for the homogeneous and heterogeneous conditions, respectively.

Moreover, it is found that the banks with a larger angle of repose show less erosion rate than those with smaller angle of repose for the both grain size conditions. The computational results for the optimization of angle of repose in homogeneous condition (Case 2) and heterogeneous condition (Case 5) at 15 and 30 minutes of simulations are shown in **Fig. 2.4**.

### 2.3.3 The Results of Transversal Grid Sensitivity Analysis and Simulation Time

The transversal grid sensitivity analysis was used to find the appropriate transversal grid size by various transversal grid size among 5 cm, 2.5 cm, 1.25 cm, 1.0 cm, 0.5 cm, 0.25 cm, 0.125 cm and 0.1 cm with a fixed grid interval in the streamwise direction ($\Delta x$=1 m), and a simulation time step ($\Delta t$=0.0005 s) in homogeneous conditions.

The transversal grid sensitivity analysis indicated that when the transversal grid size was finer than 1 cm, the accuracy of the numerical model was not dramatically different than that with a transversal grid size of 1 cm. Therefore, the suitable transversal grid size for this study was set to 1 cm. The results of the transversal grid sensitivity analysis are shown in **Fig. 2.5**. In addition, the required simulation time for the difference transversal grid size are shown in **Fig. 2.6**.

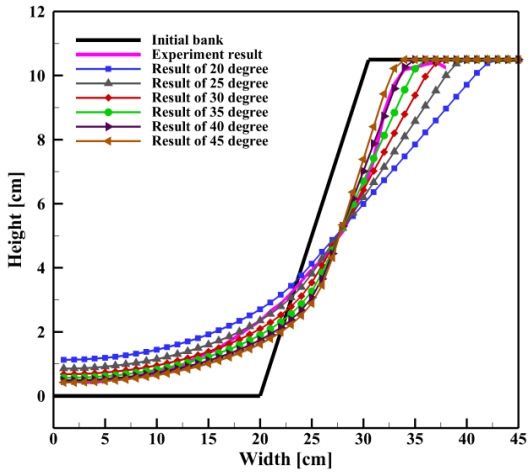


(a) The comparison results of Case 2 at 15 minutes in each angle of repose.

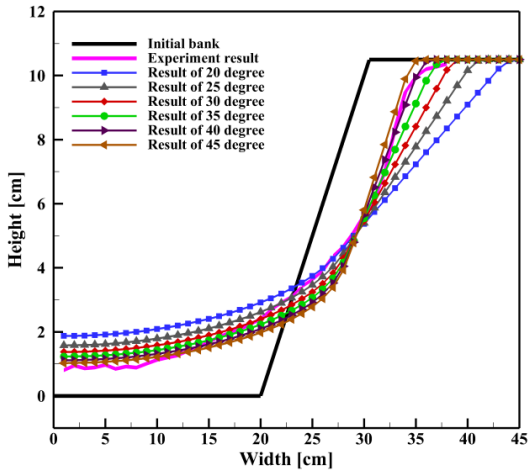


(b) The comparison results of Case 2 at 30 minutes in each angle of repose.

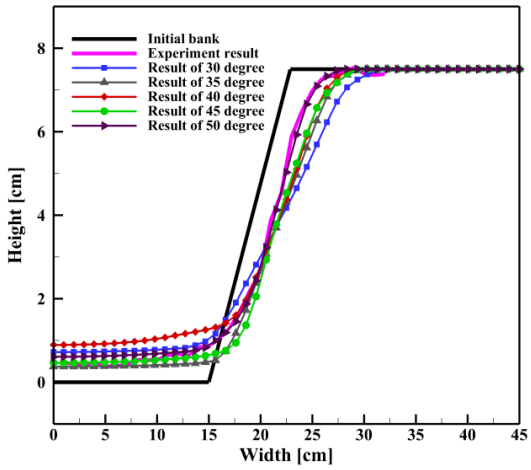


(c) The comparison results of Case 5 at 15 minutes in each angle of repose.

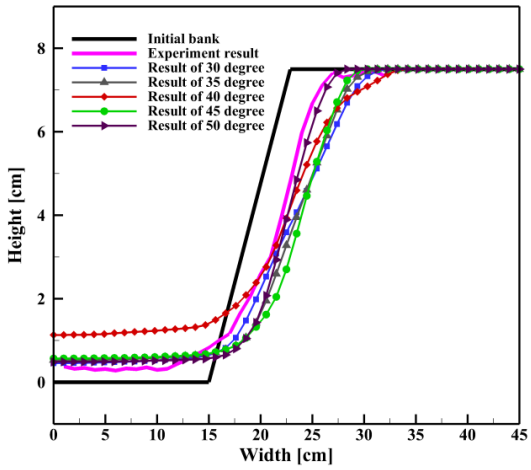


(d) The comparison results of Case 5 at 30 minutes in each angle of repose.

**Fig. 2.4** The optimization results of angle of repose in homogeneous (Case 2) and heterogeneous (Case 5) conditions.

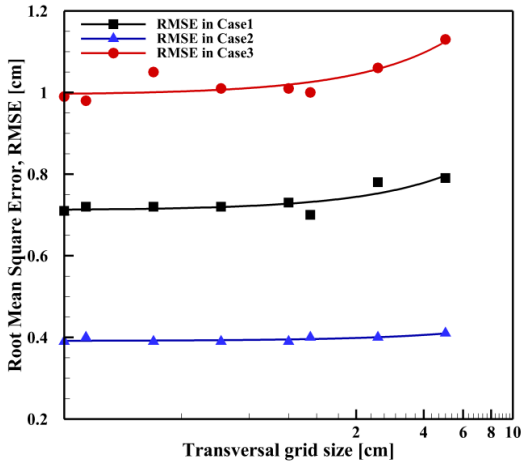


**Fig. 2.5** The results of transversal grid sensitivity analysis.

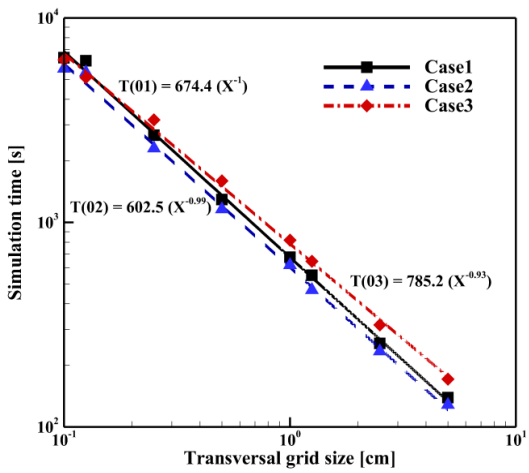


**Fig. 2.6** The results of computational time in difference transversal grid size.

### 2.3.4 The Computational Results of Riverbank Failure

Numerical simulations were setup and computed under the existing experiment flume conditions. The computational angle of repose ($\phi$) and simulation time step ($\Delta t$) were 35$^{o}$ and 0.0005 s, respectively.

This study set 12 grid points in the streamwise direction and 47 grid points in transversal direction which led to grid sizes of 1 m and 1 cm, respectively. A periodic boundary condition was set in streamwise direction for the bed deformation, channel adjustment, and bank failure. Moreover, the bottom friction parameter was estimated by the Manning-Strickler equation, which were equal to 0.014 in the homogeneous condition and 0.016 in the heterogeneous condition. In addition, the void rations (porosity) of channel material were 0.4 and 0.6 for the homogeneous and the heterogeneous condition, respectively.

#### 2.3.4.1 The results of homogeneous condition

Using the computational model, this study replicated the existing experiments conducted by Nakanishi et al., (2005), as shown details in Table 2.1 for the homogeneous condition from Case 1 to Case 3. The difference between Case 1 and Case 2 is the initial bed slope, and Case 2 and Case 3 include different riverbank heights. These cases were conducted to investigate the influence of the actual shear stress and riverbank height on the rate of bank failure, respectively.

The results of homogeneous condition show the temporal change in cross-sectional profile averaged over longitudinal direction as shown in **Fig. 2.7**. The numerical results are in a relatively good agreement with the experimental data. However, **Fig. 2.7** shows that the numerical results exceed the experimental data and this error tends to increase with time. In addition, it was found that the simulation results of Case 1 and Case 3 (steep slope condition, 1/200) after 60 minutes period of computational time show an overprediction in the bank failure when the bank failure reaches channel boundary condition.

The compared computation results of Case 1 and Case 2 with difference initial bed slope were shown that the steeper initial slope (Case 1) performs larger shear stress than initial mild bed slope (Case 2). In addition, the comparison results between Case 1 and Case 3 with different bank height were shown in **Fig. 2.7**. It can be seen that the erosion rate in Case 1 has greater rate than that other homogeneous cases.

Moreover, it can be seen that there is a point dividing the region into deposition and failure zones, which is relatively common behavior for channels with homogeneous condition. On the other hand, dunes in Case 1, observed in the exiting homogenous experimental results, were not reproduced in computational results. It is due to the fact that the limitation of 2D depth averaged flow model is applied to calculate the flow fields. However, alternate bars in Case 2 were not well simulated in computational results.

#### 2.3.4.2 The results of heterogeneous condition

The heterogeneous condition modeling replicated the existing experiments conducted by Abe et al., (2006) as described in Table 1 from Case 4 to Case 6.

**Fig. 2.8** shows the temporal change in cross-sectional profile averaged over longitudinal direction for the case of heterogeneous condition. The comparison results between the computational results and experimental data show a good agreement for the bank erosion rate. In contrast, the bed deformation results illustrate an unsatisfactory agreement.

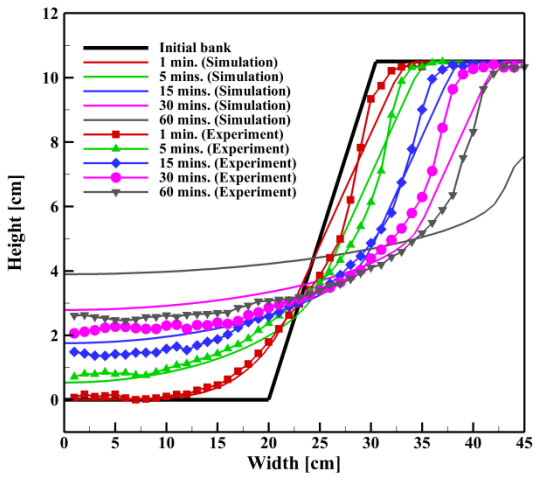


(a) The comparison results in Case 1.

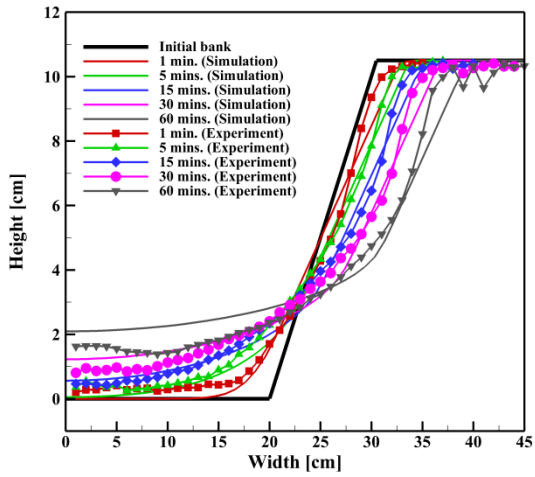


(b) The comparison results in Case 2.

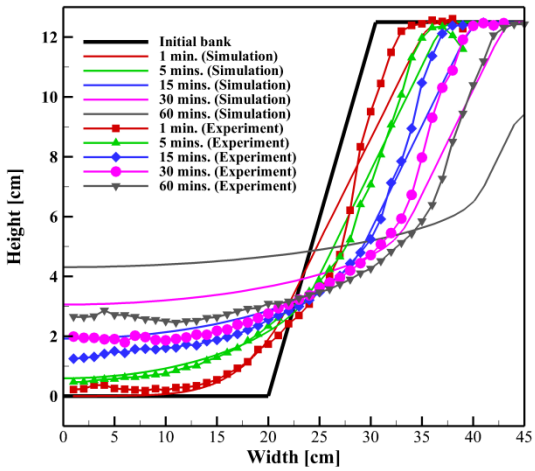


(c) The comparison results in Case 3.

**Fig. 2.7** The comparison results between numerical computation and experimental data in homogeneous condition.

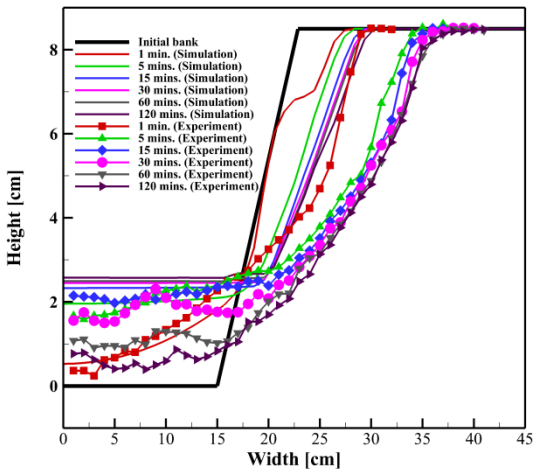


(a) The comparison results in Case 4.

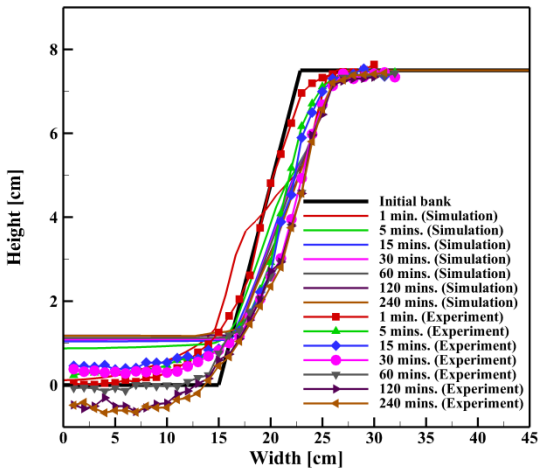


(b) The comparison results in Case 5.

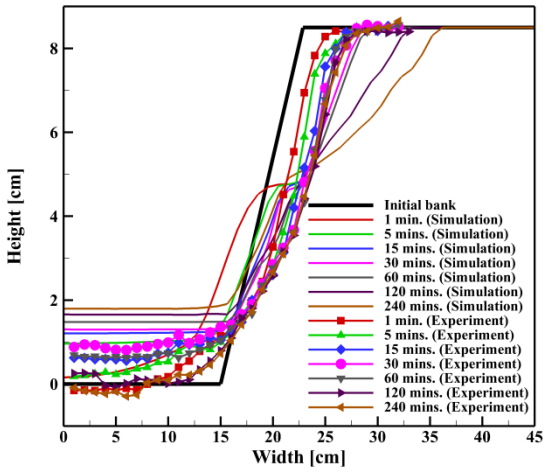


(c) The comparison results in Case 6.

**Fig. 2.8** The comparison results between numerical computation and experimental data in heterogeneous condition.

The difference in the bed deformation between computational results and experimental results causes an exceeding in the dimensionless shear stress over the critical shear stress (based on Shield's diagram as it is mentioned by Iwakagi's formula) over the whole range of bed channel and the distribution of the dimensionless shear stress around riverbank is complicated for computation in case of simple bank failure. **Fig. 2.9** shows the dimensionless shear stress profile for heterogeneous condition as a representative result after 60 minutes of the physical time.

In addition, the influence of the amount of sediment deposited on an armor layer of the sediment transport is presented in our computational results. Therefore, armoring effect of bed layer, which is the result of erosion of fine particles on the bed (leaves the coarse fractions of the mixture on the bed) induced coarsening of the bed material and it is fully developed to protect bank erosion after 60 minutes of physical time. Consequently, the development of armor layer, a well mixed sediment materials ($0.3\ mm < d < 13\ mm,\ d_{50}=1.54\ mm$), was placed on the top of bank toe with an average grain size of 3-5 mm. as shown in **Fig. 2.10**.

## 2.4 SUMMARY

A computational model for bed deformation and bank failure under homogenous and heterogeneous conditions were employed to predict channel morphology processes by using a two-dimension boundary-fitted curvilinear coordinate system, an equilibrium sediment transport, and a simple bank failure model. It was found that both grain size conditions can reproduce the experimental results by using an appropriate values of the angle of repose and computational grid sizes. It should be noted that a good agreement can be observed in homogeneous condition in the case of mild slope channel (Case 2, 1/500). On the other hand, dunes in Case 1, observed in the exiting homogenous experimental results, cannot reproduced in computational results. It is due to the fact that the limitation of 2D depth averaged flow model is applied to calculate the flow fields. However, alternate bars in Case 2 are not well simulated in computational results. In the heterogeneous condition, the results of bank erosion rate showed a satisfactory agreement with the experimental results but an unsatisfactory agreement for the bed deformation. The difference in bed deformation caused the dimensionless shear stress exceeded the critical values over the whole range of bed channel and the distribution of the dimensionless shear stress around riverbank was complicated for computing bed deformation in case of simple bank failure. Finally, the armoring effect was developed to protect bank erosion on the bank-toe with an average grain size of 3-5 mm after 60 minutes of simulation time.

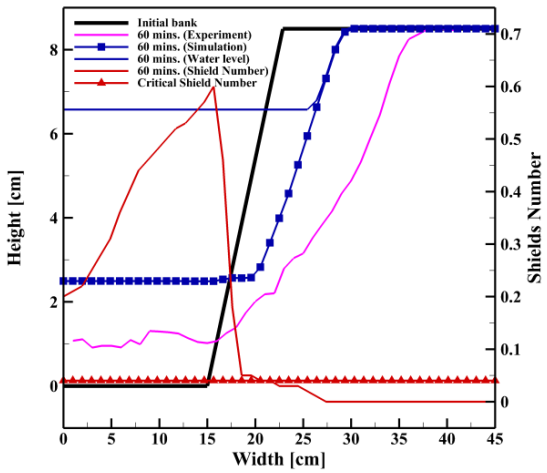


(a) The dimensionless shear stress in Case 4.

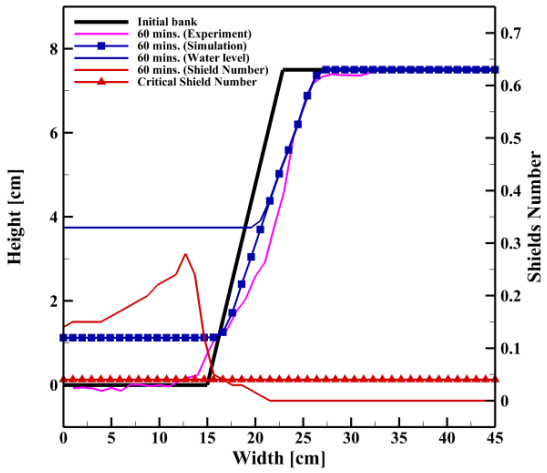


(b) The dimensionless shear stress in Case 5.

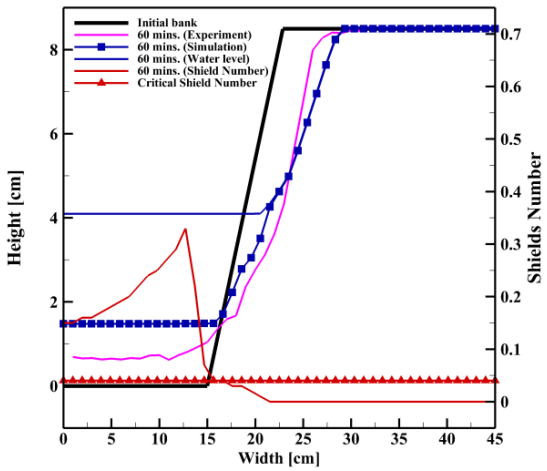


(c) The dimensionless shear stress in Case 6.

**Fig. 2.9** The dimensionless shear stress profile of heterogeneous condition.

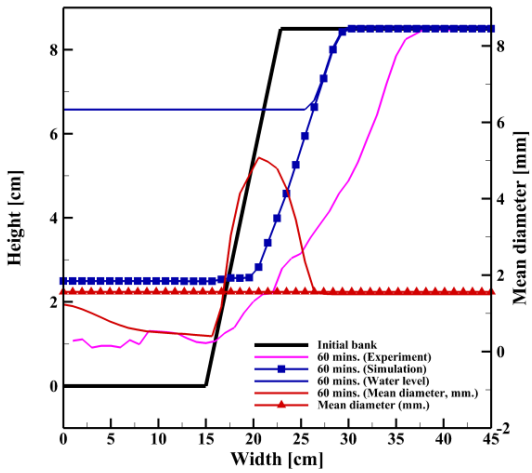


(a) The armoring effect of bed layer in Case 4.

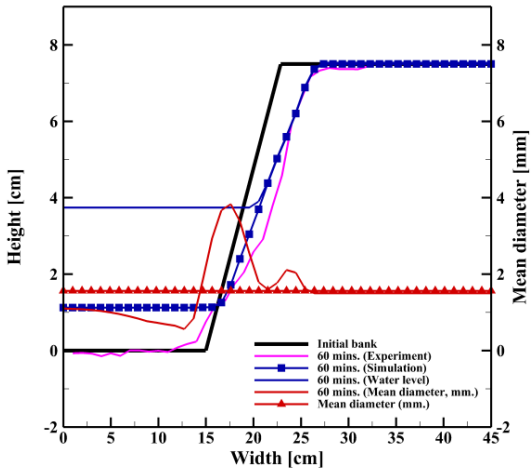


(b) The armoring effect of bed layer in Case 5.

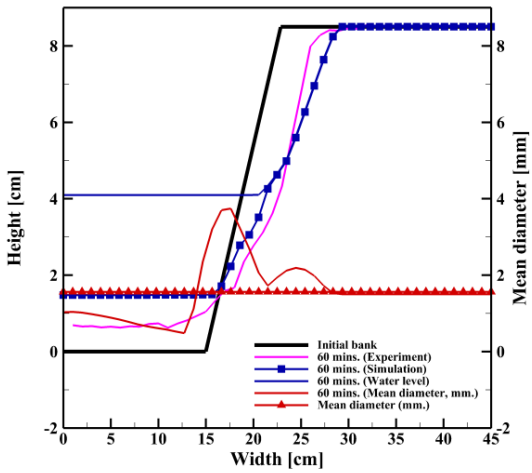


(c) The armoring effect of bed layer in Case 6.

**Fig. 2.10** The mean diameter profile of armoring effect in heterogeneous condition.

# Chapter 3

# CANTILEVER FAILURE INVESTIGATIONS FOR COHESIVE RIVERBANKS

## 3.1 INTRODUCTION

Riverbank failure results in extensive sediment production in an alluvial channel, and it can cause severe environmental and economic problems such as loss of fertilization in agricultural areas and destruction of infrastructure (Taghavi et al., 2010). However, because a cantilever failure involves a rapid channel widening and delivers a large volume of sediment into the channel, such a failure is a serious issue in river engineering (Dapporto et al., 2003; Nardi et al., 2012; Taghavi et al., 2010). Elucidating the underlying mechanism of cantilever failure is therefore important for a complete understanding of fluvial erosion and riverbank failure along a channel.

In previous studies, researchers have been unable to analyze cantilever failure and have focused mainly on simple bank failures such as rotational slip failure, toppling failure, and mass wasting failure (ASCE, 1998; Duan, 2005; Osman & Thorne, 1988). Moreover, estimations of the failure plane angle and tension crack depth have been analyzed using a combination of field and experimental data (Taghavi et al., 2010). Only a few studies have applied stability analyses based on the safety factor of the portion with cantilever failure, from which three types of possible cantilever failure mechanisms have been defined: shear-type, beam-type, and tensile-type failures (Abam, 1997; Thorne & Tovey, 1981).

Several previous studies have reported small-scale cantilever failure experiments, including experimental studies examining fluvial erosion and cantilever riverbank mechanisms (Fukuoka et al., 1999), and experimental studies measuring flow characteristics near and inside eroded riverbanks (Bahar & Fukuoka, 2002). A couple of large-scale experimental studies on the failure mechanism of cantilevers have been reported recently. Taghavi et al., (2010) conducted experiments to estimate the failure plane angle and tension crack depth, and Samadi et al., (2013) carried out experimental studies to investigate dominant cantilever failure mechanisms; finding that beam-type and tensile-type failures are dominant. Moreover, Nardi et al., (2012) conducted experiments to investigate mass failures in a sandy gravel riverbank and showed the occurrence of a variety of failure processes such as cantilever, slab, and slide failures. However, all of the large-scale experiments focused solely on processes related to cantilever failure and the interaction between stagnant water and cohesive materials; fluvial erosion was not taken into account.

Previous numerical works have studied simple bank failure mechanisms by using simple bank failure models (ASCE, 1998; Iwasaki et al., 2012; Jang & Shimizu, 2005; Nagata et al., 2000). In addition, a coupled model of fluvial erosion and mass wasting was developed to reproduce fluvial erosion processes in a bank-toe, degradation in a channel bed and destabilization of an upper bank (Darby et al., 2007; Duan & Julien, 2010).

Several numerical studies have been developed towards an understanding of the complex mechanisms of a cantilever failure. For example, Bahar & Fukuoka (2002) employed a semi-implicit method, applying a pressure-linked equation algorithm to reproduce flow characteristics near and inside eroded riverbanks. In addition, shear-type and beam-type failure mechanisms were studied to identify the significant effects of uncertainty parameters on the reliability of a riverbank stability model in determining a cantilever failure. The results showed that the overhanging block dimensions and the cohesive force are highly significant for an analysis of cantilever stability (Samadi et al., 2011). A stress-strain behavior model for a cantilever failure was also applied to simulate the subsequent failure of an overhanging block (Samadi et al., 2013). However, those previous studies have limitations in coupling fluvial erosion with cantilever failure and simulations coupling fluvial erosion and cantilever failure therefore need to be conducted.

To address the gap between experiments and numerical modeling of the process of a cantilever failure, experimental studies were conducted on a rectangular flume in this work. Furthermore, a novel coupled numerical model was developed by considering the effects of fluvial erosion and intermittent cantilever failure for cohesive riverbanks.

## 3.2 METHODOLOGY

This section provides an overview of the experimental setup and a description of the numerical model.

### 3.2.1 Experimental Setup

To address many of the ambiguities in the underlying mechanisms of a cantilever failure and because of a lack of reported experimental studies, laboratory experiments related to fluvial erosion and cantilever failure were conducted using a fixed bed in a straight rectangular channel with Plexiglas walls to allow for real-time observations and recording. The water and sediments were recirculated using a constant head tank of water placed at the upstream end of a flume, but here both sides of a flume have a constant-head tank. Moreover, to reproduce a steady uniform flow for each case examined, the water discharge remained constant at 2.4 to 6.4 l/s using a notch weir to regulate a constant discharge during the experiments. The initial water level was set to zero and a free-flowing condition was controlled at the downstream end. The flume was 30 cm wide, 10 m long and 20 cm high, and the channel slope was set to 1/500, as shown in **Fig. 3.1**. In the upstream region of the flume (2 to 3.8 m from the upstream), a wooden board was installed to avoid fluvial erosion (I to II). At the middle reach of the flume (3.8 to 5.2 m from the upstream), a cohesive riverbank was set (II to III). The cohesive riverbank was 16 cm wide, 1.4 m long and 15 to 20 cm high, with the height varying in each case considered. Downstream of the cohesive riverbank, a second wooden board was installed to protect the cohesive riverbank from fluvial erosion (III to IV).

During the experiments, sediment composed of sand and silt with mean diameters ($d_{50}$) of around 0.23 mm and 28.4 μm, respectively, was used. The sediment mixture was initially wetted with water to achieve a water content of 17.5 to 48.0% for silt-clay content (SC) of 10%, 20% and 30%. For this study, two parameters (i.e. the percentage of silt-clay content and water content) were varied in each case, because the cohesive force of cohesive riverbanks is related mainly to the percentage of silt-clay content (Couper, 2003; Dulal & Shimizu, 2010; Julian & Torres, 2006) and water content (Couper, 2003; Rinaldi & Nardi, 2013; Thorne & Tovey, 1981). However, the sediment mixtures were prepared by mainly varying the percentage of silt-clay content because, for the sediments used in this study, it was difficult to control the water content with the different percentages of silt-clay content.

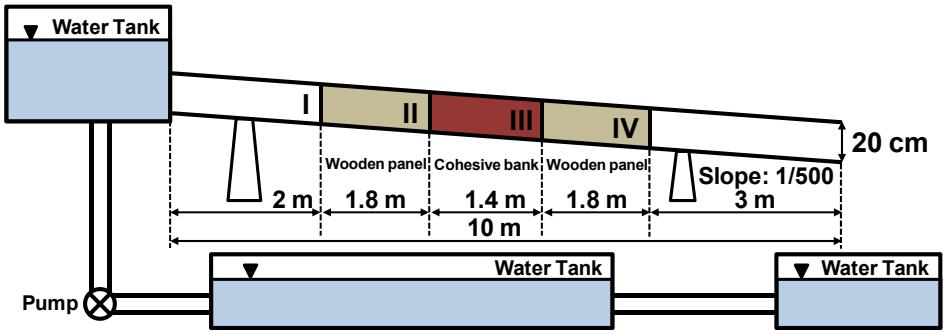


(a) Overview of experimental setup.

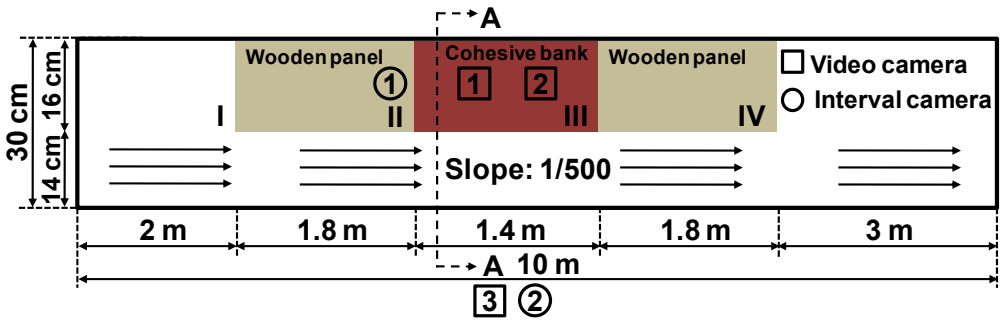


(b) Top view of experimental flume.

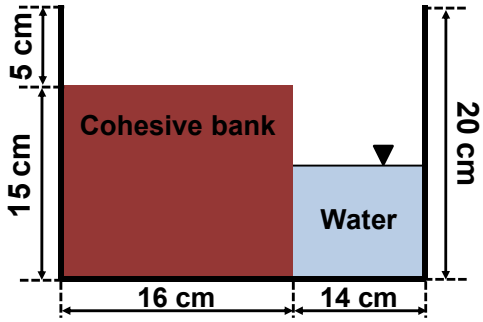


(c) Cross-section of experimental flume (A-A section).

**Fig. 3.1** The dimensions of experimental flume.

Before carrying out the experiments, the cohesive materials were tested to determine the cohesive force and internal friction angle by using a direct shear device based on the ASTM D3080-98 standard test method for direct shear testing of soil under consolidated drained conditions (ASTM, 1998). Similarly to the previous work (Sutarto et al., 2014), the direct shear test used in this study was consolidated by gradually increasing the normal stress by means of ASTM D2435-96 (ASTM, 1996). The soil samples were carefully trimmed to fit within the shear box dimensions and then placed in the shear box. Moreover, the cohesive materials were consolidated through normal stress under loads of 5, 10 and 20 kPa for 24 h. The horizontal and vertical deformations and corresponding applied shear stresses were then recorded simultaneously. The process was conducted for each sample by using the three normal stress loads. The slope of the best-fit line from the data provided the internal friction angle and the *y*-intercept provided the cohesive force (**Fig. 3.2**). Additionally, a direct shear test of pure sand was conducted to determine the cohesive force (3.09 kPa.) and internal friction angle (41.28°). However, in this study, a direct shear test was carried out for only one sample per each normal stress and therefore the results obtained gave a slightly different cohesive force and internal

friction angle compared with the replicated sample process (at least three replicates) at each normal stress.

To allow for a sufficient consolidation process, the cohesive banks were compacted by applying a static load of 0.04 kg/cm$^2$ for 72 h (Nardi et al., 2012). Dynamic compaction was not used either to protect the Plexiglas walls from damage or to reproduce the natural cohesive riverbank conditions that normally occur through static compaction. During the cohesive riverbank construction, a wooden panel was positioned to form a vertical bank. The panel was removed before the experiments started. The experimental conditions required to stop the test were (1) when cantilever failures proceeded throughout all of the cohesive riverbanks or (2) when an equilibrium stage was reached (without a failure for a 2-h period). Composite layers were not considered in this study because of uncertainties regarding the cantilever failure phenomenon and lack of previous studies. Each layer had its own geotechnical properties and the overhanging failure block is divided into a number of vertical slices. The bank geometries, discharges and cohesive properties used during the experiments are summarized in Table 3.1.

Table 3.1 Summary of experimental conditions.

| Case | Discharge (l/s) | Bank height (cm) | Silt-clay content (%) | Water content (%) | Internal friction angle (°) | Cohesive force (kPa) | Re | Fr |
|---|---|---|---|---|---|---|---|---|
| 1 | 4.0 | 20 | 10 | 17.5 | N/A | N/A | 25,000 | 0.78 |
| 2 | 4.0 | 20 | 30 | 39.6 | 34.3 | 5.76 | 25,000 | 0.78 |
| 3 | 4.0 | 15 | 30 | 39.6 | 34.3 | 5.76 | 25,000 | 0.78 |
| 4 | 2.4 | 15 | 30 | 39.6 | 34.3 | 5.76 | 15,000 | 0.74 |
| 5 | 4.0 | 15 | 20 | 32.2 | 41.3 | 6.41 | 25,000 | 0.78 |
| 6 | 5.8 | 15 | 20 | 32.2 | 41.3 | 6.41 | 36,250 | 0.81 |
| 7 | 6.4 | 15 | 30 | 48.0 | 39.8 | 5.37 | 40,000 | 0.82 |

The advantage of our experiment was the possibility to observe and record the cantilever failure mechanisms from the top and side views of the experimental flume during the fluvial erosion, tension crack and cantilever failure. All failure mechanisms were recorded by using three high-resolution video cameras and two interval recorder devices, as shown in **Fig. 3.1(b)**. The video cameras were kept at a fixed perpendicular position for the top and side views of the channel to record the temporal bank width and water depth. Additionally, the metric scales were positioned in both the horizontal and vertical directions of the channel. The video frames were subsequently converted into gray-scale metrics and the temporal bank width and water depth were determined through a digitization process with a precision of around 1 mm.

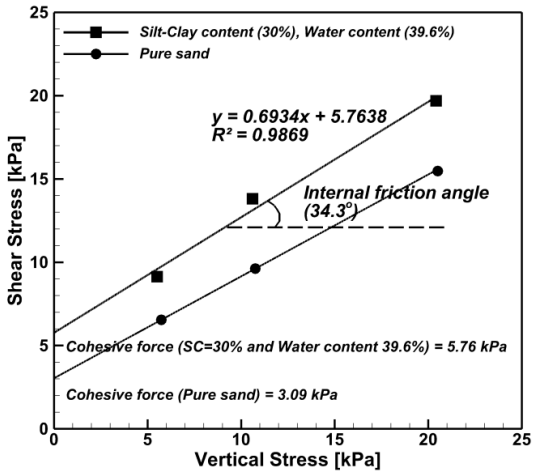


(a) SC (30%) and water content (39.6%).

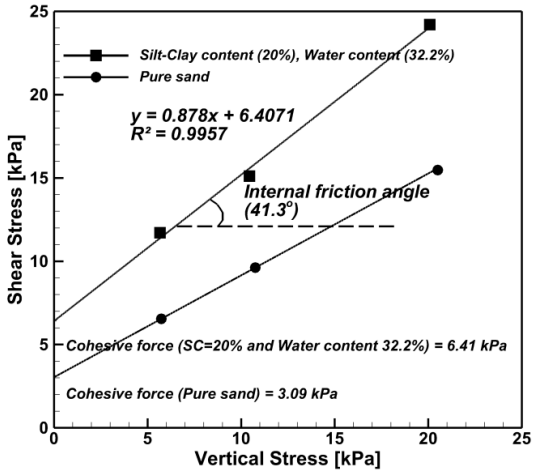


(b) SC (20%) and water content (32.2%).

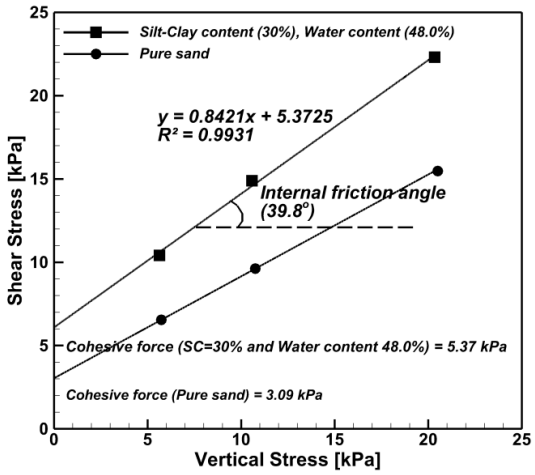


(c) SC (30%) and water content (48.0%).

**Fig. 3.2** Direct shear test results of cohesive materials.

### 3.2.2 Numerical Model

The main objective of the numerical model was to reproduce the physical mechanisms of fluvial erosion, tension crack and cantilever failure of the cohesive riverbanks.

A cantilever failure model was developed by implementing a triple-grid approach, consisting of a coarse one dimensional (1D) grid for the flow field in the lateral direction, a fine 1D grid for sediment transport and bed deformation in the lateral direction and a 2D grid for a cantilever failure in the vertical and lateral directions (**Fig. 3.3**). During the initial stage of the computation (**Fig. 3.4**), the model reproduced fluvial erosion at the lower part of the riverbank, which is shown by the dashed line in zone 1. Next, the tension crack in zone 2 and the cantilever failure in zone 3 (the dashed vertical line along the cohesive riverbank) were captured using the computational model. This approach involves applying the three submodels—fluvial erosion, cantilever failure and bedload sedimentation—at each of a series of discrete time steps. A logic diagram of the computational sequence used for the coupled mechanism of fluvial erosion and cantilever failure is illustrated in **Fig. 3.5**.

#### 3.2.2.1 Fluvial erosion

The flow field was calculated using a uniform flow model (Sturm, 2001) on a coarse lateral 1D grid cell, considering the sidewall correction effect in the narrow laboratory channel (Process 1 in **Fig. 3.5**), written as

$$u_j = \frac{1}{n} R_j^{2/3} i^{1/2} \tag{3.1}$$

where $u_j$ is the velocity in each calculated cell, n is the Manning roughness parameter along the channel (0.011), calculated using the Manning–Strickler equation ($k_s^{1/6}/7.66g^{1/2}$) in which $g$ is the gravity acceleration (9.81 m/s$^2$) and $k_s$ is the relative roughness height, defined as 1-3$d_{50}$ (1.5$d_{50}$), $R_j$ is the hydraulic radius in each calculated cell ($A_j/P_j$), $A_j$ being the cross-sectional area in each calculated cell and $P_j$ being the perimeter length in each calculated cell, i is the bed slope and j is the lateral calculated cell number. For this study, the Manning roughness parameter was in the range of the hydraulically smooth channel ($0.01 < n < 0.02$) (Julien, 2002). In addition, the mean diameter ($d_{50}$) of the sediment mixture was smaller than the pure sand sediment. As a result, the Manning roughness parameter of the sediment mixture was smaller than that of the pure sand sediment, this value still being in the range of the hydraulically smooth channel. Therefore, the influence of silt-clay content was neglected for estimating the Manning roughness parameter in this study.

For fluvial erosion, calculation of the bank erosion rate was required to determine the hydraulic parameters and riverbank geometries (Process 2 in **Fig. 3.5**). The set of equations for fluvial erosion consists of three main equations — namely, one for the erosion coefficient ($E$), one for the depth-averaged bank erosion rate from fluvial erosion ($\bar{\xi}$) and one for the bank erosion rate ($M_e$) (Duan, 2005).

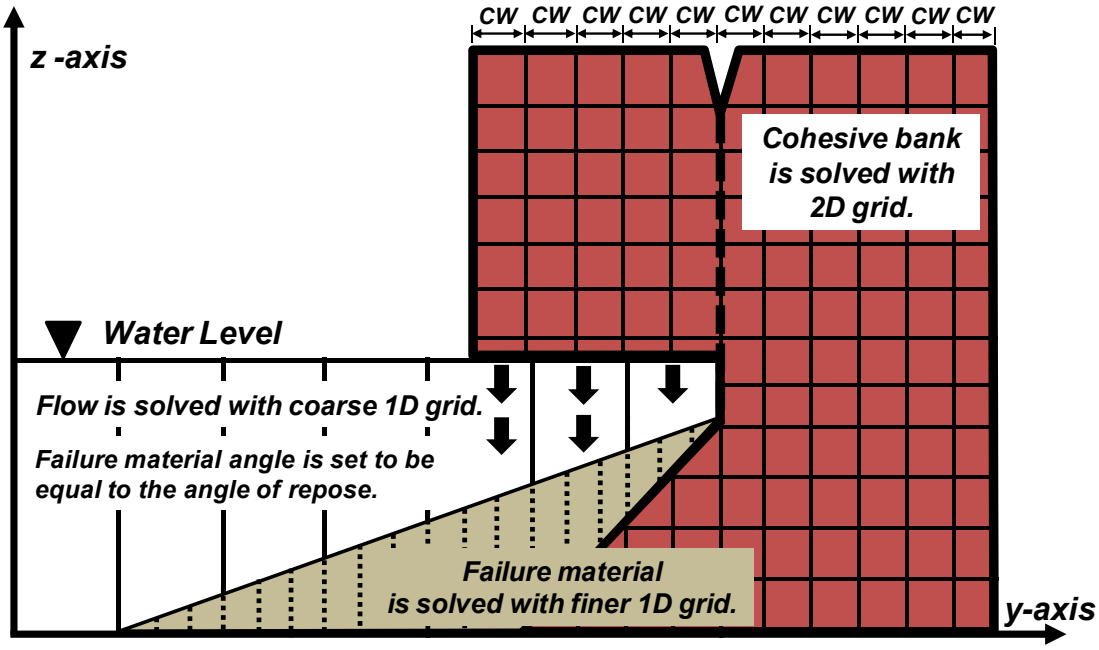


**Fig. 3.3** Framework of triple-grid approach of cantilever failure model.

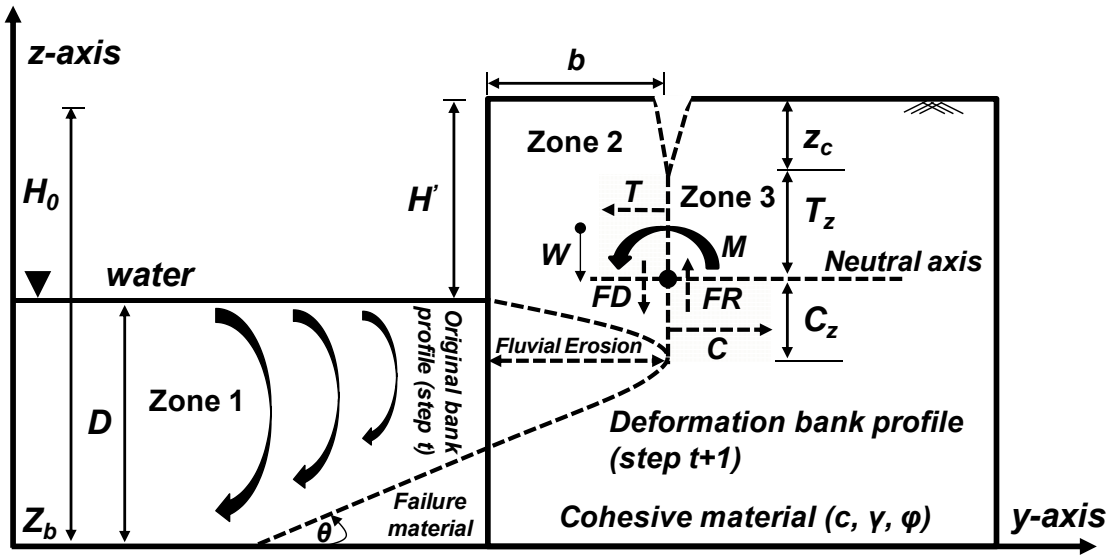


**Fig. 3.4** Overhanging geometry and forces exerted on the incipient failure block.

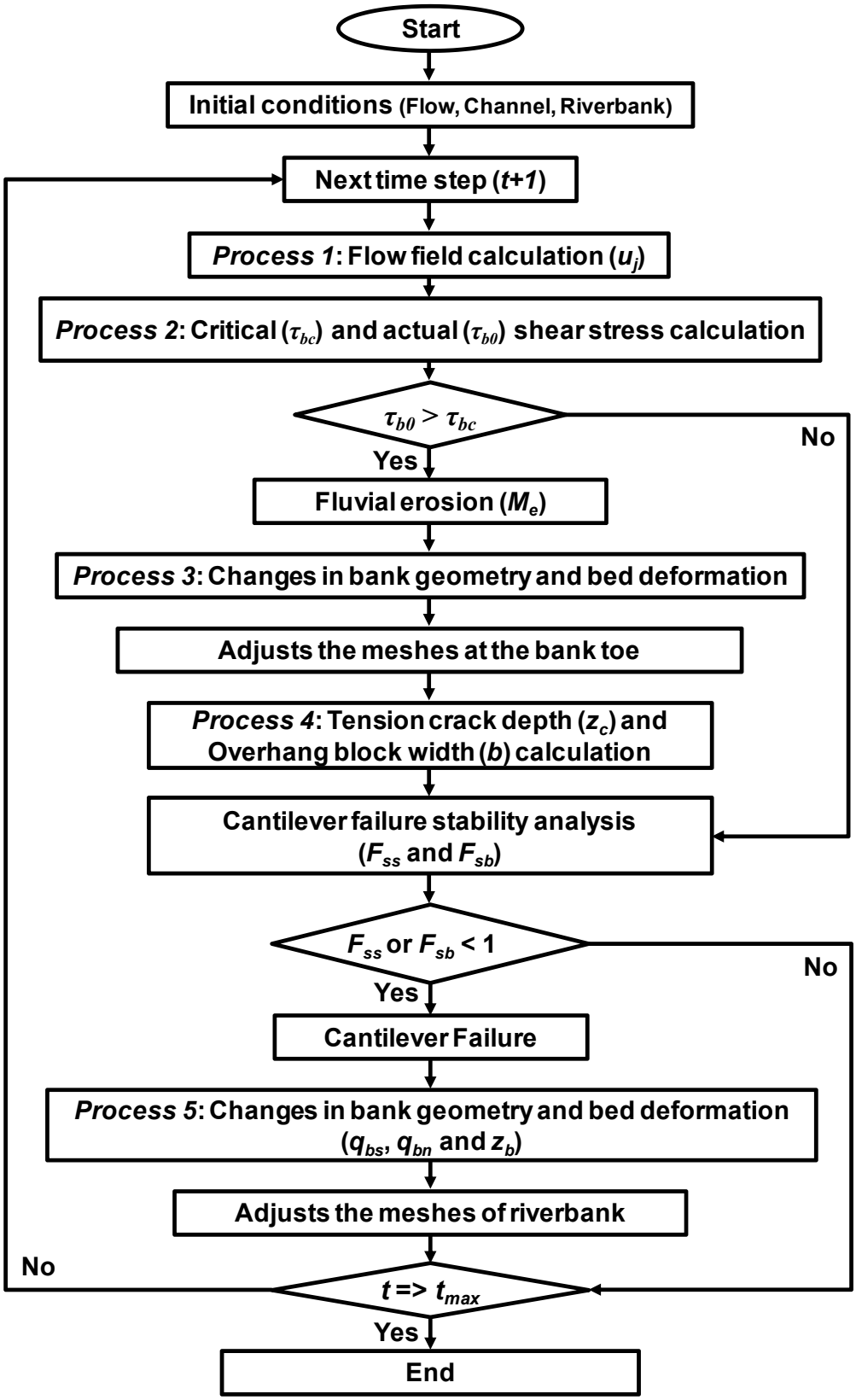


**Fig. 3.5** Logic diagram of the computational sequence.

The erosion coefficient is expressed by

$$E = \sin\bar{\beta}\sqrt{\frac{C_L^{'}}{2\rho_s}}\left(1 - C_* \cos\bar{\beta}\right) \tag{3.2}$$

where $E$ is the erosion coefficient ($(m^3/kg)^{1/2}$), $\bar{\beta}$ is the average cohesive riverbank angle, $C_L^{'}$ is the coefficient of the lift force $(C_L^2\ ln^2(0.35d_{50}/k_s)/\kappa^2)$ ($C_L$ is the coefficient of the lift force near the riverbank surface (0.178) and $\kappa$ is the von Kármán constant (0.4)), $\rho_s$ is the density of sediment particles (2,650 kg/m$^3$), and $C_*$ is the ratio of the equilibrium concentration of the suspended sediment (0.25).

The depth-averaged bank erosion rate from fluvial erosion ($\bar{\xi}$) can be quantified using an excess shear stress formula given by

$$\bar{\xi} = E\left(1 - \frac{\tau_{bc}}{\tau_{b0}}\right)^{3/2}\sqrt{\tau_{b0}} \tag{3.3}$$

where $\tau_{b0}$ is the actual shear stress $(\rho g u^2/c_c^2)$, $\rho$ is the density of water (1,000 kg/m$^3$), $c_c$ is the Chezy's roughness coefficient $(26.53D^{1/6}/d_{50}^{1/6})$ and $D$ is the water depth. The critical shear stress ($\tau_{bc}$) is estimated based on the percentage of silt-clay content (SC), which is obtained as $\tau_{bc} = 0.1 + 0.1779$ (SC) $+ 0.0028$ (SC)$^2 - 2.34E\text{-}5$(SC)$^3$ (Julian & Torres, 2006; Vanoni, 1977). In Eq. 3.3, only the portion of the riverbank where the actual shear stress is more than the critical shear stress is considered for the fluvial erosion estimation.

The rate of bank erosion can be considered proportional to the rate of depth-averaged bank erosion and can be expressed as

$$M_e = e\,\bar{\xi} \tag{3.4}$$

where $M_e$ is the rate of bank erosion (m/s) and $e$ is the coefficient that reflects the effect of a bank failure. The coefficient ($e$) can be determined by solving a series of equations with the functions of riverbank height and overhanging block dimensions, based on a heuristic approach. Further information can be obtained from Duan (2005).

For the computational process of fluvial erosion, the bank profiles are deformed to accord with the fluvial erosion simulated at the end discrete time step (Process 3 in **Fig. 3.5**). Therefore, the undisturbed cell occupation rate ($\Omega_t$) is achieved as expressed in Eq. 3.5 through two possible schemes (see **Fig 3.6**).

$$\Omega_t = \frac{\sum_{t=1}^{n} FE}{CW} \tag{3.5}$$

where CW is the width (m) of a calculated cell of the cohesive riverbank, estimated by the cohesive riverbank width divided by the number of calculated grid cells in the cohesive riverbank in the lateral direction, and FE is the simulated fluvial erosion in each time step using Eq. 3.4.

For the first scheme, if the accumulated magnitude of the simulated fluvial erosion is less than the width of a calculated cell of the cohesive riverbank, the boundary nodes are not shifted horizontally inward through the fluvial erosion (**Fig. 3.6(a)**). For the second scheme, if the accumulated fluvial erosion is equal to or larger than the width of a calculated cell of the cohesive riverbank, the new grid cells are assigned to the new cohesive riverbank profile nodes (**Fig. 3.6(b)**).

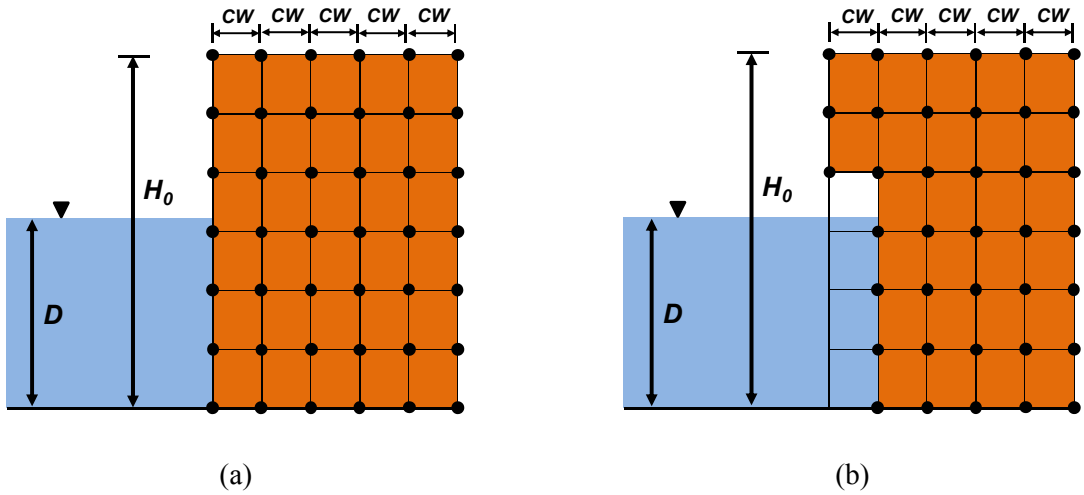


**Fig. 3.6** Two schemes used to adopt the boundary nodes by the effect of fluvial erosion (a) unmodified boundary nodes; (b) modified boundary nodes.

#### 3.2.2.2 Cantilever failure

For a cantilever failure, the overhanging failure blocks were defined by considering the safety factor for two types of failure (i.e., based on the shear-type and beam-type failure mechanisms) (Abam, 1997; Thorne & Tovey, 1981); tensile failure was omitted because such failures have rarely been observed along actual rivers (Darby et al., 2007). A cantilever failure will occur if any of the overhanging blocks have a safety factor of less than 1 (Process 4 in **Fig. 3.5**). The two types of cantilever failure mechanisms applied in this study are described by Abam (1997).

Shear-type failure involves shear stress along the vertical plane. Such failure is expected when the shear stress along the vertical plane from the weight of the overhanging block (*FD*) exceeds the cohesive force (*FR*), as shown in **Fig. 3.4**. The safety factor equation of shear failure ($F_{ss}$) is given by

$$F_{ss} = \frac{C\left(H' - z_c\right)}{2\gamma_s b H'} \tag{3.6}$$

where $C$ is the compressive strength per unit length (kN/m), $H'$ is the overhanging block height (m), $\gamma_s$ is the unit weight of soil (kN/m$^3$), $b$ is the overhanging block width ($C(T_Z^2) / 2\gamma H'$) as determined by Abam (1997), $z_c$ is the maximum depth of a tension crack ($2C/\gamma \tan(\pi/4 + \phi/2)$) ($T_z$ is the tensile zone length (m) and $\phi$ is the internal friction angle) based on the location of the overhanging block width (Terzaghi et al., 1996). However, the tension crack depth for this study was assumed to be 0.5 of the overhanging block height because the ration of tension crack depth and overhanging block height (0.3 to 0.7) does not typically change the factor of safety by more than 10% (Thorne & Abt, 1993).

Beam-type failure is related to the unstable overhanging blocks rotating from the cohesive riverbank forward into the channel. This occurs when the rotational moment at the neutral axis from the weight of the block subject to cantilever failure (*M*) exceeds the restoring moment of cohesive force. The safety factor of a beam-type failure ($F_{sb}$) can be described by

$$F_{sb} = \frac{T\left(T_Z^2\right)}{2\left[\gamma_s b^2 H' - C\frac{C_Z^2}{2}\right]} \tag{3.7}$$

where $T$ is the tensile strength per unit length (kN/m) and $C_z$ is the compressive zone length (m).

#### 3.2.2.3 Bedload transport and bed deformation

After fluvial erosion and a cantilever failure, the failure materials were dropped into the channel and assumed to be non-cohesive materials and bedload (Process 5 in **Fig. 3.5**). The equations describing the bedload transport and bed deformation are as follows.

The sediment transport rate in the streamwise direction ($q_{bs}$) was calculated using the formula proposed by Ashida & Michiue (1972)

$$q_{bs} = 17\tau_*^{3/2}\left(1-\frac{\tau_{*c}}{\tau_*}\right)\left(1-\sqrt{\frac{\tau_{*c}}{\tau_*}}\right)\sqrt{Ggd_{50}^3} \tag{3.8}$$

where $\tau_*$ is the non-dimensional bed shear stress ($u^*/(G\,g\,d_{50})$), $u^*$ is the shear velocity ($\sqrt{g\,R_j\,i}$), G is the specific weight of sediment (2.65) and $\tau_{*c}$ is the non-dimensional critical bed shear stress, using the formula of Iwagaki (1956).

The sediment transport rate in the lateral direction ($q_{bn}$) was calculated using the formula of Hasegawa (1984) by neglecting the effect of a secondary current as follows

$$q_{bn} = -q_{bs}\sqrt{\frac{\tau_{*c}}{\mu_s\mu_k\tau_*}}\frac{\partial z_b}{\partial y} \tag{3.9}$$

where $\mu_s$ is the static friction coefficient (1.0), $\mu_k$ is the kinetic friction coefficient (0.45), $Z_b$ is the bed elevation in the calculated cell and y is the coordinate components in the lateral axis.

The bed deformation was calculated using a continuity equation of sedimentation transport in an orthogonal coordinate, expressed as

$$\frac{\partial z_b}{\partial t} + \frac{1}{1-\lambda}\left(\frac{\partial q_{bn}}{\partial y}\right) = 0 \tag{3.10}$$

where $t$ is time and $\lambda$ is the porosity of the material (0.4), which is in a range of general value of the riverbank and riverbed (Dulal et al., 2010; Iwasaki et al., 2012). Moreover, the silt proportion in the sediment mixture was washed away to downstream end of the flume after the fluvial erosion and

cantilever failures in the experimental results. Therefore, the process of bed deformation of this study was considered only in pure sand sediment.

## 3.3 RESULTS AND DISCUSSION

### 3.3.1 Experimental Results

A summary of cantilever failure during each experiment is given with reference to images of spatial bank width observed in the experiments (illustrated through the results of Case 6 in **Fig. 3.7**) and to schematic diagrams of spatial bank width using top-view video cameras, as shown in **Fig. 3.8**. The failure processes determined in the experimental studies are as follows.

In Case 1, fluvial erosion occurred immediately, during the initial stage. The riverbank rotated into the channel approximately 1 min after the wooden panel was removed and the experiment was started, because the material was cohesionless.

In Case 2, from the initial time to $t$ = 13 min, fluvial erosion occurred at the bank-toe, whereas the first tension crack developed progressively at the upper surface at 13 min 45 s. At about 14 min, a beam-type failure occurred at the downstream end, followed by a beam-type failure at the upstream end at 19 min. A large tension crack and beam-type failure developed at the upstream end at 23 min 34 s and at 24 min, and the experiment was ended at 34 min.

In Case 3, the fluvial erosion dominated from the initial time up to 3 min. Four tension cracks and beam-type failures occurred at 3 min, 3 min 15 s, 5 min and 6 min 30 s. After beam-type failure, the bank slope reshaped toward an angle of approximately 90°. The experiment stopped at 8 min 30 s.

In Case 4, fluvial erosion developed from the start time up to 10 min. Six tension cracks and beam-type failures then occurred along the cohesive riverbank. The experiment ended at 18 min 30 s.

In Case 5, fluvial erosion occurred during the initial stage. The first considerable tension crack was observed in the middle region at 15 min 30 s. From 16 to 32 min, five successive tension cracks and beam-type failures were captured along the cohesive riverbank. The experiment reached the equilibrium stage at 45 min.

In Case 6, fluvial erosion occurred immediately after the wooden panel was removed. Tension cracks and beam-type failures were then observed in rapid succession at the downstream end at 10 min; at the upstream end at 11 min, 12 min 20 s and 13 min, at the downstream end again at 14 and 16 min, and at the upstream end again at 17 min and 18 min. The experiment reached the equilibrium stage at 20 min.

In Case 7, during the initial stage, fluvial erosion occurred along the bank but was more evident in the middle region. The first tension crack and beam-type failure were captured between 14 and 15 min 25 s. From 17 min 20 s to 33 min, eleven significant tension cracks and beam-type failures were observed along the riverbank. At 35 min, the cohesive riverbank reached its final configuration because no failures occurred after this time.

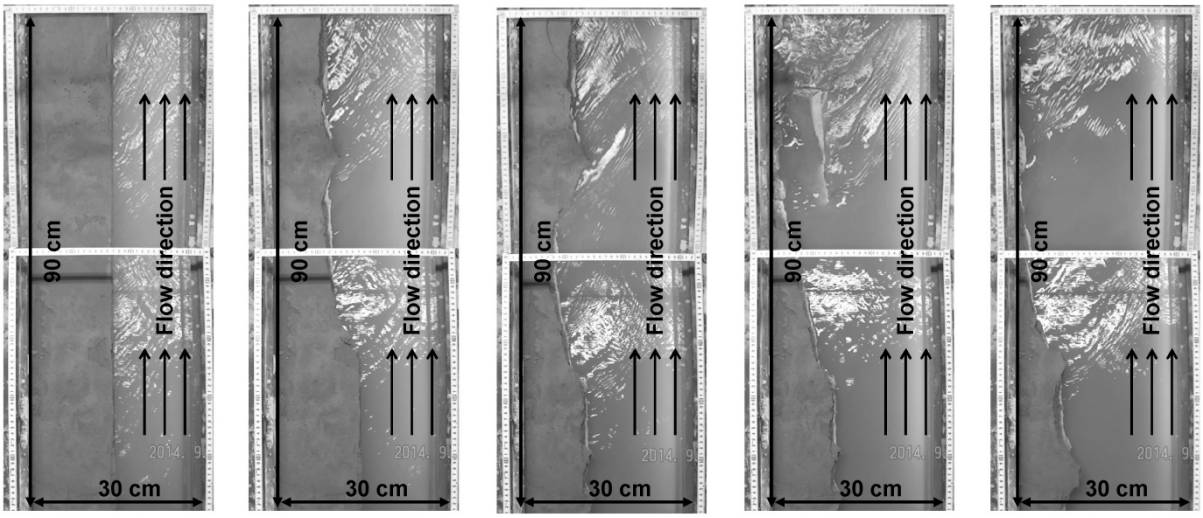


(a) initial stage. (b) 10 min. (c) 13 min. (d) 16 min. (e) 20 min.

**Fig 3.7** Experimental image results of spatial bank width in Case 6.

The experiments showed that fluvial erosion has the greatest effect on the occurrence of cantilever failure instability because such erosion increases the width of an overhanging block (observed using side view video cameras) but decreases its stability. This is because fluvial erosion is related to a loosening of weak bonds between the material particles. The observations from these experiments are similar to the those of previous studies (Abam, 1997; Darby et al., 2007; Rinaldi & Nardi, 2013; Thorne & Tovey, 1981). Tension crack and beam-type failure processes were then observed and repeated intermittently until the final stage of failure. The tension cracks began to develop vertically downwards from the upper surface of the overhanging block, thereby reducing the effective length of the vertical failure surface and decreasing the riverbank stability. Moreover, tension cracks seemed to develop only when the cantilever failure was already close to failure. The dimensions of the failure block were 2.97-9.98 cm wide and 11.76-62.14 cm long (see Table 3.2). In terms of the cantilever failure mechanisms, the present experimental results are consistent with previous experiments, showing that a beam-type failure is the dominant failure mechanism (Nardi et al., 2012; Samadi et al., 2013).

### 3.3.2 Numerical Results

To assess the accuracy and reliability of the proposed model, the numerical results were compared with the experimental results in terms of the streamwise-averaged bank width and water level at each time step, these being the average values of the bank width and water level along the center part of the cohesive riverbanks. In addition, the numerical results were validated using the spatial bank width and water level.

**Fig. 3.9** shows cross-sectional views at two time stages, simulated using the numerical model. **Fig. 3.9(a)** shows the fluvial erosion in the submerged zone. This process occurs through the fluvial entrainment of materials from the bank-toe, leading to an undermining that produces an overhanging block. **Fig. 3.9(b)** shows the beam-type failure of a cohesive riverbank, which is a common mechanism of a cantilever failure. Following the drop process of the numerical model, the failure materials were assumed to be non-cohesive materials that come to rest at the intermediate drop point.

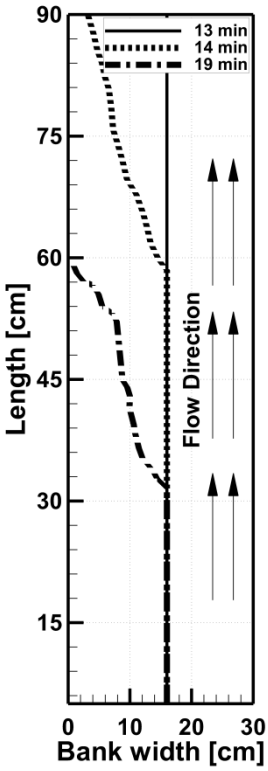


(a) Case 2.

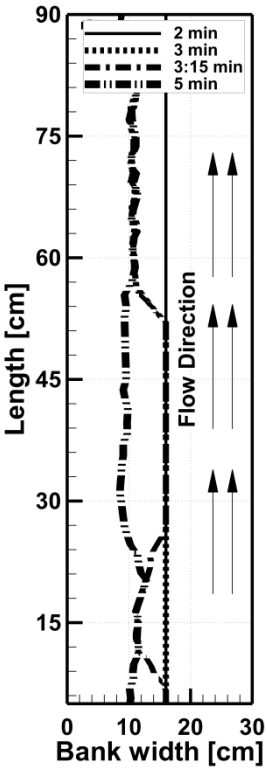


(b) Case 3.

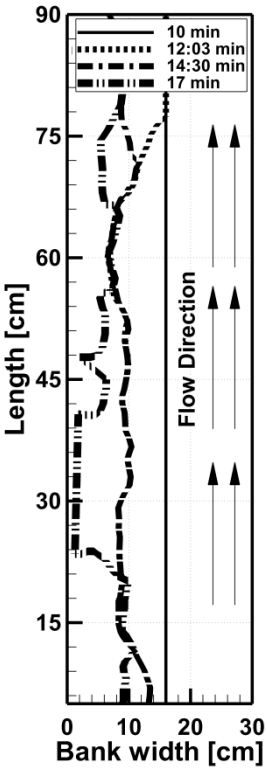


(c) Case 4.

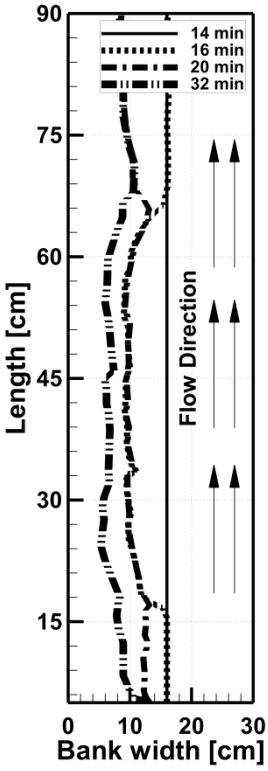


(d) Case 5.

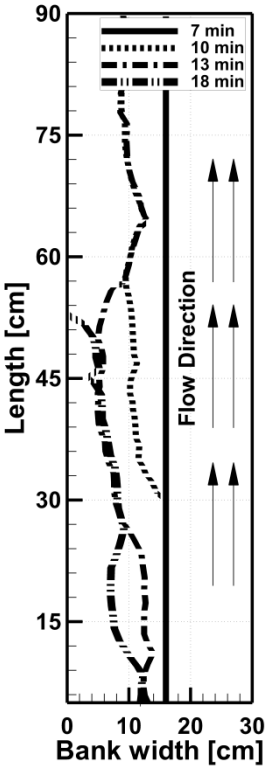


(e) Case 6.

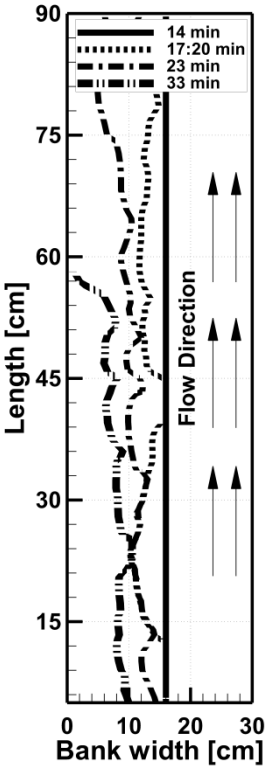


(f) Case 7.

**Fig 3.8** Schematic diagrams of spatial bank width.

Table 3.2 Summary of the failure time and failure block dimensions.

| Case | Variable | Failure time and failure block dimensions | | | | |
|---|---|---|---|---|---|---|
| | | I | II | III | IV | V |
| 2 | Failure time (min) | 14.00 | 19.00 | 24.00 | 30.00 | - |
| | Width (cm) | 8.36 | 8.30 | 6.29 | 5.21 | - |
| | Length (cm) | 31.35 | 28.46 | 27.99 | 11.76 | - |
| 3 | Failure time (min) | 3.00 | 3.15 | 3.25 | 4.30 | 5.00 |
| | Width (cm) | 5.57 | 2.97 | 5.41 | 4.03 | 9.98 |
| | Length (cm) | 34.53 | 12.04 | 22.24 | 14.50 | 28.33 |
| 4 | Failure time (min) | 12.00 | 14.00 | 16.00 | 17.00 | 18.00 |
| | Width (cm) | 6.30 | 7.55 | 3.95 | 7.30 | 5.63 |
| | Length (cm) | 59.70 | 18.2 | 13.25 | 27.62 | 44.46 |
| 5 | Failure time (min) | 15.00 | 16.00 | 19.00 | 19.30 | 30.00 |
| | Width (cm) | 5.76 | 6.08 | 6.31 | 3.06 | 3.95 |
| | Length (cm) | 29.41 | 18.53 | 24.87 | 14.76 | 62.14 |
| 6 | Failure time (min) | 8.00 | 8.30 | 8.40 | 11.00 | 13.00 |
| | Width (cm) | 5.07 | 5.01 | 6.84 | 3.29 | 5.22 |
| | Length (cm) | 13.22 | 19.27 | 22.37 | 19.21 | 34.50 |
| 7 | Failure time (min) | 15.25 | 17.40 | 21.10 | 23.00 | 33.00 |
| | Width (cm) | 3.86 | 3.15 | 4.01 | 3.15 | 4.24 |
| | Length (cm) | 20.98 | 15.02 | 13.72 | 29.58 | 17.98 |

The numerical and experimental results of a cantilever failure were also compared with a perfect agreement line, which fell within a range of 25% error line in terms of streamwise average bank width and 20% error line in streamwise average water level, as shown in **Fig. 3.10**. Several points fell outside the 25% error line (Case 2 and Case 4), which is why the numerical modeling did not consider the effect of the slump blocks. The effect of the slump blocks on the riverbed in front of the riverbank where it forms a sediment buffer that reinforces riverbanks and reduces fluvial erosion is described by Crosato (2008).

The relationships of streamwise-averaged water levels indicates that the calculated water level shows an increasing trend whereas the water surface stayed at a constant level during the experiments. This is because the failure materials in the experimental results were washed away to the downstream region of the experimental flume whereas, in the numerical modeling, it was assumed that the failure materials were dropped at the intermittent drop point. When the failure materials are dropped into the channel, the water level will increase along the channel. Nevertheless, streamwise-averaged bank

width and water level in the numerical simulations show relatively high degrees of accuracy, and those errors almost fluctuate from 20 to 25% of the experimental results.

Regarding the validation for spatial bank width and water level, the numerical model satisfactorily replicated the experimental results. As an example, the validations of spatial bank width and water level for Case 6 at 10, 11, and 13 min are shown in **Fig. 3.11** and **3.12**, respectively.

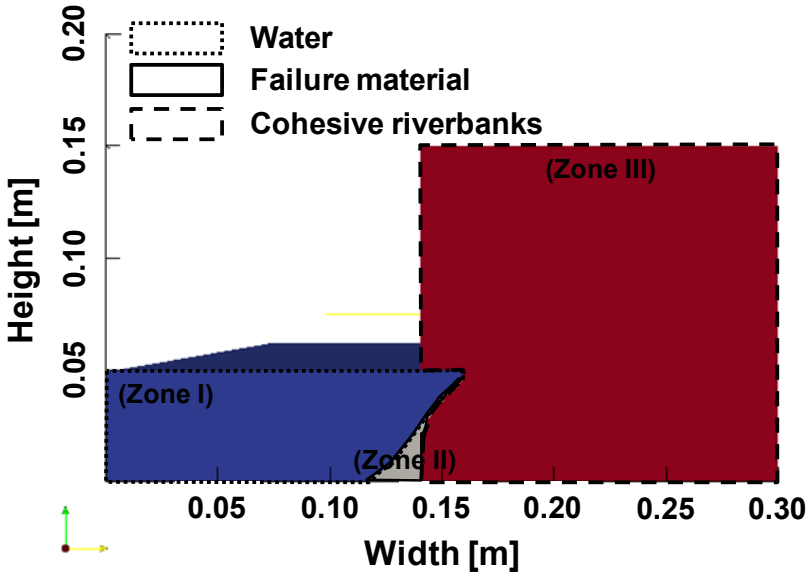


(a) Fluvial erosion.

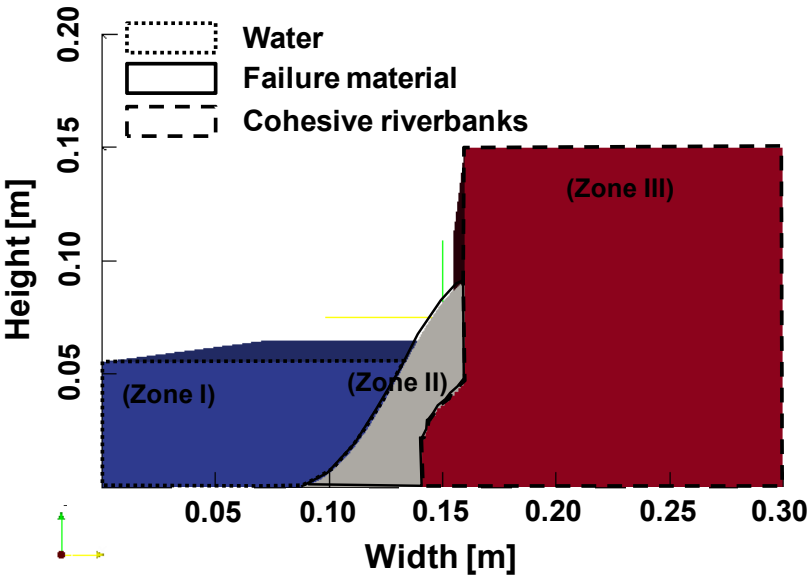


(b) Beam-type failure.

**Fig. 3.9** Cross-sectional views of fluvial erosion and beam-type failure mechanism of Case 3. (Zone I, II and III are water, failure material and cohesive riverbank, respectively.)

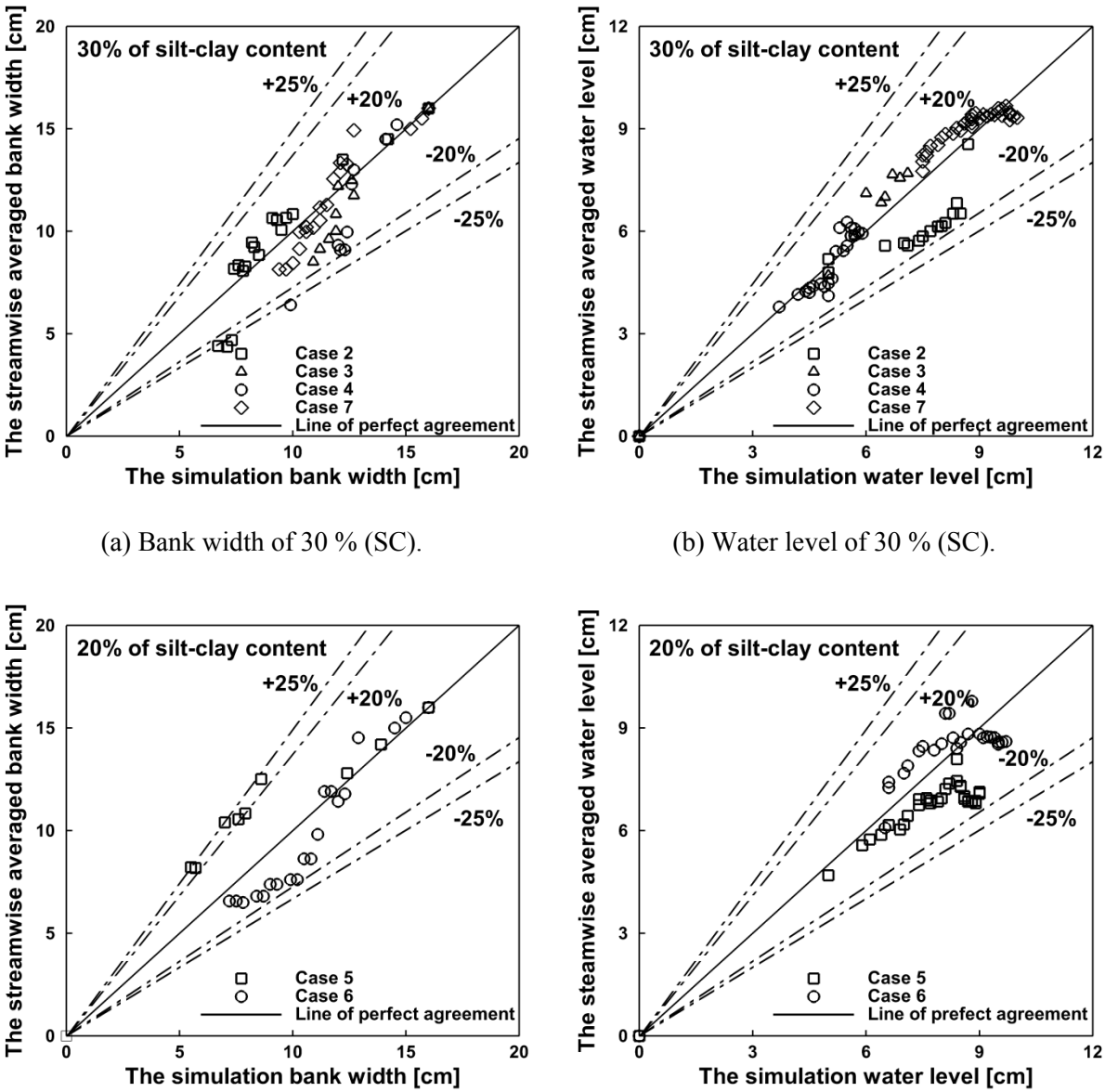


(a) Bank width of 30 % (SC).

(b) Water level of 30 % (SC).

(c) Bank width of 20 % (SC).

(d) Water level of 20 % (SC).

**Fig. 3.10** Comparison of numerical results and spatially averaged experimental results.

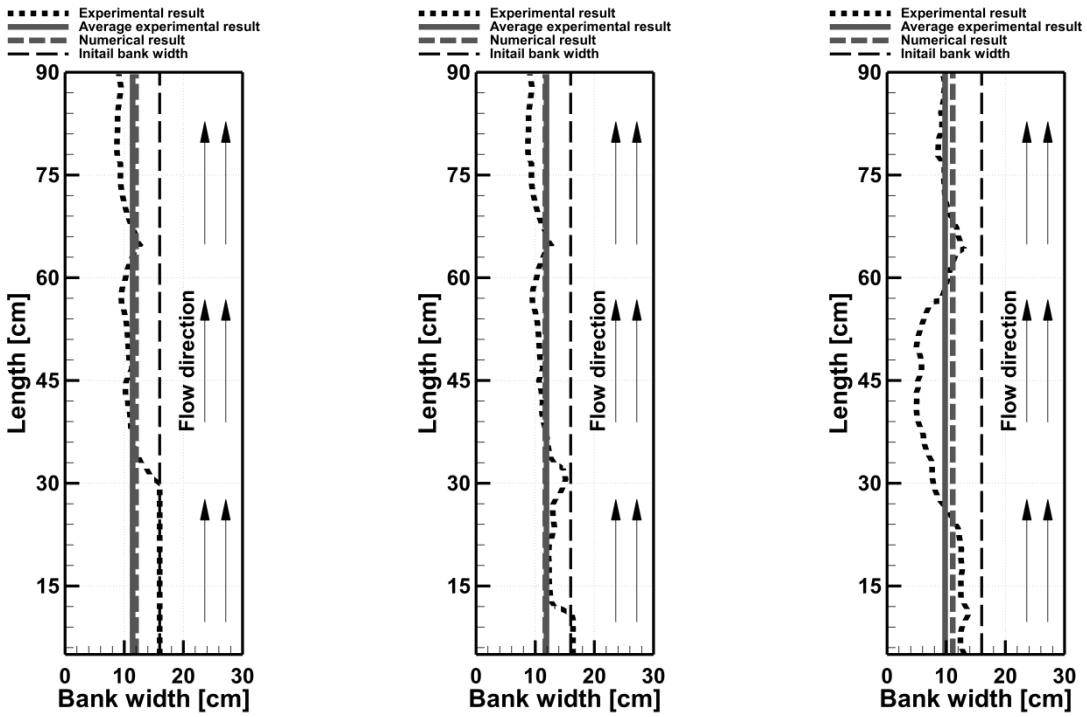


(a) 10 min (b) 11 min (c) 13 min

**Fig 3.11** Validation results for spatial bank width in Case 6.

### 3.3.3 Discussion

For the flow conditions, the Reynolds numbers (Re) were within the range of 15,000 to 40,000 and the Froude numbers (Fr) were smaller than 1 (Table 3.1), which corresponded to a turbulent flow and subcritical flow regimes, respectively. Generally, the Froude number is adopted here to represent a large number of alluvial rivers where the flow condition is subcritical flow (Dulal & Shimizu, 2010; Lewin, 1976; Peakall et al., 2007). Moreover, the channel aspect ratio was less than five (i.e., the flume width was less than five times the flow depth). That ratio is smaller than the aspect ratio in real rivers, but the smaller aspect ratio was chosen in order to clearly replicate the cantilever failure in the experimental flume. To overcome the aspect ratio discrepancy between the experimental flume and real rivers, the sidewall correction method was considered essential for this study. In the numerical model, the sidewall correction effect was calculated by a dividing channel method in which the streamwise velocity was calculated separately on each coarse lateral 1D grid cell.

For the experimental results, experiments using different overhanging block heights and cohesive forces were conducted to identify the effect of the overhanging block stability. The results indicate that the overhanging block height and cohesive force have a significant impact on the overhanging block stability (Samadi et al., 2011). For example, the experimental results show that the total experimental time for a higher bank (20 cm in Case 2) was longer than that of a lower bank (15 cm in Case 3). The main reason for that is the larger failure of the higher bank's materials dropping into the channel and being strongly protected from new fluvial erosion at the bank-toe. Furthermore, the rate of fluvial erosion in Case 3 (SC = 30%) was greater than that of Case 5 (SC = 20%) under similar hydraulic conditions in the experimental and numerical results, as shown by the temporal average bank width in **Fig. 3.13(a)**. For Case 3, the experiment was stopped at 8 min 30 s when the failure

proceeded throughout all of the cohesive riverbanks. Moreover, the Case 5 experiment reached the equilibrium stage at 45 min because riverbanks with a higher silt-clay content are more susceptible to failure than those with lower silt-clay content. Observations from the other works are similar in terms of changing silt-clay content (Couper, 2003; Dulal & Shimizu, 2010; Julian & Torres, 2006). For numerical results, the rate of fluvial erosion in Case 3 was greater than that in Case 5 under similar conditions, as shown in **Fig. 3.13(b)**. Moreover, the numerical results are consistent with the experiment results with regards to the changing percentage of silt-clay content.

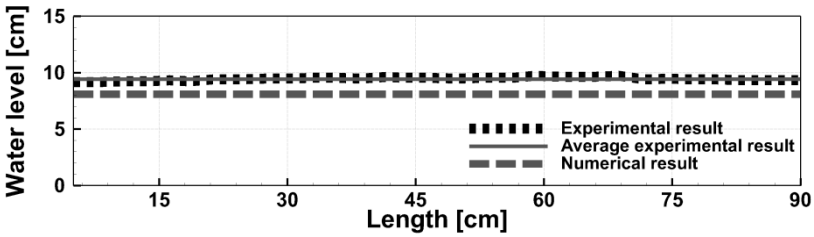


(a) 10 min.

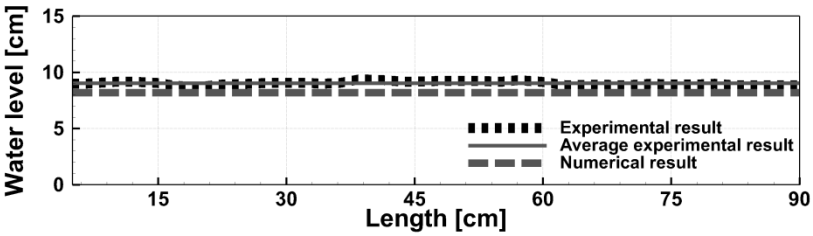


(b) 11 min.

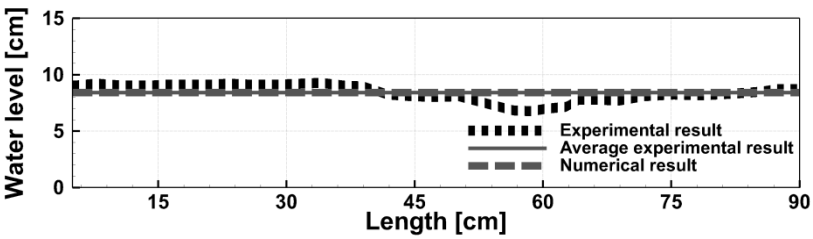


(c) 13 min.

**Fig 3.12** Validation results for spatial water level in Case 6.

Another significant parameter in cantilever failure is the cohesive force. The cohesive force of riverbanks is related mainly to the percentage of silt-clay content (Couper, 2003; Dulal & Shimizu, 2010; Julian & Torres, 2006) and water content (Couper, 2003; Rinaldi & Nardi, 2013; Thorne & Tovey, 1981). Additionally, the percentage of silt-clay content could be expected to have some bearing on the susceptibility of the cohesive riverbanks to subaerial erosion processes, as the cohesive materials with a high silt-clay content have greater plasticity and hence capacity for swelling and shrinkage. For overhanging block stability, the cohesive force is a main parameter for calculating the safety factor of the overhanging block in Eqs. 3.6 and 3.7. In both equations, the safety factor of the overhanging block with a high cohesive force is larger than the safety factor of an overhanging block with low cohesive force.

The experiments were able to randomly reproduce a cantilever failure — as illustrated in **Fig. 3.8** — and some of the experimental results showed the backward erosion process. Furthermore, most of experimental results in the case of high actual shear stress (high discharge) showed backward erosion, which is similar to previous observations (Hooke, 1980; Laubel et al., 2003). In the present study, riverbank particles were detached from the downstream region through the effect of a second wooden panel by the generation of a reverse flow. This process is summarized as follows. The flow from the channel hits a second wooden panel and is reversed, with the high velocity, to erode the cohesive riverbank at the downstream region. For this reason, this study considered only the center region and used streamwise-averaged data of cohesive banks to reduce the effect of the wooden panel. Experimental limitations were the effect of scale and friction factor between the cohesive riverbanks and experimental wall. The experiments were conducted at a smaller scale than the prototype because it was hoped to obtain cantilever failure information in expected patterns of response more rapidly and with a closer control over the model details than would be possible using a full-scale experiment (Muir, 2004; Samadi et al., 2013).

As in the numerical model, the present uniform flow model has limitations in reproducing variations of the phenomena in the streamwise direction of the eroded riverbank. Therefore, a 2D depth-averaged model is needed to reproduce the flow fields of eroded non-uniform riverbanks along a channel (Bahar & Fukuoka, 2002). Moreover, the present numerical model is a simple cross-sectional 2D model. Such a model is limited in its ability to simulate non-uniform cantilever failure, the longitudinal gradient of sediment transport and pore water pressure. The proposed model should thus be improved in future research so that it considers the effect of such phenomena.

## 3.4 SUMMARY

This study elucidated the mechanisms of a cantilever failure by means of laboratory experiments and numerical modeling. In laboratory experiments, three types of cohesive materials with different percentages of silt-clay content were investigated in seven cases by varying the hydraulic conditions. The novel numerical modeling of a cantilever failure implemented by a triple-grid approach within the framework of fluvial erosion and the cantilever's subsequent failure was validated by the experimental results. The main summary from the results are as follows.

For the mechanism of a cantilever failure, the experimental results showed that the fluvial erosion at the lower part generates an overhanging block in the upper part of the cohesive riverbanks. Tension cracks then develop at the upper surface of the cohesive riverbanks. Such tension cracks seem to develop only when the cantilever failure is already close to failure. After that, cantilever failure occurred along the tension crack line. The dominant failure mechanism was observed to be beam-type failure, which is consistent with the findings of previous researchers who have suggested that the beam-type failure may be prevalent (e.g. Darby et al., 2007; Samadi et al., 2011, 2013; Thorne & Tovey, 1981). Moreover, the results indicate that cohesive riverbanks with higher silt-clay contents are more susceptible to failure than those with lower silt-clay contents. The observations from the this works are similar to previous studies in term of changing silt-clay content (Couper, 2003; Dulal & Shimizu, 2010; Julian & Torres, 2006).

The developed numerical model can satisfactorily reproduce fluvial erosion at the lower part of cohesive riverbanks and beam-type failure at an overhanging block of cohesive riverbanks. Additionally, the numerical model shows good agreement with the experimental results in terms of the spatial-averaged bank width and water level along the cohesive riverbanks. The experimental

results were presented and compared qualitatively with the numerical results. It is, however, still necessary to examine the validity of the slump block model for this work and compare the calculated results with more experimental studies and local observations.

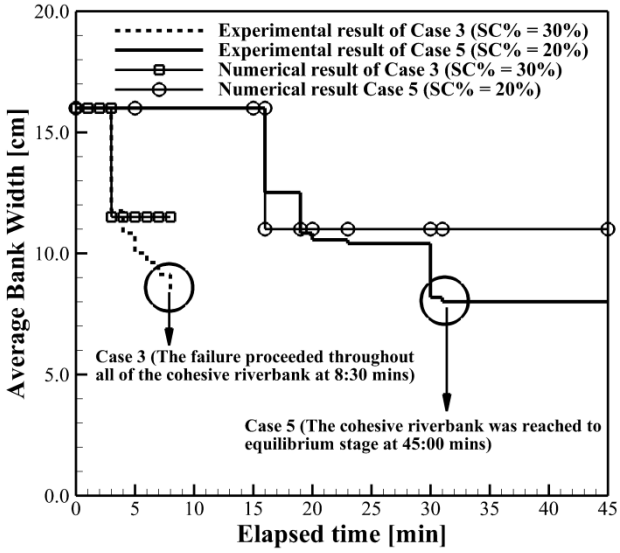


(a) The average bank width of the experimental and numerical results.

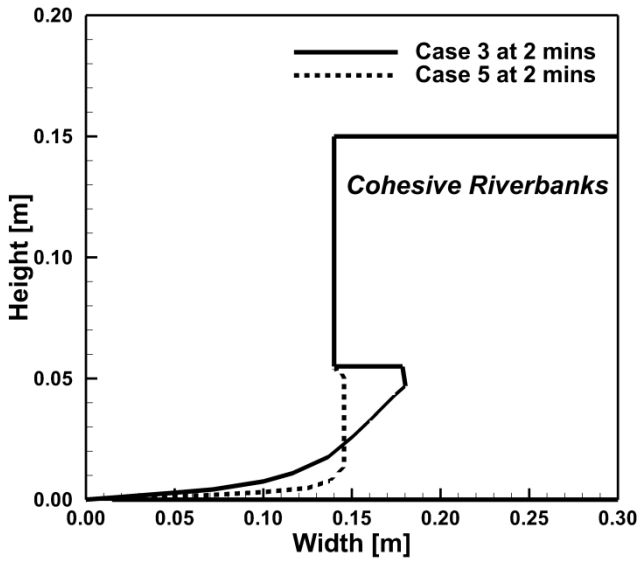


(b) The riverbank geometry of the numerical results.

**Fig 3.13** Comparison results between the experimental and numerical results with the different cohesive force of Case 3 (SC = 30%) and Case 5 (SC = 20%).

# Chapter 4

# COUPLED STUDIES OF FLUVIAL EROSION AND CANTILEVER FAILURE FOR COHESIVE RIVERBANKS: CASE STUDIES IN THE EXPERIEMNTAL FLUMES AND U-TAPAO RIVER

## 4.1 INTRODUCTION

An important source of extensive sediment production in natural alluvial channels is riverbank failure, in particular, a cantilever failure along an alluvial channel. Moreover, this phenomenon creates several environmental problems and socioeconomic issues, for instance, loss of fertilization in agricultural areas and destruction of surrounding infrastructure (Rinaldi & Darby, 2008; Taghavi et al., 2010). Therefore, studies on coupling fluvial erosion, cantilever failure, and bedload sedimentation are required to elucidate the complex mechanism of cantilever failure occurring along cohesive riverbanks.

In terms of riverbank stability analyses, previous researchers have been unable to analyze cantilever failures, and have focused predominantly on using a critical shear stress concept for the slope stability analysis of steep riverbanks (Osman & Thorne, 1988), riverbank retreat due to fluvial erosion and mass failure under gravity (ASCE, 1998), and the rate of riverbank erosion due to the hydraulic force acting on the riverbank surface (Duan, 2005).

For the analytical study of cantilever failure, a limited number of studies have applied stability analyses based on the factor of safety of the portion subject to cantilever failure, for which three possible cantilever failure mechanisms have been defined: shear-type, beam-type and tensile-type failures (Abam, 1997; Thorne & Tovey, 1981). In addition, the tensile strength equation of the tension crack at the time of failure is expressed in terms of the overhanging block weight and geometrical dimensions (Fukuoka, 1994).

Several previous studies have reported small-scale cantilever failure experiments, including experimental studies examining the fluvial erosion and cantilever failure mechanisms (Fukuoka et al., 1999), as well as experimental works measuring flow characteristics near and inside the eroded cohesive banks (Bahar & Fukuoka, 2002). Recently, several large-scale experimental studies on cantilever failure mechanisms were reported. For instance, experiments were conducted to estimate the failure plane angle, and tension crack depth (Taghavi et al., 2010). In addition, experimental studies were conducted to investigate the dominant cantilever failure mechanisms; the studies show that beam-type and tensile-type failures are dominant (Samadi et al., 2013). Moreover, experiments were carried out to investigate mass failures in a sandy gravel bank, and to show the occurrence of a variety of failure processes, such as cantilever, slab, and slide (Nardi et al., 2012).

To aid understanding of the complex mechanisms of cantilever failure, several numerical studies have been developed. For example, a semi-implicit method of applying a pressure-linked equation algorithm was employed to reproduce flow characteristics near and inside eroded banks (Bahar & Fukuoka, 2002). In addition, the shear-type, and beam-type failure mechanisms were studied to identify the significant effects of the uncertainty parameters on the reliability of a bank stability model in determining cantilever failure. The results showed that the overhanging block dimensions, and the cohesive force are highly significant for an analysis of overhanging block stability (Samadi et al., 2011). A stress-strain behavior model for cantilever failure was applied to simulate the subsequent failure of an overhanging block by the limited equilibrium method, defined as the ratio between stabilizing and destabilizing forces (Samadi et al., 2013). In addition, a coupled model of fluvial erosion and mass wasting failure was developed to reproduce fluvial erosion in the bank-toe, degradation in bed channel, and destabilization by only considering shear-type failure of an upper bank (Darby et al., 2007; Duan & Julien, 2010; Langendoen et al., 2008; Motta et al., 2014; Rinaldi et al., 2008).

Furthermore, a coupling model of fluvial erosion, cantilever failure, and bedload sedimentation was proposed to simulate the subsequent cantilever failure by considering two types of cantilever failure, which are shear-type and beam-type failures (Patsinghasanee et al., 2015b, 2015c). The main limitation of this previous study was in the quantification of the fluvial erosion rate ($\varepsilon$) derived from the erodibility coefficient, because the determination of erodibility coefficient remains complex, and is dependent on several factors, including the water content, cohesive force, and silt-clay content (Couper, 2003; Grabowski et al., 2011; Julian & Torres, 2006).

To address the gap in coupling fluvial erosion, cantilever failure and bedload sedimentation, the previous empirical and analytical equations of the actual shear stress, critical shear stress, erodibility coefficient, and factor of safety of the shear-type and beam-type failures were employed to describe the overhanging block properties, and to determine the fluvial erosion rate and the overhanging block stability in the existing experimental works (see details in Chapter 3) and the natural riverbanks of the U-Tapao River, Songkhla Province, Thailand. In addition, an existing numerical model (see numerical model information in Chapter 3) was modified using the appropriate empirical and analytical equations, and validated by the temporal variations of spatially averaged bank width, cantilever failure type, and overhanging failure dimensions of the existing experimental works, and the U-Tapao River.

## 4.2 METHODOLOGY

This section provides an overview of an existing experiment (Chapter 3), the U-Tapao River, and a modeling description of the implementation in the coupled study of fluvial erosion, cantilever failure, and bedload sedimentation.

### 4.2.1 Laboratory Experiment

This chapter used the data from an existing experiment (Chapter 3) (Patsinghasanee et al., 2015b, 2015c), which was conducted for fully understanding the mechanism of a cantilever failure. Since the details of design, and aim of this experiment have been described in the previous chapter, herein only a brief overview is presented.

The existing experiments were conducted in a straight rectangular channel, 30 cm in width, 10 m in length, and 20 cm in height. The channel slope was set as 1/500. In the upstream region of the channel, a wooden board was installed to avoid fluvial erosion (I to II). At the middle reach of the channel (3.8 to 5.2 m upstream), a cohesive bank formed. The dimensions of the cohesive bank were 16 cm in width, 1.4 m in length, and a variable height of 15 to 20 cm. In the downstream region of the cohesive bank, a second wooden board was installed to provide protection from fluvial erosion (III to IV) (**Fig. 4.1**).

In these experiments, the sediment was composed of sand and silt with mean diameters ($d_{50}$) of 0.23 mm and 28.4 μm, respectively. The sediment mixture was initially wetted with water to achieve a water content in the range of 32.2 to 48.0%. Cohesive banks were compacted by applying a static load of 0.04 kg/cm$^2$ for 72 h, to allow sufficient consolidation. Prior to conducting the experiments, the cohesive materials were tested to determine the cohesive force, and internal friction angle by using a direct shear device based on the ASTM D3080-98 standard test method for direct shear testing of soil under consolidated drained conditions (ASTM, 1998). This test was consolidated by gradually increasing the normal stress in accordance with ASTM D2435-96 (ASTM, 1996). Moreover, the soil samples were carefully trimmed to fit within the shear box dimensions, and were placed in the shear box. Following this, the cohesive materials were consolidated through normal stress under loads of 5, 10, and 20 kPa for 24 h. The horizontal and vertical deformations, and corresponding applied shear stresses were then recorded simultaneously. Summary of the experimental conditions and cohesive bank properties are summarized in Table 4.1.

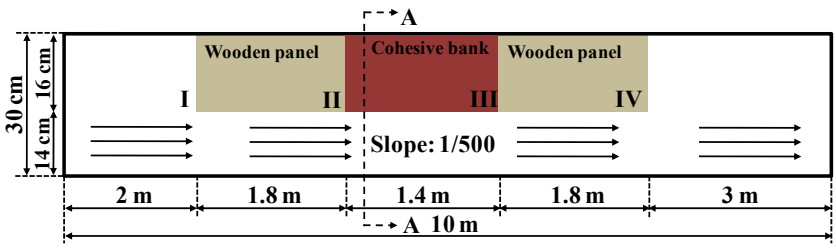


(a) Top view of experimental flume.

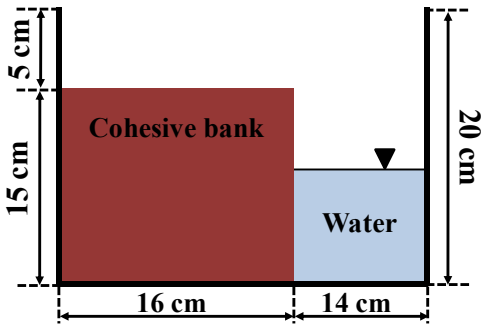


(b) Cross-section of experimental flume (A-A section).

**Fig 4.1** Dimensions of a straight experimental channel.

Table 4.1 Summary of the existing experimental conditions.

| Case | Discharge (l/s) | Bank height (cm) | Silt-clay content (%) | Water content (%) | Internal friction angle (°) | Cohesive force (kPa) | Re | Fr |
|---|---|---|---|---|---|---|---|---|
| 1 | 4.0 | 20 | 30 | 39.6 | 34.3 | 5.76 | 25,000 | 0.78 |
| 2 | 4.0 | 15 | 30 | 39.6 | 34.3 | 5.76 | 25,000 | 0.78 |
| 3 | 2.4 | 15 | 30 | 39.6 | 34.3 | 5.76 | 15,000 | 0.74 |
| 4 | 4.0 | 15 | 20 | 32.2 | 41.3 | 6.41 | 25,000 | 0.78 |
| 5 | 5.8 | 15 | 20 | 32.2 | 41.3 | 6.41 | 36,250 | 0.81 |
| 6 | 6.4 | 15 | 30 | 48.0 | 39.8 | 5.37 | 40,000 | 0.82 |

A summary of the tension crack, and cantilever failure is shown with reference to the images of temporal bank width as observed in the experiments (illustrated in **Figs. 4.2(a)** and **4.2(b)**), and the schematic diagram of temporal bank width as reported in **Fig. 4.2(c)**. The experimental results show that fluvial erosion has the greatest effect on the occurrence of cantilever failure instability because such erosion increases the width of an overhanging block, but decreases its stability. This is because fluvial erosion is related to the loosening of weak bonds between the material particles. Tension cracks then developed on the upper surface of the cohesive banks. Such cracks seemed to develop only when the cantilever was already close to failure. Following this, cantilever failure occurred along the tension crack line. The dominant failure mechanism was observed to be beam-type failure.

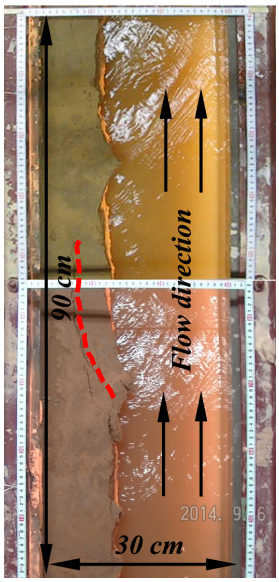


(a) Tension crack at 15 mins 30 s.

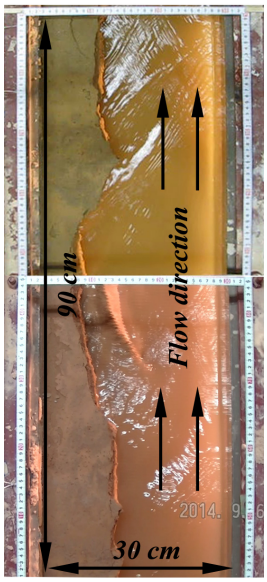


(b) Beam-type failure at 16 mins.

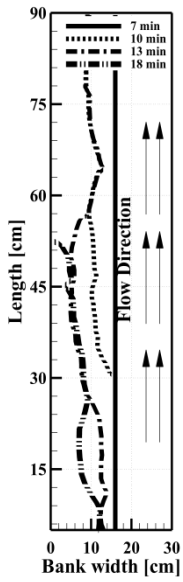


(c) Schematic diagram.

**Fig 4.2** Experimental image results and schematic diagrams of temporal bank width of Case 5.

### 4.2.2 The U-Tapao River

The U-Tapao River is located within the Songkhla Lake River Basin, Songkhla Province, Thailand (**Fig. 4.3**). For this study, the selected sites are located at the middle region of the U-Tapao River, which are almost straight channel, named UT.1, UT.2, UT.3, and UT.4 (Semmad, 2010). The coordinates in the EPSG: 4326 - Geographic WGS 84 of the study sites are shown in Table 4.2.

Moreover, the riverbanks regularly experience instability due to erosion at a moderate rate, particularly in the rainy season from July to February. The significant failure types in the U-Tapao River are planar and cantilever failures (Semmad, 2010). In general, the annual rainfall is 1,627 mm due to the tropical climate of this region (Department of Water Resources, 2007). Furthermore, the riverbed and riverbank materials do not vary significantly within the study sites, with a mean diameter of approximately 0.34 mm, as shown in the example of the grain size distribution at different depths from the top of the riverbank to the riverbed of section UT.3 in **Fig. 4.4**. In terms of riverbank properties, the soil materials are low plasticity clay with a percentage of silt-clay content (SC) in the range of 50.1 to 82.5%, an internal friction angle ($\phi$) from 22.58° to 28.96°, an erodibility coefficient ($k_d$) from approximately 0.07 to 21.33 $cm^3/(N\ s)$, a critical shear stress ($\tau_{bc}$) within the range of 9.44 to 12.99 Pa, a unit weight of soil ($\gamma_s$) from 18,970 to 20,120 $N/m^3$, and a plasticity index ($I_w$) from 12.1 to 23.53 (Semmad, 2010).

Table 4.2 Coordinates of the study sites in the U-Tapao River.

| Name | Coordinates | |
|---|---|---|
| | X | Y |
| UT.1 | 100.440 | 6.931 |
| UT.2 | 100.458 | 6.973 |
| UT.3 | 100.460 | 6.967 |
| UT.4 | 100.459 | 6.965 |

### 4.2.3 The Coupled Study of Fluvial Erosion and Cantilever Failure

As noted previously, the previous studies have limitations in terms of coupling fluvial erosion ,cantilever failure, and bedload sedimentation. Moreover, the quantification of erodibility coefficient remains complex, and it depends on several factors. Therefore, the main objective of this study is to provide a physical overview of a coupled study by applying different equations for critical shear stress, and the erodibility coefficient to elucidate the mechanism of cantilever failure in the experimental channel, and the U-Tapao River.

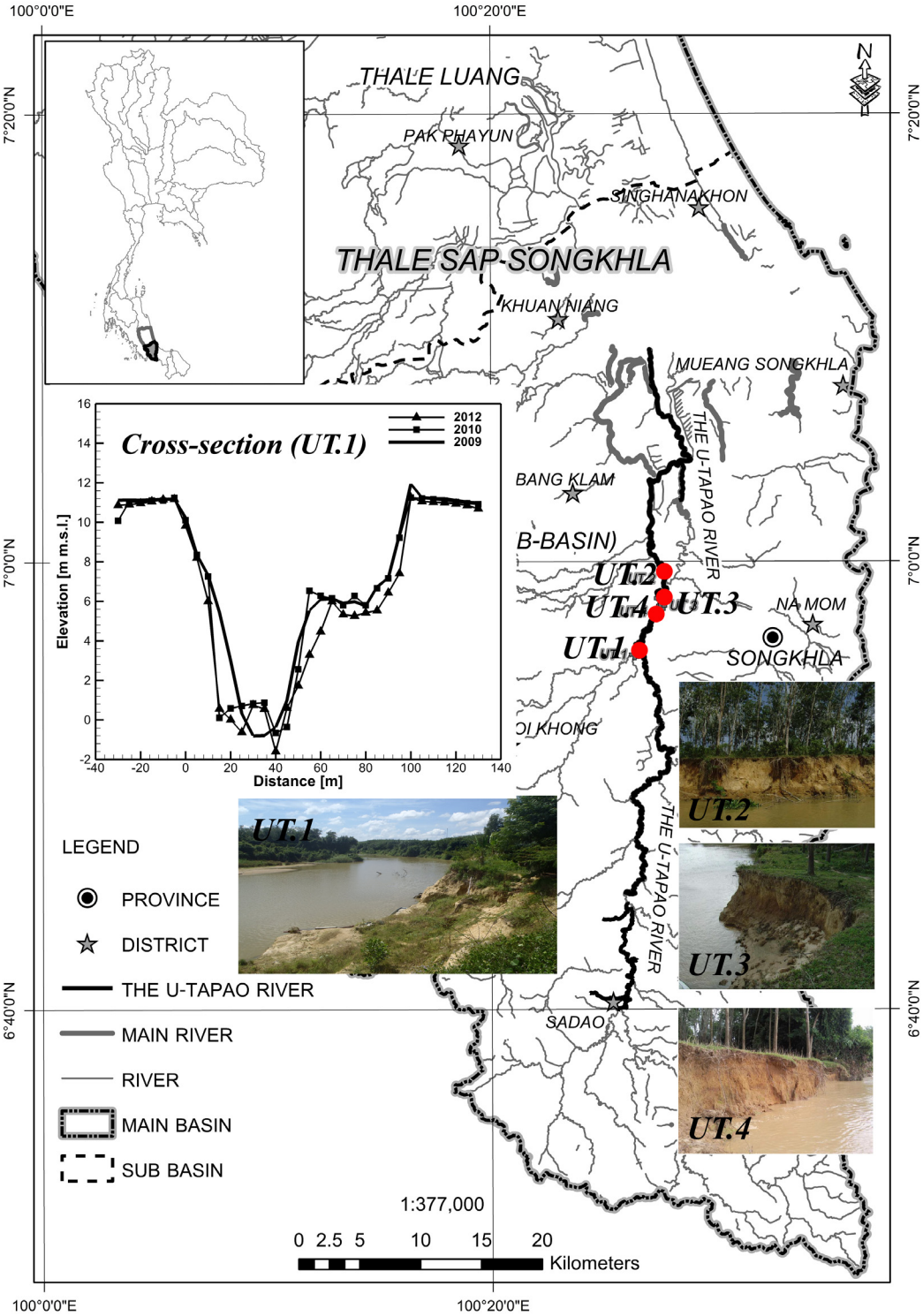


**Fig. 4.3** Study locations along the U-Tapao River, Songkhla Province, Thailand.

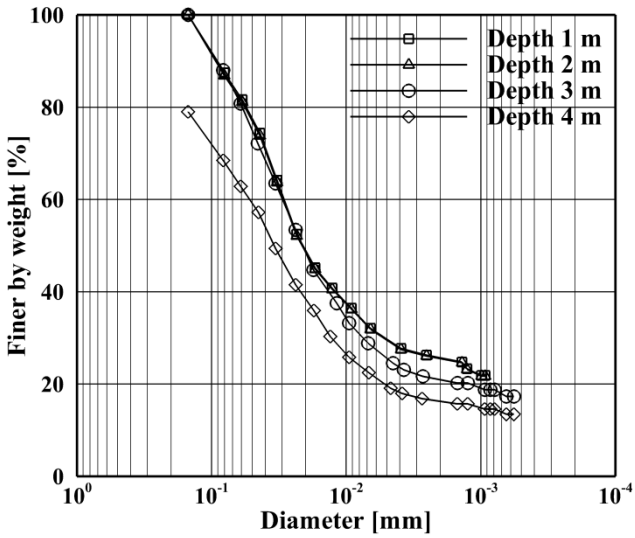


**Fig. 4.4** Grain size distribution of UT.3.

A coupling model was developed by implementing a triple-grid approach, consisting of a coarse one-dimensional (1D) grid for the flow field in the lateral direction; a fine 1D grid for sediment transport, and bed deformation in the lateral direction; and a 2D grid for cantilever failure in the vertical and lateral directions (**Fig. 4.5**). The assumptions for the coupling fluvial erosion, and cantilever failure are illustrated in **Fig. 4.6**. In the initial stage, the fluvial erosion is reproduced at the lower part of a cohesive bank, as shown by the dash-dotted line in zone I. The fluvial erosion has the greatest effect on the incidence of cantilever failure instability because this erosion increases the overhanging block width, but decreases the factor of safety with respect to both shear-type, and beam-type failures. Following this, the tension crack depth, and location are developed in zone II. The tension cracks begin to develop vertically downwards from the upper surface of the overhanging block. They reduce the effective length of the vertical failure surface, and decrease the bank stability. Moreover, tension cracks seem to develop only when the cantilever is close to failure. Then, the factors of safety of shear-type and beam-type failures of an overhanging block in zone III (the vertical broken line along the cohesive bank) are determined by the analytical equations. The logic diagram of the computational sequence used for the coupled mechanism of fluvial erosion, cantilever failure, and bedload sedimentation is illustrated in **Fig. 4.7**.

#### 4.2.3.1 Fluvial erosion

The flow field is calculated using a uniform flow model on a coarse lateral 1D grid cell (Process 1 in **Fig. 4.7**), considering the sidewall correction effect in the narrow experimental channel (Sturm, 2001). Moreover, the flow field equation can consider the complicated shape of fluvial erosion near the bank by evaluating the hydraulic radius in each calculated cell, and is written as follows:

$$u_j = \frac{1}{n} R_j^{2/3} i^{1/2} \tag{4.1}$$

where $u_j$ is the velocity in each calculated cell; n is the Manning roughness parameter along the channel (0.011), calculated using the Manning–Strickler equation ($k_s^{1/6}/7.66g^{1/2}$); $g$ is the gravity acceleration (9.81 m/s$^2$); $k_s$ is the relative roughness height defined as 1-3$d_{50}$ (1.5$d_{50}$); $R_j$ is the

hydraulic radius in each calculated cell ($A_j/P_j$); $A_j$ is the cross-sectional area in each calculated cell; $P_j$ is the wetted perimeter length in each calculated cell; i is the bed slope; and j is the lateral calculated cell number.

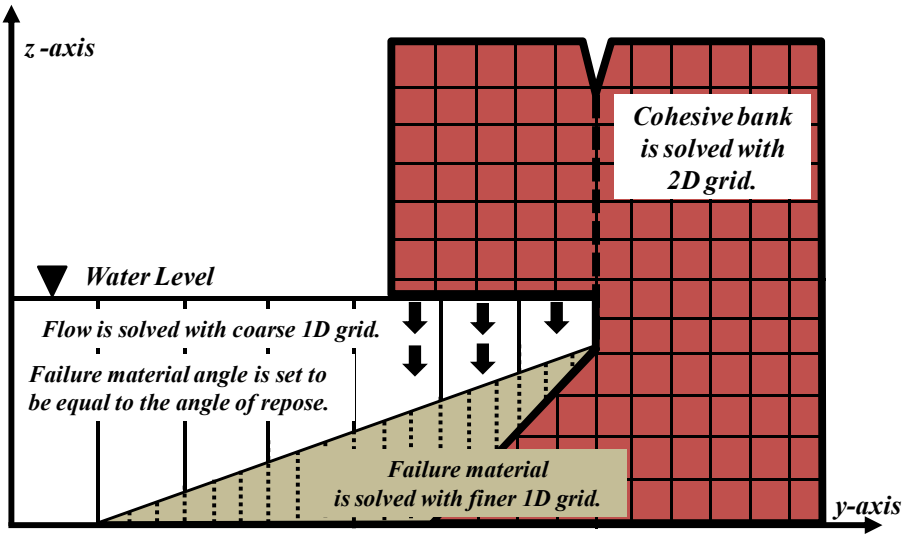


**Fig. 4.5** Framework of triple-grid approach of a coupling model.

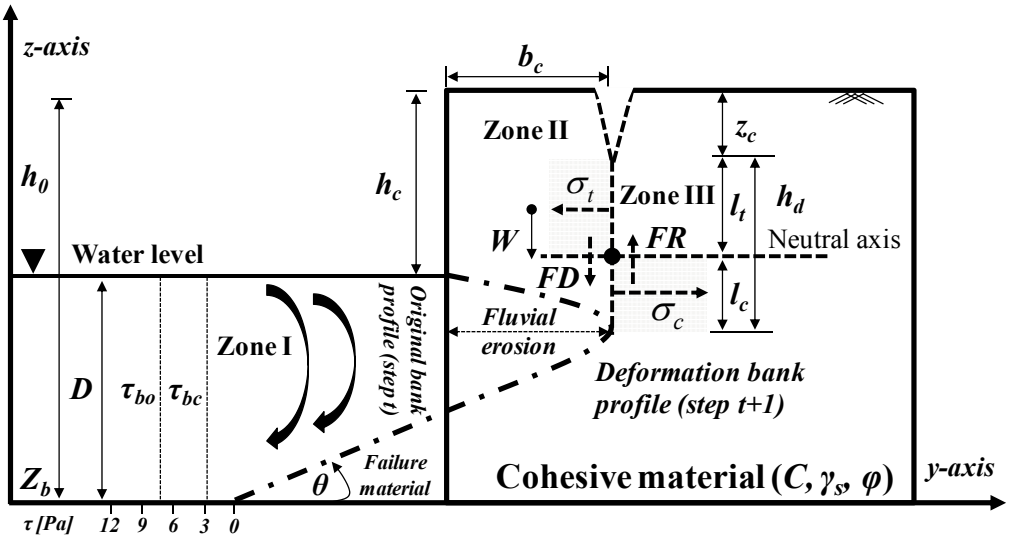


**Fig. 4.6** Overhanging geometry and forces exerted on the incipient failure block in a coupling model. $h_0$ is the initial bank height (m), $h_c$ is the overhanging block height (m), $h_d$ is the effective length of vertical failure surface (m), $b_c$ is the overhanging block width (m), $z_c$ is the tension crack depth (m), $D$ is the water depth (m), $\tau_{bo}$ and $\tau_{bc}$ are the actual shear stress and critical shear stress (Pa), $l_t$ and $l_c$ are the tensile zone length and compressive zone length (m), $W$ is the overhanging block weight (kN), $\sigma_t$ and $\sigma_c$ are the tensile stress and compressive stress (kN/m$^2$), $\theta$ is the angle of repose, $C$ is the cohesive force (Pa), $\phi$ is the internal friction angle and $\gamma_s$ is the unit weight of soil (kN/m$^3$).

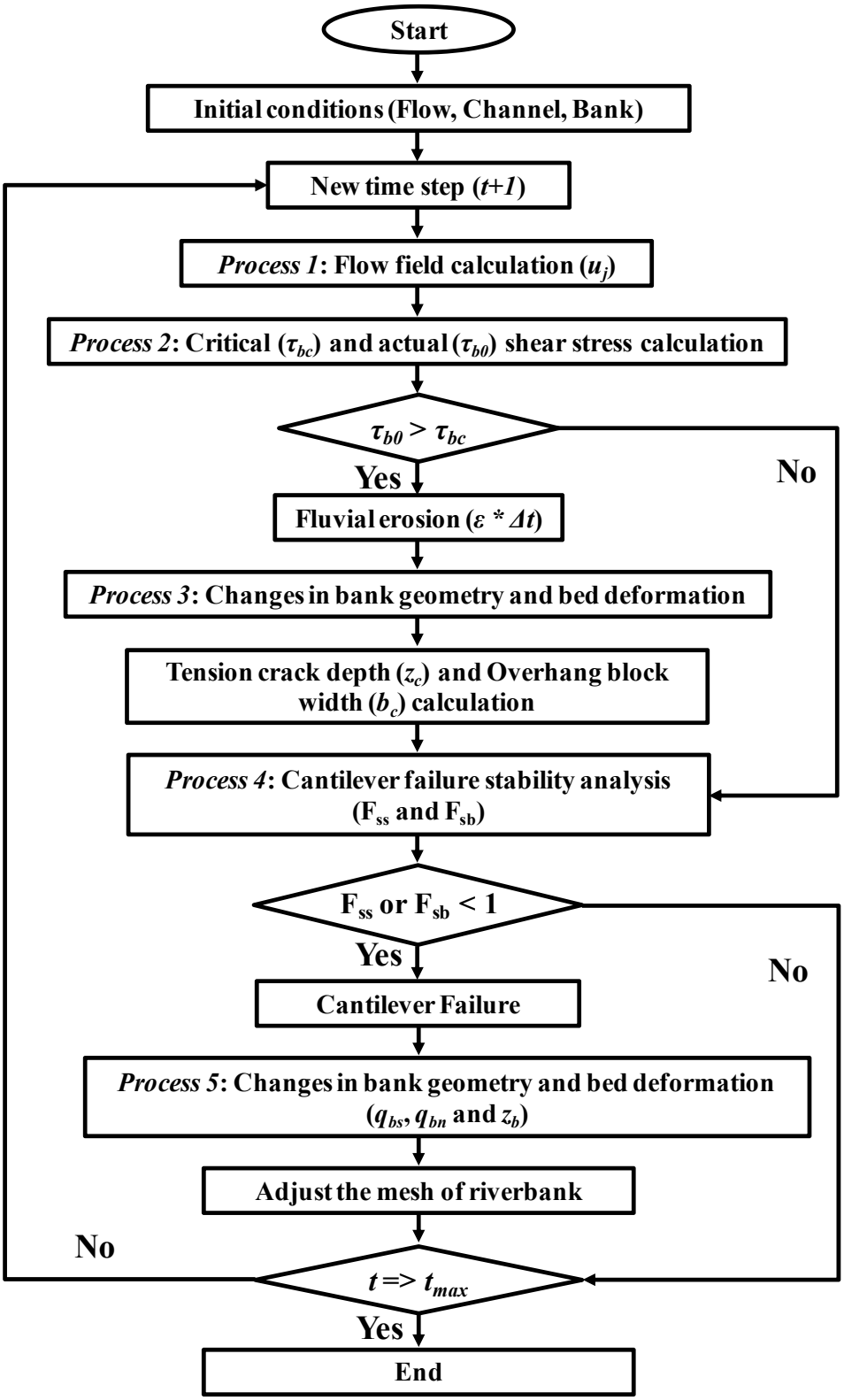


**Fig. 4.7** Logic diagram of the computational sequence of the coupled modeling.

The fluvial erosion rate is determined by using an excess shear stress relation around wetted perimeter, including bottom, lateral and top sides of the cohesive bank (Process 2 in **Fig. 4.7**) as shown below (Arulannandan et al., 1980; Partheniades, 1965).

$$\varepsilon = k_d \left( \tau_{b0} - \tau_{bc} \right)^a \tag{4.2}$$

where $\varepsilon$ is the fluvial erosion rate (m/s), $k_d$ is the erodibility coefficient ($m^3$/(N s)), $\tau_{b0}$ is the actual shear stress applied by the flow (Pa), $\tau_{bc}$ is the critical shear stress of the cohesive bank (Pa), and $a$ (dimensionless) is the exponent generally considered to be unity. In Eq. 4.2, the negative value of the excess shear stress determines the negative value of the fluvial erosion rate, which has no physical meaning. Therefore, the positive value of excess shear stress is only considered for fluvial erosion estimation.

The actual shear stress is determined by the function of the hydraulic radius, and channel slope in each calculated cell as shown in Eq. 4.3. Additionally, the near bed shear stress is assumed to be equal to the bank shear stress determined by the hydrodynamic model.

$$\tau_{b0} = \rho \, g \, R_j \, i \tag{4.3}$$

where $\rho$ is the density of water (1,000 kg/$m^3$).

The theoretical determination of the critical shear stress of bank material is complex, because it is dependent on several factors, including the plasticity index (Smerdon & Beasley, 1961; Yalin & Karahan, 1979), mean diameter (Smerdon & Beasley, 1961; Yalin & Karahan, 1979), internal friction angle (Yalin & Karahan, 1979), and the percentage of silt-clay content (Julian & Torres, 2006; Smerdon & Beasley, 1961).

The empirical equations of the critical shear stress as a function of mean diameter (Smerdon & Beasley, 1961), the modified Shields diagram (Yalin & Karahan, 1979), and the percentage of silt-clay content (Julian & Torres, 2006) are employed for this study, as expressed in Eqs. 4.4 to 4.6.

$$\tau_{bc} = 3.54 \times 10^{-28.1 d_{50}} \tag{4.4}$$

$$\tau_{bc} = \tau_{bc}^{*} \left( \gamma_s - \gamma_w \right) d_{50} \tag{4.5}$$

$$\tau_{bc} = 0.1 + 0.1779 \left( SC \right) + 0.0028 \left( SC^2 \right) - 2.34E^{-5} \left( SC^3 \right) \tag{4.6}$$

where SC is the percentage of silt-clay content, $\tau_{bc}^{*}$ is the critical Shield parameter ($0.3\mathrm{e}^{-d_*/3} + 0.06 \tan\phi \left( 1 - \mathrm{e}^{-d_*/20} \right)$), $\gamma_s$ is the unit weight of soil (N/$m^3$), $\gamma_w$ is the unit weight of water (N/ $m^3$), $d_*$ is the dimensionless particle diameter ($d_{50} \left[ \frac{(G-1)g}{\upsilon^2} \right]^{1/3}$), G is the specific gravity (2.65), and $\upsilon$ is the kinematic viscosity ($10^{-6}$ $m^2$/s).

For Eq. 4.4, Smerdon & Bealey (1961) conducted experimental work to determine the relationship between the critical shear stress and the basic soil properties (i.e., plasticity index, dispersion ratio,

mean diameter, and percentage of clay) on eleven samples of cohesive Missouri soils. Moreover, in Eq. 4.5, Yalin & Karahan (1979) modified the Shields diagram by using the dimensionless particle diagram. Additionally, Julian & Torres (2006) estimated the critical shear stress, based on the percentage of silt-clay content, by a third-order polynomial equation, as expressed in Eq. 4.6.

Although Eq. 4.2 appears simple, in practice, it is necessary to define the erodibility coefficient. This parameter is highly variable. Therefore, the in situ experiments for determining the critical shear stress, and erodibility coefficient are advantageous for different soils and environments (Hanson, 1990). In the previous study, several researchers conducted their experiments in natural rivers to develop the relationship between the critical shear stress and erodibility coefficient (Hanson & Simon, 2001; Karmaker & Dutta, 2011; Thoman & Niezgoda, 2008; Wynn, 2004).

For the relationship between the critical shear stress and erodibility coefficient, Hanson & Simon (2001) conducted their testes for a wide variety of soil types in riverbeds in the mid-western USA. The relationship is expressed in Eq. 4.7. In south-west Virginia, Wynn (2004) tested 142 samples in the vegetated riverbank and the erodibility coefficient relationship is shown in Eq. 4.8. Thoman & Niezgoda (2008) conducted 25 in situ jet testes in the ephemeral reach of the Power River Basin, Wyoming, USA. The relationship of this study is written in Eq. 4.9. Karmaker & Dutta (2011) carried out 58 in situ jet testes in the riverbank of the Brahmaputra River, India. The relationship is described in Eq. 4.10.

$$k_d = 0.2\tau_{bc}^{-0.5} \tag{4.7}$$

$$k_d = 3.1\tau_{bc}^{-0.37} \tag{4.8}$$

$$k_d = 1.11\tau_{bc}^{-0.37} \tag{4.9}$$

$$k_d = 3.16\tau_{bc}^{-0.185} \tag{4.10}$$

To characterize the fluvial erosion rate around the wetted perimeter of the bank, the fluvial erosion rate (Eq. 4.2) is evaluated in each timestep by the function of $k_d$, $\tau_{b0}$, and $\tau_{bc}$ to erode the bank in the vertical and lateral directions. For actual shear stress, this procedure is a simple method to evaluate the near-bank shear stress by neglecting the lateral shear stress because the secondary current in straight experimental flume and natural river show velocities of approximately 2% of the streamwise velocity (Blanckaret et al., 2010; Nezu et al., 1993). In addition, the shear stress distribution on the bank instead of a constant shear stress does not significantly change the simulation results of the migration by bank failure (Motta et al., 2014). As a result, this procedure is an idealization of the fluvial erosion rate estimation, and was used simply to simulate the coupled numerical model of the cantilever failure phenomena.

Mesh adaptation processes were developed for the computational process of fluvial erosion at the lower part of cohesive bank in the numerical modeling (Process 3 in **Fig. 4.7**). The assumption of mesh adaptation is that the bank profiles are deformed in accordance with the fluvial erosion simulated at the end of the discrete time step. Therefore, the undisturbed cell occupation rate ($\Omega_t$) was introduced in this study as expressed in Eq. 4.11.

$$\Omega_t = \frac{[V_{org} - \sum_{t=1}^{n} V_{erd}]}{V_{org}} \tag{4.11}$$

where $V_{org}$ is the initial volume of a grid cell of a cohesive bank ($m^3$), $V_{erd}$ is the simulated fluvial erosion volume in each time step ($m^3$), and $t$ is time (s).

For the first scheme, if the accumulated fluvial erosion volume is less than the initial grid cell volume of the bank, the boundary nodes are not shifted horizontally inward through fluvial erosion (**Fig. 4.8 (a)**). For the second scheme, if the accumulated fluvial erosion volume is equal to or larger than, the initial grid cell volume of the bank, new grid cells are assigned to update the bank profile nodes (**Fig. 4.8(b)**)

#### 4.2.3.2 Cantilever failure

The factor of safety for two types of cantilever failure are defined, namely shear-type failure (Thorne & Tovey, 1981) and beam-type failure (Micheli & Kirchner, 2002), because the tensile-type failure is rarely observed in natural rivers (Darby et al., 2007). Cantilever failure occurs if any part of the overhanging block has a factor of safety less than one (Process 4 in **Fig. 4.7**).

Shear-type failure is expected when the shear stress along the vertical plane from the overhanging block weight (*FD*) exceeds the resisting force of cohesive bank (*FR*), as shown in **Fig. 4.6**. The safety factor of shear failure ($F_{ss}$) is described as (Thorne & Tovey, 1981)

$$F_{ss} = \frac{C\,h_d}{\gamma_s A_b} \tag{4.12}$$

where $C$ is the cohesive force (Pa), $h_d$ is the effective length (m), $\gamma_s$ is the unit weight of soil ($N/m^3$), and $A_b$ is the cross-sectional area of overhanging block ($m^2$).

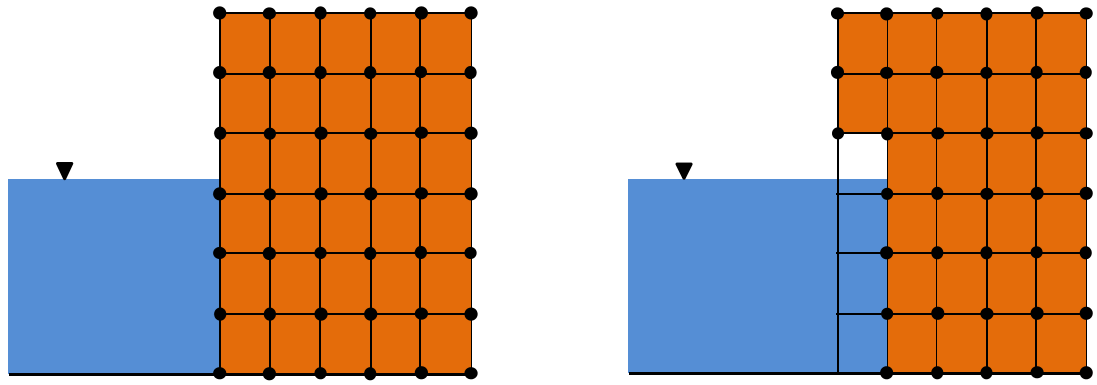

(a) Unmodified boundary nodes prior to fluvial erosion.

(b) New boundary conditions are assigned by the effect of fluvial erosion.

**Fig. 4.8** Illustration of the two schemes used to adopt the boundary nodes by the effect of fluvial erosion.

Beam-type failure is related to unstable overhanging blocks by rotation around a neutral axis (**Fig. 4.6**). This failure occurs when the rotational moment of the overhanging block overcomes the resistive moments of soil's strength in the tension and compression zones. The safety factor of a beam-type failure ($F_{sb}$) can be described as (Micheli & Kirchner, 2002)

$$F_{sb} = \frac{\sigma_c l_c^2 + \sigma_t l_t^2}{\gamma_s h_c b_c^2} \tag{4.13}$$

with $h_d = l_c + l_t$ and $\sigma_c/\sigma_t = l_t / l_c$, where $l_c$ and $l_t$ are the overhanging lengths under compressive and tensile strength (m), respectively; $\sigma_c$ and $\sigma_t$ are the compressive and tensile strength (kN/m$^2$). To link the cohesive and tensile strengths of cohesive material, the equation of Fang & Hirst (1973), and Fang & Daniels (2006) is employed for this study.

$$\sigma_t = \frac{C}{\xi} \tag{4.14}$$

with $\xi = 1/[0.34+0.01I_w]$, where $\xi$ is the ratio of tensile strength to cohesion and $I_w$ as the plasticity index. Finally, based on the Chen-Drucker modified Mohr-Coulomb criteria (Chen & Drucker, 1969), $\sigma_c$ is computed using:

$$\sigma_c = 2C \tan\left(45 + \frac{\phi}{2}\right) \tag{4.15}$$

where $\phi$ is the internal friction angle.

The tension crack depth ($z_c$) is assumed to be half of the overhanging block height ($h_c$) because the ratio of tension crack depth and overhanging block height ranges from 0.3 to 0.7, and does not typically change the factor of safety by more than 10% (Thorne & Abt, 1993).

In this study, the critical shear stress results were compared with three other empirical equations as expressed in Eqs. 4.4 to 4.6. Moreover, the erodibility coefficient was estimated by four empirical relationships as written in Eqs. 4.7 to 4.10. Following this, the appropriate critical shear stress equation was selected from the technical suggestions in the published researches and the physical meaning of values. Then, the erodibility coefficient by using existing empirical equations was compared with the observation values of the experimental studies (Patsinghasanee et al., 2015b, 2015c), and the U-Tapao River data (Semmad, 2010). As a result, the suitable critical shear stress and erodibility coefficient equations were selected to substitute in Eq. 4.2 for calculating fluvial erosion. Finally, the cantilever failure type was defined by the factor of safety determined by Eqs. 4.12 and 4.13 from the experimental studies, and the U-Tapao River data.

#### 4.2.3.3 Bedload transport and bed deformation

In terms of bedload transport and bed deformation, after the fluvial erosion and cantilever failure, the failure materials are dropped into the channel, and assumed to be non-cohesive materials and bedload (Process 5 in **Fig. 4.7**). The equations describing the bedload transport and bed deformation are as follows:

The sediment transport rate in the streamwise direction ($q_{bs}$) is calculated by Ashida & Michiue's formula as follows (Ashida & Michiue, 1972):

$$q_{bs} = 17\tau_*^{3/2}\left(1-\frac{\tau_{*c}}{\tau_*}\right)\left(1-\sqrt{\frac{\tau_{*c}}{\tau_*}}\right)\sqrt{Ggd_{50}^3} \tag{4.16}$$

where $\tau_*$ is the non-dimensional bed shear stress ($u_*^2/(G\,g\,d_{50})$); $u_*$ is the shear velocity ($\sqrt{g\,R_j\,i}$); and $\tau_{*c}$ is the non-dimensional critical bed shear stress, calculated using Iwagaki's formula (Iwagaki, 1956).

The sediment transport rate in the lateral direction ($q_{bn}$) is calculated by Hasegawa's formula for distributing the failure sediments in the lateral direction by using the function of the bed slope in the lateral direction in each calculated grid cell, and neglecting the effect of the secondary current (Hasegawa, 1984) as follows:

$$q_{bn} = -q_{bs}\sqrt{\frac{\tau_{*c}}{\mu_s\mu_k\tau_*}}\frac{\partial Z_b}{\partial y} \tag{4.17}$$

where $\mu_s$ is the static friction coefficient (1.0), and $\mu_k$ is the kinetic friction coefficient (0.45).

The bed deformation is calculated using the continuity equation of the sediment transport in the orthogonal coordinate, and is expressed as:

$$\frac{\partial Z_b}{\partial t} + \frac{1}{1-\lambda}\left(\frac{\partial q_{bn}}{\partial y}\right) = 0 \tag{4.18}$$

where $\lambda$ is the porosity of the material (0.4).

## 4.3 RESULTS AND DISCUSSION

In this section, results of the overhanging block properties, fluvial erosion, cantilever failure, and numerical modeling are presented. These results are determined by two types of overhanging blocks, consisting of the existing experimental results of a cantilever failure (Patsinghasanee et al., 2015b, 2015c), and the observed data of cross-sections of the U-Tapao River (Semmed, 2010).

### 4.3.1 Overhanging Block Properties

This section describes the properties of the reference overhanging blocks used in the analytical study, and numerical modeling. The overhanging blocks in the experimental channel (Table 4.3) and the U-Tapao River (Table 4.4) were selected to provide the overhanging block properties. The range of properties was selected as follows:

(1) The reference overhanging block height varied within the range of 0.09 to 0.15 m of the experimental flumes, and 1.37 to 5.26 m of the U-Tapao River.

(2) The reference overhanging block width varied within the range of 0.05 to 0.07 m, which are consistent with the range of experimental results (from 0.03 to 0.08 m) (Patsinghasanee et al., 2015b, 2015c), and within the range of 0.15 to 0.60 m of the U-Tapao River.

(3) The range of tension crack depth range was selected on the basic assumption that it is limited to half the overhanging block height.

(4) The range of water depth in the experimental flume varied from 0.03 to 0.06 m, as observed during the experiments. Additionally, the average water depth of the U-Tapao River in November 2009 was within the range of 4.72 to 5.74 m.

(5) The geotechnical parameters (i.e., cohesive force, percentage of silt-clay content, and internal friction angle) are described in the previous experimental study (Patsinghasanee et al., 2015b, 2015c), and the U-Tapao River study (Semmed, 2010).

(6) The tensile ($\sigma_t$) and compressive ($\sigma_c$) strengths were calculated by Eqs. 4.14 and 4.15. The $\sigma_t$ and $\sigma_c$ of the experimental flumes varied within the range of 2.25 to 2.50 kPa, and 21.8 to 28.33 kPa, respectively. For the U-Tapao River, the $\sigma_t$ and $\sigma_c$ were within the ranges of 2.64 to 9.65 kPa, and 16.59 to 51.14 kPa, respectively. Moreover, the ratios of the tensile to compressive strengths ($\sigma_t/\sigma_c$) were in the range of 0.09 to 0.19. These ratios were consistent with the previous study, in which this ratio was suggested to be approximately 0.1 (Ajaz, 1973).

### 4.3.2 Fluvial Erosion

The fluvial erosion of the cohesive bank was estimated using Eq. 4.2. Pragmatically, the estimations of the actual shear stress by Eq. 4.3, critical shear stress by Eqs. 4.4 to 4.6, and erodibility coefficient by Eqs. 4.7 to 4.10 are the significant parameters. Therefore, the estimated values of the significant parameters are described in this section.

For the actual shear stress, the values in the experimental banks varied between 0.68 and 1.23 Pa, whereas those in the U-Tapao River were within the range of 18.51 to 22.52 Pa. Additionally, the values of critical shear stress are 3.49 Pa for the experimental study and 3.53 Pa in the U-Tapao River, determined by the formula of Smerdon & Beasley (1961); 0.44 Pa for the experimental study and from 0.75 to 0.83 Pa in the U-Tapao River by Yalin & Karahan's formula (Yalin & Karahan, 1979); and from 0.38 to 0.57 Pa for the experimental study and 9.44 to 12.99 Pa in the U-Tapao River by Julian & Torres's formula (Julian & Torres, 2006). This is as expressed by the values of the actual and critical shear stresses of the experimental banks and the U-Tapao River in Tables 4.3 and 4.4, respectively.

The critical shear stress values measured using the in situ jet tests in the U-Tapao River vary from 10.58 to 10.64 Pa (Semmad, 2010). Comparisons of these values with those of the existing empirical equations indicate poor estimations using the modified Shields diagram (from 0.75 to 0.83 Pa), and mean diameter (3.53 Pa) methods. The reason for the former is that the modified Shields diagram was developed for non-cohesive materials. In addition, Smerdon & Beasley's formula (Smerdon & Beasley, 1961) yields a lower estimation than the observation values. On the other hand, the values estimated from the percentage of silt-clay content (from 9.44 to 12.99 Pa) are approximately equal to those measured in the in situ jet tests (from 10.58 to 10.64 Pa). For this reason, the percentage of silt-clay content provides a better estimation of the critical shear stress for cohesive materials than the other equations. Moreover, the actual shear stress calculated by Eq. 4.3 is suitable for this study

because the values in this equation are larger than those determined by the percentage of silt-clay content in the experimental flume and the U-Tapao River.

The erodibility coefficient ($k_d$) was estimated by four previous empirical equations. The estimated values of $k_d$ of the experimental banks and the U-Tapao River are shown in Tables 4.3 and 4.4, respectively. Comparisons of the results of the previous relationship as expressed by Eqs. 4.7 to 4.10 and the experimental studies show poor agreement. This is due to the fact that the experiments for the previous empirical equations were carried out in natural rivers, whereas those of the present study were conducted in the experimental channel. In the U-Tapao River, the values of $k_d$ measured by in situ jet test are in the range of 0.07 to 21.33 $cm^3/(N\ s)$ (Semmad, 2010). However, the values of $k_d$ determined by the previous empirical equations are within the range of 0.06 to 2.08 $cm^3/(N\ s)$. This may be due to the fact that the experiments in the previous studies were carried out in riverbed zones (Hanson & Simon, 2001), vegetated riverbanks (Kamaker & Dutta, 2011; Wynn, 2004), and ephemeral riverbanks (Thoman & Niezgoda, 2008), whereas the studies in the U-Tapao River were carried out in the riverbank zone with sparse vegetation cover (Semmad, 2010).

Therefore, the relationship between the critical shear stress ($\tau_{bc}$) and erodibility coefficient ($k_d$) indicates that it does not follow the previous relationship. As a result, the analysis of $k_d$ and $\tau_{bc}$ determined that these parameters vary significantly from one site to another. Thus, for the fluvial erosion rate, the relationship of the $k_d$ and $\tau_{bc}$ is required to be measured locally.

### 4.3.3 Cantilever Failure

To determine the cantilever failure, the factor of safety equations for the shear-type and beam-type failures in Eqs. 4.12 and 4.13 were calculated using the properties of the reference overhanging blocks, as expressed in Tables 4.3 and 4.4.

For the experimental studies, the factor of safety of the beam-type failure is less than one. It is clear that the beam-type failure is the dominant failure mechanism in the experimental studies. On the other hand, for the U-Tapao River, the factor of safety of the shear-type failure in the four cross-sections is less than one. This means that the shear-type failure is the dominant failure mechanism in the U-Tapao River. The values of the factor of safety are expressed in Tables 4.3 and 4.4.

Moreover, the relationship between overhanging block height ($h_c$) and overhanging block width ($b_c$) of the experimental study and U-Tapao River at the critical stage of the shear-type failure and beam-type failure ($F_{ss}$ and $F_{sb}$ = 1) are illustrated in **Fig. 4.9**. For example, in Case 5 of the experimental study, the analytical results show that fluvial erosion at the submerged bank zone has the effect on the cantilever failure instability because such erosion increase the overhanging block width but decrease its stability (**Fig. 4.9(a)**). Moreover, Zone ABC in **Fig. 4.9(a)** represents a stable zone but Zone ACDE means an unstable stage. If the overhanging block width reaches to Line AC (solid line), it means that the cantilever failure will reach to the beam-type failure before shear-type failure (dash line). It has been confirmed that the beam-type failure is the dominant failure mechanism of this case. In the cross-section UT.1, Point D is the transition point of the cantilever failure type from beam-type failure (solid line) to shear-type failure (dash line). Zone ABCD in **Fig. 4.9(b)** represents a stable stage of the overhanging block. If the overhanging block height of this section is not higher than 1.2 m, the beam-type failure will be the dominant failure mechanism. However, the overhanging block height during flood period in November 2009 of cross-section UT.1 was equal to 5.26 m. Therefore, the analytical results have been reported that the dominant failure mechanism of cross-section UT.1 is shear-type failure.

Table 4.3 Properties, actual shear stress, critical shear stress, erodibility coefficient, and factor of safety of the reference overhanging blocks of the experimental cohesive banks.

| Variable | Symbol | Case 1 | Case 2 | Case 3 | Case 4 | Case 5 | Case 6 |
|---|---|---|---|---|---|---|---|
| 1) Overhanging block properties: | | | | | | | |
| Overhanging block height (m) | $h_c$ | 0.15 | 0.10 | 0.12 | 0.10 | 0.09 | 0.09 |
| Tension crack depth (m) | $z_c$ | 0.08 | 0.05 | 0.06 | 0.05 | 0.05 | 0.04 |
| Overhanging block width (m) | $b_c$ | 0.07 | 0.06 | 0.06 | 0.05 | 0.05 | 0.06 |
| Flow depth (m) | $D$ | 0.05 | 0.05 | 0.03 | 0.05 | 0.06 | 0.06 |
| Compressive length (m) | $l_c$ | 0.007 | 0.005 | 0.005 | 0.004 | 0.004 | 0.003 |
| Tensile length (m) | $l_t$ | 0.073 | 0.045 | 0.055 | 0.046 | 0.046 | 0.037 |
| Cohesive force (kPa) | $C$ | 5.76 | 5.76 | 5.76 | 6.41 | 6.41 | 5.37 |
| Silt-clay content (%) | SC | 30.0 | 30.0 | 30.0 | 20.0 | 20.0 | 30.0 |
| Internal friction angle ($^o$) | $\phi$ | 34.3 | 34.3 | 34.3 | 41.3 | 41.3 | 39.8 |
| Compressive strength (kPa) | $\sigma_c$ | 21.80 | 21.80 | 21.80 | 28.33 | 28.33 | 25.25 |
| Tensile strength (kPa) | $\sigma_t$ | 2.25 | 2.25 | 2.25 | 2.50 | 2.50 | 2.38 |
| Ration of the tensile by compressive strength | $\sigma_t/\sigma_c$ | 0.10 | 0.10 | 0.10 | 0.09 | 0.09 | 0.09 |
| 2) Actual shear stress and critical shear stress (Pa): | | | | | | | |
| Actual shear stress | $\tau_{b0}$ | 0.93 | 0.93 | 0.68 | 0.93 | 1.16 | 1.23 |
| Critical shear stress by Smerdon & Beasley's Eq. | $\tau_{bc}$ | 3.49 | 3.49 | 3.49 | 3.49 | 3.49 | 3.49 |
| Critical shear stress by Yalin & Karahan's Eq. | $\tau_{bc}$ | 0.44 | 0.44 | 0.44 | 0.44 | 0.44 | 0.44 |
| Critical shear stress by Julian & Torres's Eq. | $\tau_{bc}$ | 0.57 | 0.57 | 0.57 | 0.38 | 0.38 | 0.57 |
| 3) Erodibility coefficient ($cm^3/(N\ s)$): | | | | | | | |
| Observation values | $k_d$ | 217.97 | 871.90 | 1,285.87 | 109.06 | 172.09 | 115.14 |
| Erodibility coefficient by Hason & Simon's Eq. | $k_d$ | 0.26 | 0.26 | 0.26 | 0.32 | 0.32 | 0.26 |
| Erodibility coefficient by Wynn's Eq. | $k_d$ | 3.82 | 3.82 | 3.82 | 4.42 | 4.42 | 3.82 |
| Erodibility coefficient by Thoman & Niez's Eq. | $k_d$ | 1.37 | 1.37 | 1.37 | 1.58 | 1.58 | 1.37 |
| Erodibility coefficient by Kamaker & Dutta's Eq. | $k_d$ | 3.51 | 3.51 | 3.51 | 3.77 | 3.77 | 3.51 |
| 4) Factor of safty: | | | | | | | |
| Shear-type failure | $F_{ss}$ | 1.57 | 1.98 | 1.80 | 2.45 | 2.42 | 2.09 |
| Beam-type failure | $F_{sb}$ | 0.60 | 0.64 | 0.60 | 0.90 | 0.77 | 0.58 |

Table4.4 Properties, actual shear stress, critical shear stress, erodibility coefficient, and factor of safety of the reference overhanging blocks of the U-Tapao River.

| Variable | Symbol | UT.1 | UT.2 | UT.3 | UT.4 |
|---|---|---|---|---|---|
| 1) Overhanging block properties: | | | | | |
| Overhanging block height (m) | $h_c$ | 5.26 | 4.81 | 1.37 | 4.71 |
| Tension crack depth (m) | $z_c$ | 2.63 | 2.41 | 0.68 | 2.36 |
| Overhanging block width (m) | $b_c$ | 0.45 | 0.60 | 0.15 | 0.35 |
| Flow depth (m) | $D$ | 5.74 | 4.72 | 4.76 | 4.82 |
| Compressive length (m) | $l_c$ | 0.323 | 0.385 | 0.094 | 0.343 |
| Tensile length (m) | $l_t$ | 2.307 | 2.025 | 0.586 | 2.017 |
| Cohesive force (kPa) | $C$ | 9.25 | 17.05 | 5.53 | 4.89 |
| Silt-clay content (%) | SC | 55.8 | 53.0 | 82.5 | 50.1 |
| Internal friction angle ($^o$) | $\phi$ | 28.42 | 22.61 | 22.58 | 28.96 |
| Compressive strength (kPa) | $\sigma_c$ | 31.05 | 51.14 | 16.59 | 16.59 |
| Tensile strength (kPa) | $\sigma_t$ | 4.26 | 9.65 | 2.64 | 2.81 |
| Ration of the tensile by compressive strength | $\sigma_t/\sigma_c$ | 0.14 | 0.19 | 0.16 | 0.17 |
| 2) Actual shear stress and critical shear stress (Pa): | | | | | |
| Actual shear stress | $\tau_{b0}$ | 22.52 | 18.51 | 18.66 | 18.90 |
| Critical shear stress by Smerdon & Beasley's Eq. | $\tau_{bc}$ | 3.53 | 3.53 | 3.53 | 3.53 |
| Critical shear stress by Yalin & Karahan's Eq. | $\tau_{bc}$ | 0.75 | 0.82 | 0.83 | 0.79 |
| Critical shear stress by Julian & Torres's Eq. | $\tau_{bc}$ | 11.00 | 10.22 | 12.99 | 9.44 |
| 3) Erodibility coefficient ($cm^3/(N\ s)$): | | | | | |
| Observation values | $k_d$ | 6.37 | 6.37 | 0.07 | 21.33 |
| Erodibility coefficient by Hason & Simon's Eq. | $k_d$ | 0.06 | 0.06 | 0.06 | 0.06 |
| Erodibility coefficient by Wynn's Eq. | $k_d$ | 1.27 | 1.31 | 1.20 | 1.35 |
| Erodibility coefficient by Thoman & Niez's Eq. | $k_d$ | 0.45 | 0.47 | 0.43 | 0.48 |
| Erodibility coefficient by Kamaker & Dutta's Eq. | $k_d$ | 2.03 | 2.06 | 1.97 | 2.08 |
| 4) Factor of safty: | | | | | |
| Shear-type failure | $F_{ss}$ | 0.54 | 0.75 | 0.93 | 0.35 |
| Beam-type failure | $F_{sb}$ | 1.27 | 1.43 | 1.75 | 1.15 |

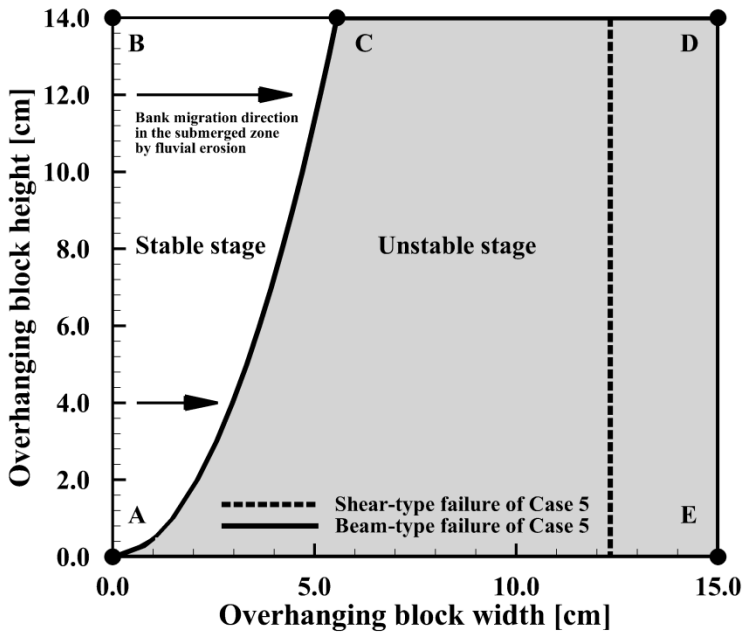


(a) Experimental study (Case 5).

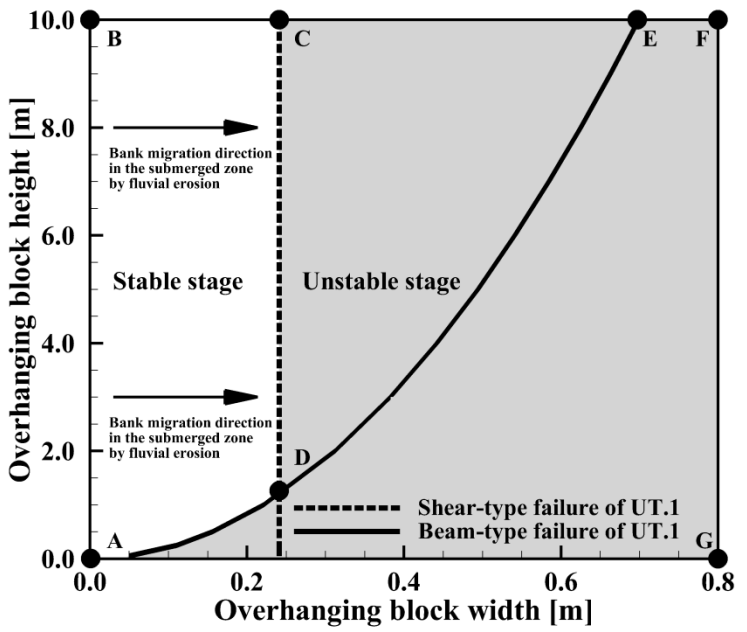


(b) The U-Tapao River (UT.1).

**Fig. 4.9** Relationship between overhanging block height and overhanging block width at the critical failure stage.

### 4.3.4 Numerical Results

To assess the accuracy and reliability of the numerical results, they were only validated from the experimental results in terms of the temporal variations of the spatially averaged bank width, because the temporal survey data of the cantilever failures of the U-Tapao River were not available in the previous research (Semmed, 2010). However, the 2D cross-sectional model of the U-Tapao River were developed for obtaining the physical simplification in the overhanging block geometries (width and height), and dominant cantilever failure type in each cross-section.

In this study, the fluvial erosion, cantilever failure, and bedload sedimentation were represented on a Cartesian grid cell. For the experimental flume simulation, 20 lateral grid cells (1D coarse grid cell) were employed for simulating flow velocity in each calculated cell. Moreover, 200 lateral grid cells were used to compute bedload transportation, bed deformation, and fluvial erosion shifted the bank nodes horizontally inward though cohesive bank. Additionally, 80 vertical grid cells were employed for reproducing the cantilever failure. The coupling model was simulated for 1 h period employing a time step of 0.05 second.

**Fig. 4.10** shows cross-sectional views at two time stages simulated by the numerical modeling. **Fig. 4.10(a)** shows the fluvial erosion at the submerged zone, when the cohesive bank is still stable. This process occurs by fluvial entrainment of material from the bank-toe and leads to the undermining of the cohesive bank that reproduce the overhanging block. **Fig. 4.10(b)** shows the beam-type failure of a cohesive bank, which is a common mechanism of cantilever failure (Abam, 1997; Micheli & Krichner, 2002; Patsinghasanee et al., 2015b, 2015c; Thorne & Tovey, 1981). Following the dropped process of numerical modeling, the failure material (Zone III in **Fig. 4.10(b)**) were assumed to be non-cohesive materials that come to rest at the intermediate dropped point. Furthermore, the silt-clay content in failure material was assumed to immediately transport out of numerical domain.

Moreover, the validation results of the temporal variations of the spatially averaged bank width by the current numerical modeling, and the experimental results are shown in **Fig. 11**. The current numerical results show a better agreement with the experimental results than those the previous numerical results (Patsinghasanee et al., 2015b, 2015c). This is due to the fact that the current numerical modeling used the erodibility coefficient from the experimental values. In contrast, the previous numerical results illustrate quite poor validation agreement in terms of the temporal variations of the spatially averaged bank width because the previous numerical modeling employed analytical equations for calculating erodibility coefficient. Additionally, the current numerical modeling can reproduce the first cantilever failure with high precision in terms of the times and the overhanging block width. For the current numerical modeling, significant errors occurred after the cantilever failure because the failure material dropped into the channel and protected against further fluvial erosion at the bank-toe. Therefore, the slump block effect must be considered in the new numerical modeling.

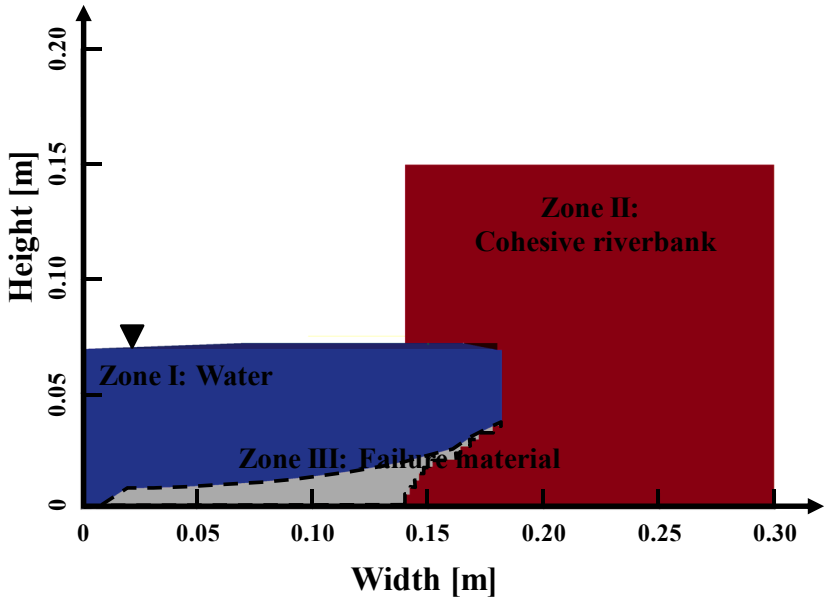


(a) Fluvial erosion stage.

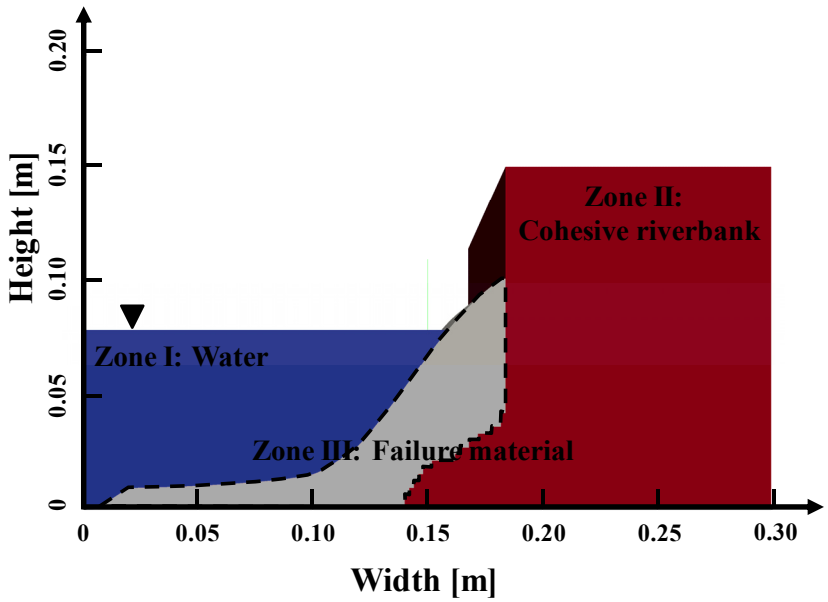


(b) Beam-type failure stage.

**Fig. 4.10** Cross-sectional views of fluvial erosion and beam-type failure mechanism at two time stages for Case 5. (Zone I is water, Zone II is the cohesive bank, and Zone III is the failure material.)

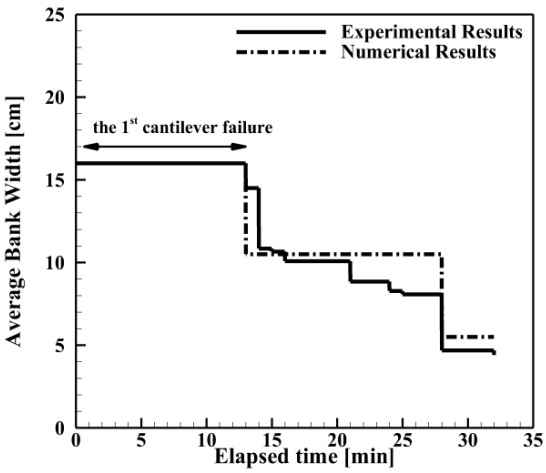


(a) Case 1.

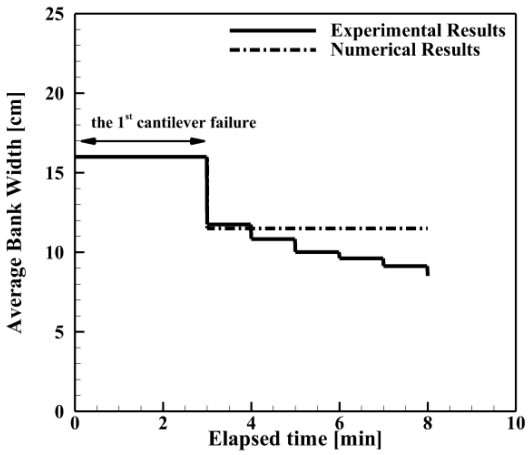


(b) Case 2.

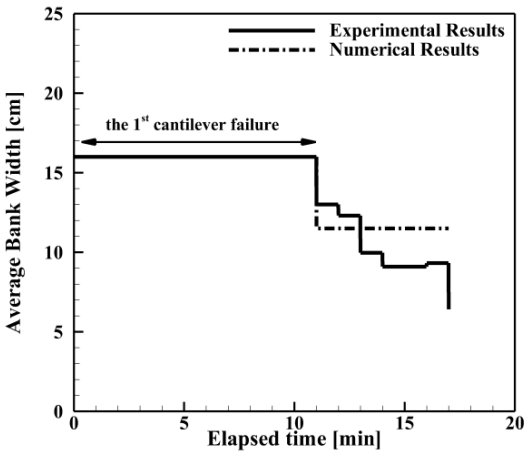


(c) Case 3.

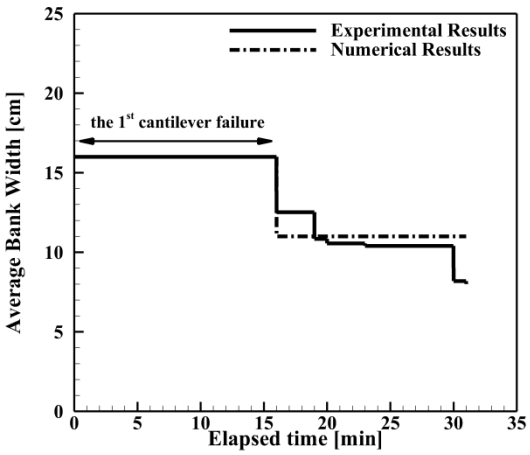


(d) Case 4.

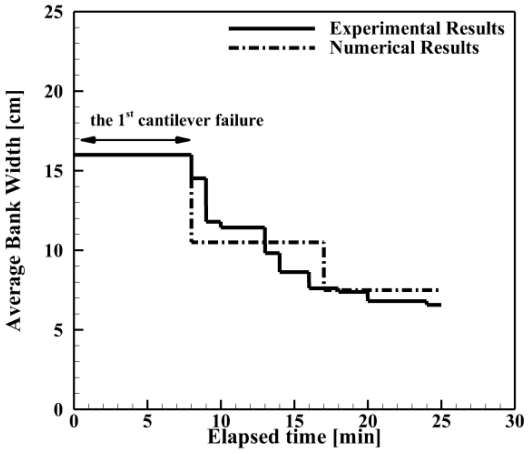


(e) Case 5.

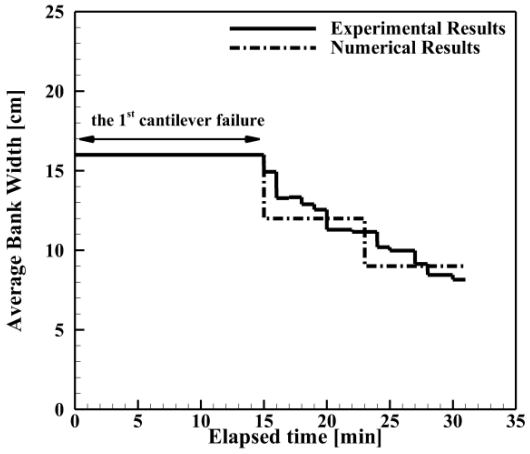


(f) Case 6.

**Fig. 4.11.** Validation results of the temporal variations of spatially averaged bank width.

For the U-Tapao River modeling, the initial cross-section have assumed a vertical riverbank because the survey cross-sectional data are presented that the U-Tapao riverbanks are almost become vertical as shown in the example data of section UT.1 in **Fig. 4.3**. The numerical riverbank geometries are 10 m in a channel width, 15 m in a cohesive riverbank width, and a variable bank height of 6.13 to 11.0 m. Moreover, 25 and 625 lateral grid cells were used for simulating flow velocity, fluvial erosion, bedload transportation, and bed deformation in 1D coarse grid cell and 1D finer grid cell, respectively. Furthermore, 200 vertical grid cells were employed for replicating cantilever failure on the overhanging block of the U-Tapao River. From an analysis of the discharge record in November 2009 at the Royal Irrigation Department station X.90 (Ban Bang Sala, Hatyai, Songkhla) near UT.1, a model discharge was derived of 224.3 $m^3/s$, which is the average value of flood period during field survey data on November 2009.

The simulation results of the four cross-sections in the U-Tapao River are shown that the shear-type failure is the dominated failure mechanism, which is similar to the analytical results in Section 4.3.3. Additionally, the overhanging block geometries in the numerical results are within the range of 0.16 to 0.48 m in width, and 2.44 to 7.26 m in height, while those in the survey data are within the range of 0.15 to 0.60 m in width, and 1.37 to 5.26 m in height. Therefore, this study can conclude that the simulated results are consistent with that survey data in terms of overhanging block geometries.

However, the present numerical model is a cross-sectional 2D model. Thus, it is limited to simulate non-uniform cantilever failure, complex flow characteristic near and inside the cohesive bank, longitudinal gradient of sediment transport, pore water pressure, and slump block effect. This means that the current model cannot replicate the non-uniform cantilever failure mechanism, the slump block effect, and longitudinal gradient of sediment transport observed in the laboratory experiments.

## 4.4 SUMMARY

This study has elucidated the mechanisms of cantilever failure by means of an analytical study, and numerical modeling of the experimental results and data from the U-Tapao River, Thailand.

For fluvial erosion, the actual shear stresses of the experimental works range from 0.68 to 1.23 Pa, whereas those of the U-Tapao River are within the range of 18.51 to 22.52 Pa. Moreover, the critical shear stresses estimated by the percentage of silt-clay content of the experimental banks are within the range of 0.38 to 0.57 Pa, whereas those of the U-Tapao River range from 9.44 to 12.99 Pa. Additionally, a comparison of the results of the erodibility coefficient between the four previous relationships and the experimental results show a poor agreement. This is owing to the fact that the previous equations were tuned under natural river conditions, whereas the current study was conducted in the experimental channel. Moreover, the erodibility coefficient estimated by the previous equations and the measurements of the U-Tapao River yield significantly different values because of the different riverbank material properties, covered vegetation, measured region of channel, and consolidation load acting on the upper surface of the cohesive riverbank between the previous study areas and the U-Tapao River. Therefore, the relationship between the erodibility coefficient and the critical shear stress of this research indicates that they do not follow the previous relationships. As a result, the analysis of the erodibility coefficient and the critical shear stress determined that these parameters significantly vary from one site to another. Thus, the relationship of the erodibility coefficient and the critical shear stress are required to be measured locally. Furthermore, the results show that the dominant cantilever failure mechanisms of the experiment, and the U-Tapao River are the beam-type and shear-type failure, respectively. From the above

explanations, the results show that this method is able to analyze the cantilever failure of the cohesive riverbank in the experimental flumes and the natural river.

Finally, for the numerical modeling, the comparison results of the temporal variations of the spatially averaged bank width between the current numerical and experimental results show a high degree of confidence. Significant errors occurred after the cantilever failure because the failure material was dropped into the channel and protected against further fluvial erosion at the bank-toe. Therefore, the slump block effect must be considered in the new numerical modeling. Moreover, the numerical results of the U-Tapao River can reproduce the accurate failure mechanism, which is shear-type failure, and overhanging block geometries in terms of width and height.

# Chapter 5

# EXPERIMENTAL INVESTIGATION ON CANTILEVER FAILURES FOR COHESIVE RIVERBANKS

## 5.1 INTRODUCTION

Riverbank failure results in extensive sediment production in an alluvial channel, and can cause severe environmental and economic problems such as loss of fertilization in agriculture areas and destruction of infrastructure (Taghavi et al., 2010). However, because cantilever failure involves rapid channel widening and delivers a large volume of sediment into the channel, such a failure is a serious issue in river engineering (Nardi et al., 2012). Elucidating the underlying mechanism of cantilever failure is therefore important for a full understanding of fluvial erosion and riverbank failure with the effect of slump blocks along a channel.

Only a few studies have applied stability analysis based on the safety factor of the portion with cantilever failure, from which three types of possible cantilever failure mechanisms—shear-type, beam-type and tensile-type failures—have been defined (Abam, 1997; Thorne & Tovey, 1981). However, the tensile-type failure was rarely observed along the natural rivers (Darby et al., 2007; Thorne & Tovey, 1981).

For experimental studies, several small-scale experiments were carried out to examine fluvial erosion and cantilever failure phenomena (Fukuoka et al., 1999) and to measure flow characteristics (Bahar & Fukuoka, 2002). Moreover, a couple of large-scale experiments were conducted to estimate the failure plane angle and tension crack (Taghavi et al., 2010), and to investigate the dominant cantilever failure mechanism by using sandy gravel banks (Nardi et al., 2012) and cohesive banks (Samadi et al., 2013). However, all of the large-scale experiments focused solely on processes related to cantilever failure and the interaction between stagnant water and cohesive materials; fluvial erosion was not taken into account. Recently, the interaction between fluvial erosion and cantilever failure was investigated in a small-scale experimental flume (Patsinghasanee et al., 2015b, 2015c).

After a cantilever failure, the overhanging blocks crumble down in a shape like slump blocks and cover the bank-toe. It is thought the fluvial erosion rate decreases because of the failure of slump blocks (Dulal et al., 2010). Moreover, the simplified process of slump blocks was expressed in small-scale experiments (Dulal & Shimizu, 2010) and natural rivers (Parker et al., 2011) for the first time.

To address the gaps in the experimental study of the processes for a cantilever failure with slump block considerations, large-scale experiments were conducted on a straight rectangular flume to understand the complex mechanism of cantilever failure using high-resolution video cameras to measure the temporal bank width and acceleration sensors to clarify the failure mechanism inside the cohesive riverbank. Additionally, the slump block mechanisms during the progress of cantilever failure and its decomposition phenomena are discussed in laboratory experiments.

## 5.2 METHODOLOGY

To deal with the limitations in the underlying mechanisms of a cantilever failure with slump block effect and because of a lack of previous experimental literatures, large-scale experimental works related to fluvial erosion and cantilever failure with slump block effect were conducted in a fix bed rectangular straight flume with a Plexiglas wall to allow for real-time observation and recording. The water and sediments were recirculated using a constant head tank of water placed at the upstream end of flume. Moreover, to reproduce a steady uniform flow, the water discharge remained constant at 6.45 l/s using a rectangular weir to regulate a constant discharge during the experiments. In addition, the initial water level was set to zero and a free-flowing condition was controlled at the downstream end.

Generally, the main limitations of the previous experiments were the scale and sidewall correction effects. For this chapter, the geometrical and material scaling, and the sidewall correction effect were considered to form the cohesive riverbanks and construct the experimental flume. Therefore, a governing equation was employed with regard to the shear-type failure of an overhanging block as follows (Muir, 2004; Samadi et al., 2013):

$$F_{ss} = f\left(C/\gamma_s b_c\,,\, h_c/b_c\right) \tag{5.1}$$

where $F_{ss}$ is the factor of safety of shear-type failure, $C$ is the cohesive force (Pa), $\gamma_s$ is the unit weight of soil (N/m$^3$), $b_c$ is the overhanging block width (m), and $h_c$ is the overhanging block height (m).

Based on Eq. 5.1, if an overhanging block is formed in the laboratory flume, the values of the two dimensionless parameters must be similar in both the prototype and experimental model. Moreover, the overhanging block height affects both the resistant and driving forces acting on unit width of an overhanging failure block (Muir, 2004; Samadi et al., 2013). Therefore, this parameter can be neglected in the stability analysis as shown in Eq. 5.2. Thus, it is only necessary to evaluate the remaining three parameters (i.e. cohesive force, unit weight of soil, and factor of safety) to model a cantilever failure in the laboratory:

$$F_{ss} = C/\gamma_s b_c \tag{5.2}$$

Based on the above explanation, $F_{ss}$ was assumed to be one, which is the critical point of an overhanging block stability. Moreover, $\gamma_s$ and $C$ of the materials were determined using a water pycnometer and a direct shear test. Further information about a direct shear test is given by Patsinghasanee et al., (2015b, 2015c) (see Chapter 3). After that, the overhanging block width can be estimated by substituting $F_{ss}$, $\gamma_s$ and $C$ into Eq. 5.2. As a result, the critical overhanging block width is equal to 0.23 m. For experimental design, the flume dimensions were 0.8 m in width, 8.0 m in length, and 0.4 m in height and the channel slope was set to 0.001, as shown in **Fig. 5.1**. In the upstream region of the flume (0.0-3.0 m from the upstream), a wooden board was installed to avoid fluvial erosion (I to II). At the middle reach of the flume (3.0-5.0 m from the upstream), a cohesive riverbank was set (II to III). The cohesive riverbank was 0.5 m wide, which is about two times larger than the estimated value (0.23 m), 2.0 m long and 0.2 m high. Downstream of the cohesive riverbank, a second wooden board was installed to protect the cohesive riverbank from fluvial erosion (III to IV).

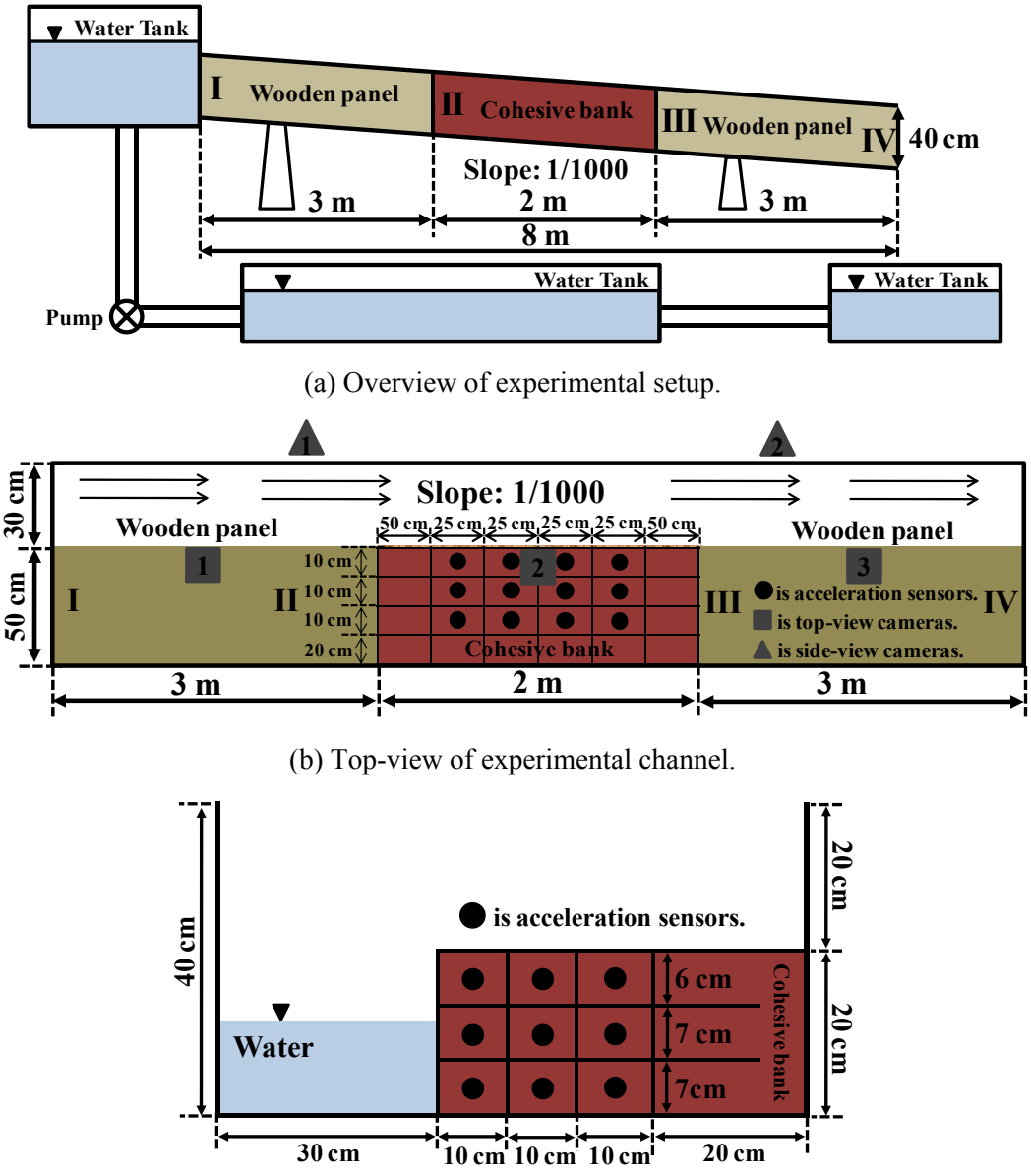


**Fig. 5.1** Dimensions of the large-scale experimental channel.

For sediment preparations, sediment composed of sand and silt with a mean diameter ($d_{50}$) of around 0.23 mm and 28.4 µm, respectively, was used. The sediments were well mixed and massaged by slowly adding water. The sediment mixtures were initially wetted with water to achieve a water content between 32.2% and 39.6% for the percentage of silt-clay content (SC) of 20% and 30% under the similar conditions with the previous study (Patsinghasanee et al., 2015b, 2015c). For this experiment, two parameters (i.e., the silt-clay content and water content) were varied in this study, because the cohesive force of cohesive riverbank is mainly related to the silt-clay content (Couper, 2003; Dulal & Shimizu, 2010; Grabowski et al., 2011; Julian & Torres, 2006) and water content (Couper, 2003; Grabowski et al., 2011; Rinaldi & Nardi, 2013; Thorne & Tovey, 1981). However, the sediment mixtures were prepared by varying the silt-clay content because, for the sediments used in this study, it was difficult to control the water content with the different silt-clay content as following the suggestion of previous study (Patsinghasanee et al., 2015b, 2015c).

To allow for a sufficient consolidation process, the cohesive riverbanks were compacted by applying a static load of 0·04 kg/cm$^2$ for 72 h (Nardi et al., 2012; Patsinghasanee et al., 2015b, 2015c). Dynamic compaction was not used either to protect a Plexiglas wall from damage and to reproduce the natural cohesive riverbank conditions that normally occur through static compaction. During the cohesive riverbank construction, a wooden panel was positioned to form a vertical cohesive riverbank. The panel was removed before the experiments started. The experimental conditions required to stop the test were (1) when cantilever failures proceeded throughout all of the cohesive riverbanks or (2) when an equilibrium stage was reached (without a failure for a 3-h period). Composite layers were not considered because of uncertainties regarding the cantilever failure phenomenon with the slump block effect and lack of previous studies. For material properties, the values of the cohesive force and internal friction angle were used from the previous study (Patsinghasanee et al., 2015b, 2015c) because the cohesive materials were mixed under the similar conditions with the previous work. The riverbank geometries, discharges, and cohesive material properties used during the experiments are summarized in Table 5.1.

Table 5.1 Summary of the large-scale experimental conditions.

| Variable | Case 1 | Case 2 |
|---|---|---|
| Discharge (l/s) | 6.45 | 6.45 |
| Bank height (cm) | 20 | 20 |
| Bank width (cm) | 50 | 50 |
| Silt-clay content (%) | 30 | 20 |
| Water content (%) | 39.6 | 32.2 |
| Cohesive force (Pa) | 5.76 | 6.41 |
| Internal friction angle (°) | 34.3 | 41.3 |
| Bank critical shear stress (Pa) | 0.57 | 0.38 |
| Erodibility coefficient (m$^3$/(N s)) | 105.6 | 42.8 |
| Reynolds number | 21,500 | 21,500 |
| Froude number | 0.56 | 0.56 |

The advantage of the experiment was the possibility to observe and record the cantilever failure mechanism with the slump block from the top and side views, and inside of the cohesive riverbanks of the experimental flume during fluvial erosion, tension crack, cantilever failure and slump block. All failure mechanisms were recorded using 5 high-resolution video cameras and 36 acceleration sensors, as shown in **Figs. 5.1(b)** and **5.1(c).** The video cameras were fixed perpendicular on position for the top-view (3 cameras) and side-side (2 cameras) of the flume to record the temporal bank width and water depth. Additionally, the metric scales were positioned in both the horizontal and vertical directions of the experimental flume. The video frames were subsequently converted into gray-scale

metrics, and the temporal bank width and water depth were determined through a digitization process with a precision of around 1 mm. Moreover, the acceleration sensors (Onset computer corporation (USA); UA-004-64) were installed inside the cohesive riverbanks that were similar with the previous experimental scale (Shimada et al., 2009) and the large-scale experiment of a riverine levee breach (Kakinuma & Shimizu, 2014). Sensor specifications were expressed in Table 5.2. Acceleration signals in the *x-y-z* directions would produced due to the failure and outflow of the installation positions. These sensors are of the self-recording type and they must be collected after the completion of the experiment for data acquisition.

Table 5.2 Acceleration sensor specifications.

| Variable | UA-004-64 |
|---|---|
| Measurement range | ±3 *g* |
| Accuracy | ±0.075 *g* |
| Resolution | 0.025 *g* |
| Time accuracy | ±1 min/month |
| Dimension | 58 × 33× 23 mm |
| Weight | 18 grams |

## 5.3 RESULTS

A summary of the cantilever failure and slump block effect during each experiment is provided with reference to the images of the temporal bank width and with the acceleration signals to clarify the failure mechanisms inside the cohesive riverbanks.

A series of small-scale experiments were carried out to test the responses, in terms of fluvial erosion, tension crack and cantilever failure, of the different silt-clay contents and water contents. For instance, the possible silt-clay content and water content were tested that appeared to be appropriate to reproduce the cantilever failure mechanisms. A summary of the initial tests was reported in the Chapter 3 (Patsinghasanee et al., 2015b, 2015c). The results of these experiments were used to compare with and analyze the failure mechanisms in the large-scale experiments.

For large-scale experiments, an important task is to clarify the cantilever failure processes in chronological order. Therefore, the acceleration sensors were installed inside the cohesive riverbanks. These sensors recorded the chronological failure mechanisms and identified the fluvial erosion or cantilever failure at points where the values varied greatly. As results of the acceleration values, **Fig. 5.2** shows the acceleration values in the *x-y-z* directions recorded by the sensors. For data interpretation, if the acceleration values suddenly change in the *y*-direction or *z*-direction, they mean that the beam-type or shear-type failure occurs in a cohesive riverbank, respectively. Moreover, the changed acceleration values in the *x*-direction mean that the fluvial force erodes a cohesive riverbank at the submerged zone. A summary of the failure processes determined in the experimental studies is as follows, with a reference photo reported in **Figs. 5.3** and **5.4** and the temporal bank geometry

measured using the acceleration sensors as shown in **Fig. 5.5**. For **Fig. 5.5**, a representative block of a sensor (10 cm in width, 25 cm in length and 6 or 7 cm in height) was removed from an initial cohesive riverbank, if the acceleration signals varied greatly.

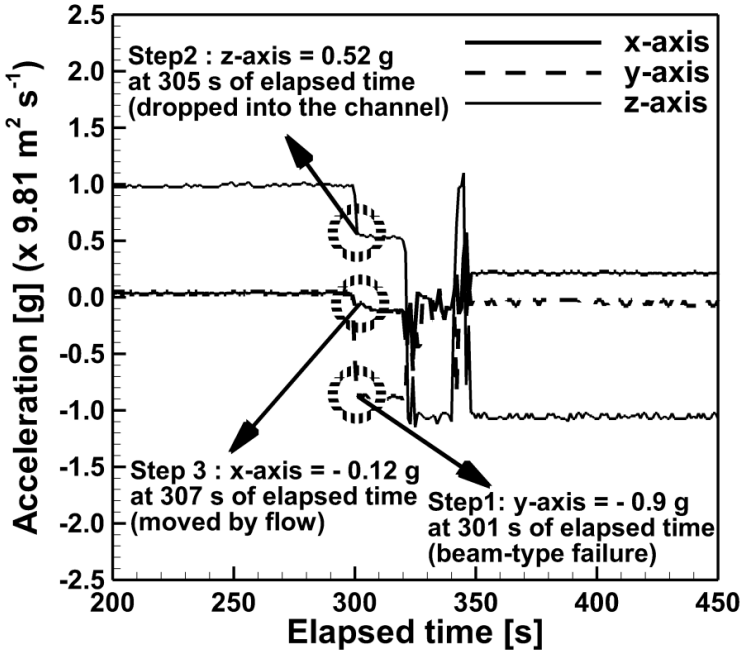


(a) Signal of beam-type failure mechanism.

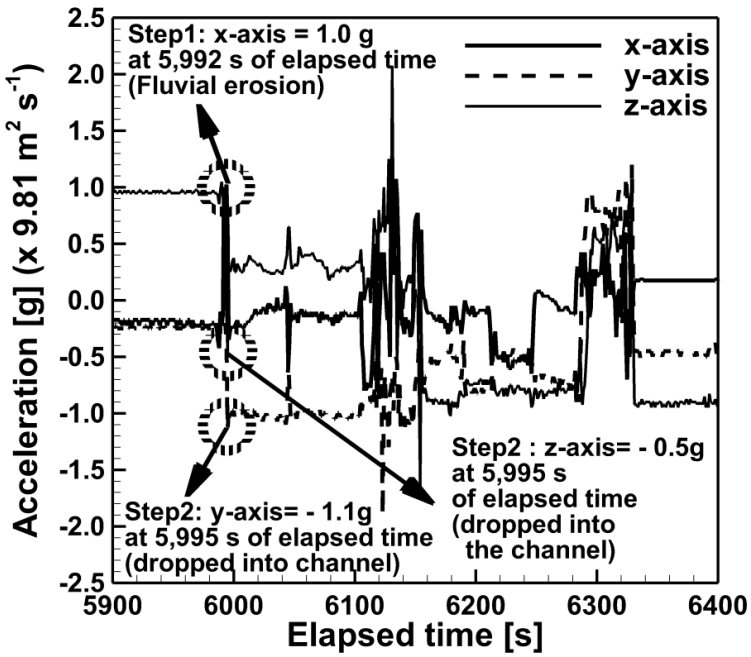


(b) Signal of fluvial erosion at the bank-toe.

**Fig. 5.2** Example results of data interpretations in Case 1.

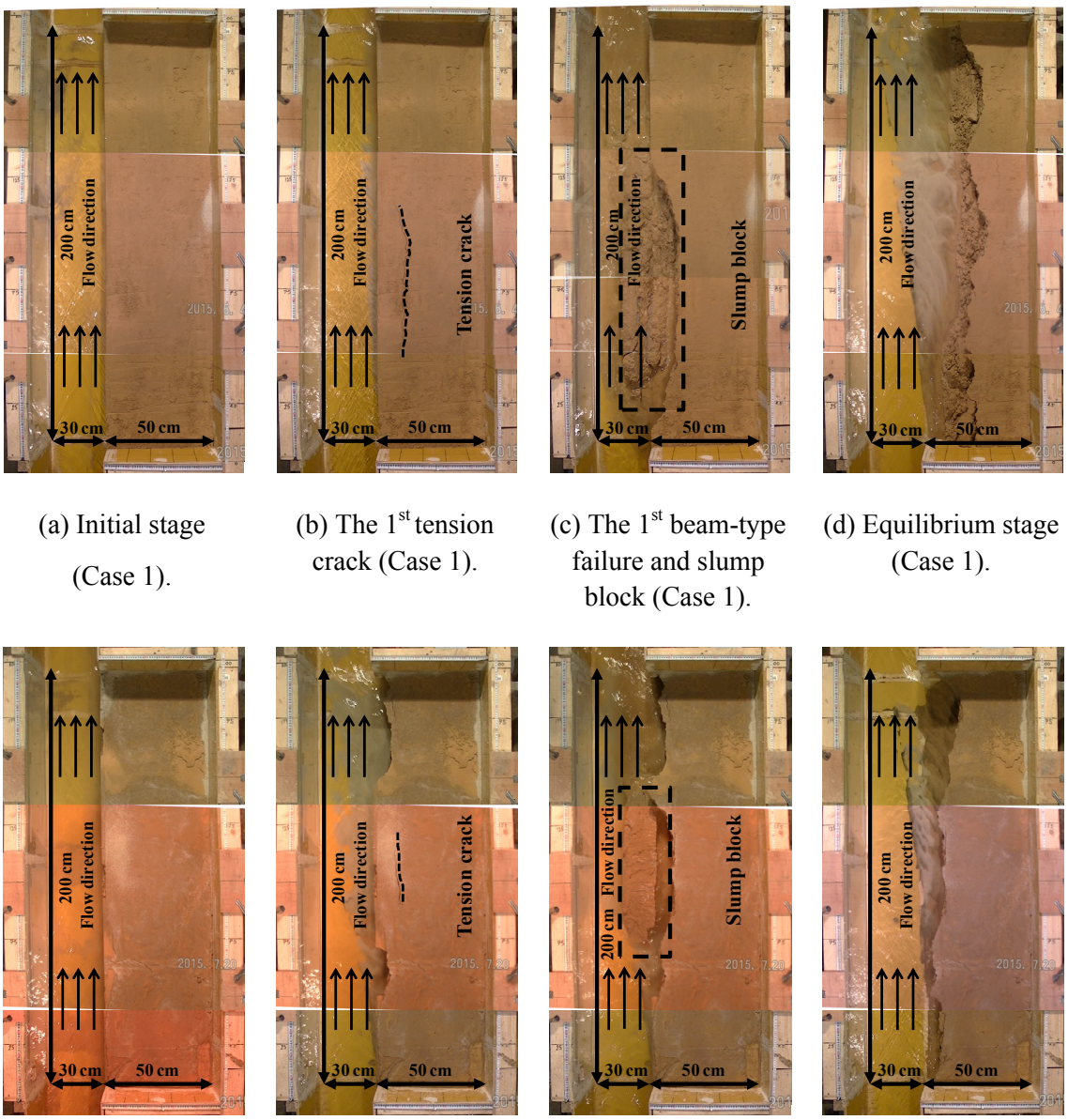


(a) Initial stage (Case 1).

(b) The 1st tension crack (Case 1).

(c) The 1st beam-type failure and slump block (Case 1).

(d) Equilibrium stage (Case 1).

(e) Initial stage (Case 2).

(f) The 4th tension crack (Case 2).

(g) The 4th beam-type failure and slump block (Case 2).

(h) Equilibrium stage (Case 2).

**Fig. 5.3** Example results of the experimental works in Cases 1 and 2.

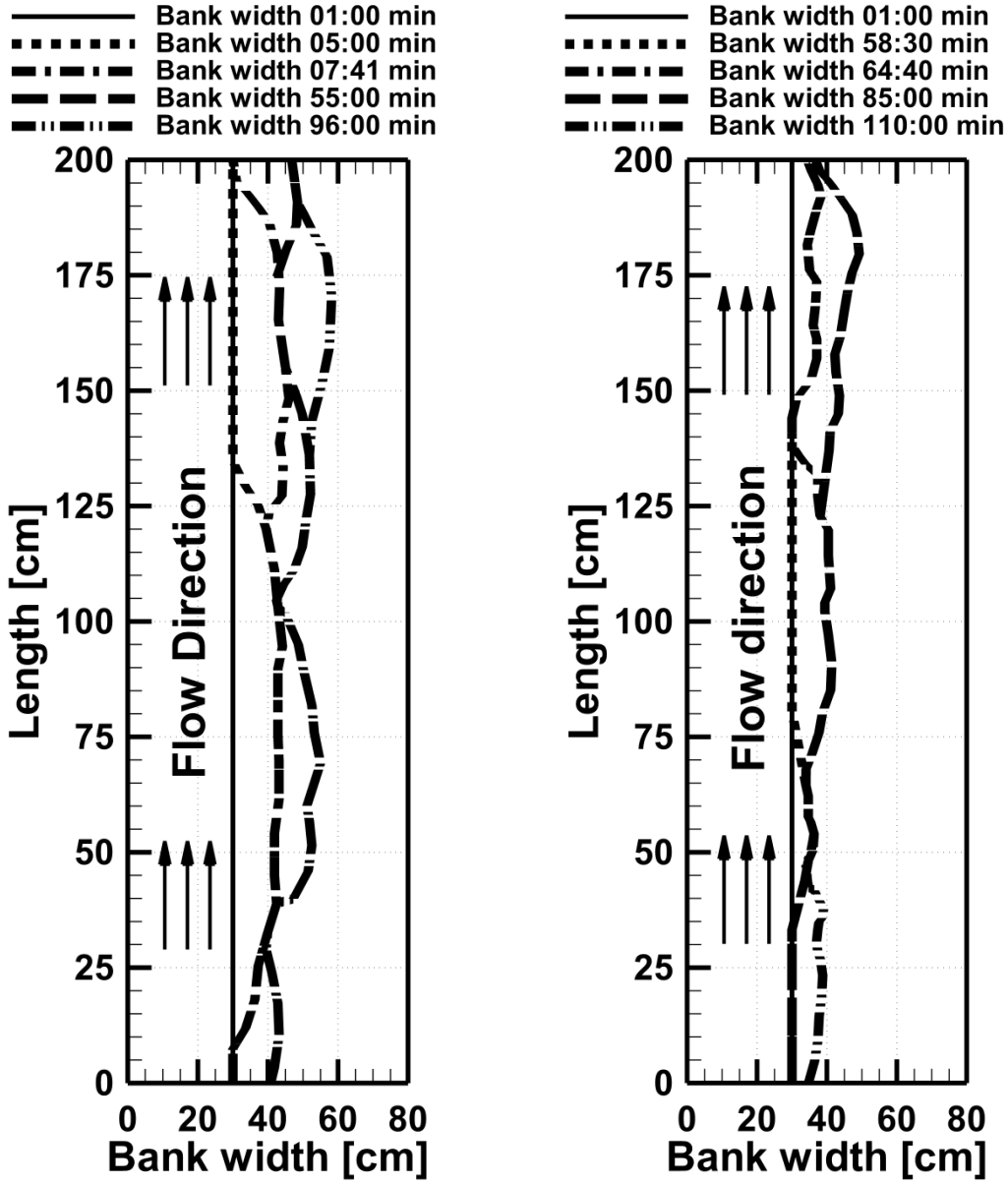


(a) Case 1.

(b) Case 2.

**Fig. 5.4** Schematic diagrams of spatial bank width in Cases 1 and 2.

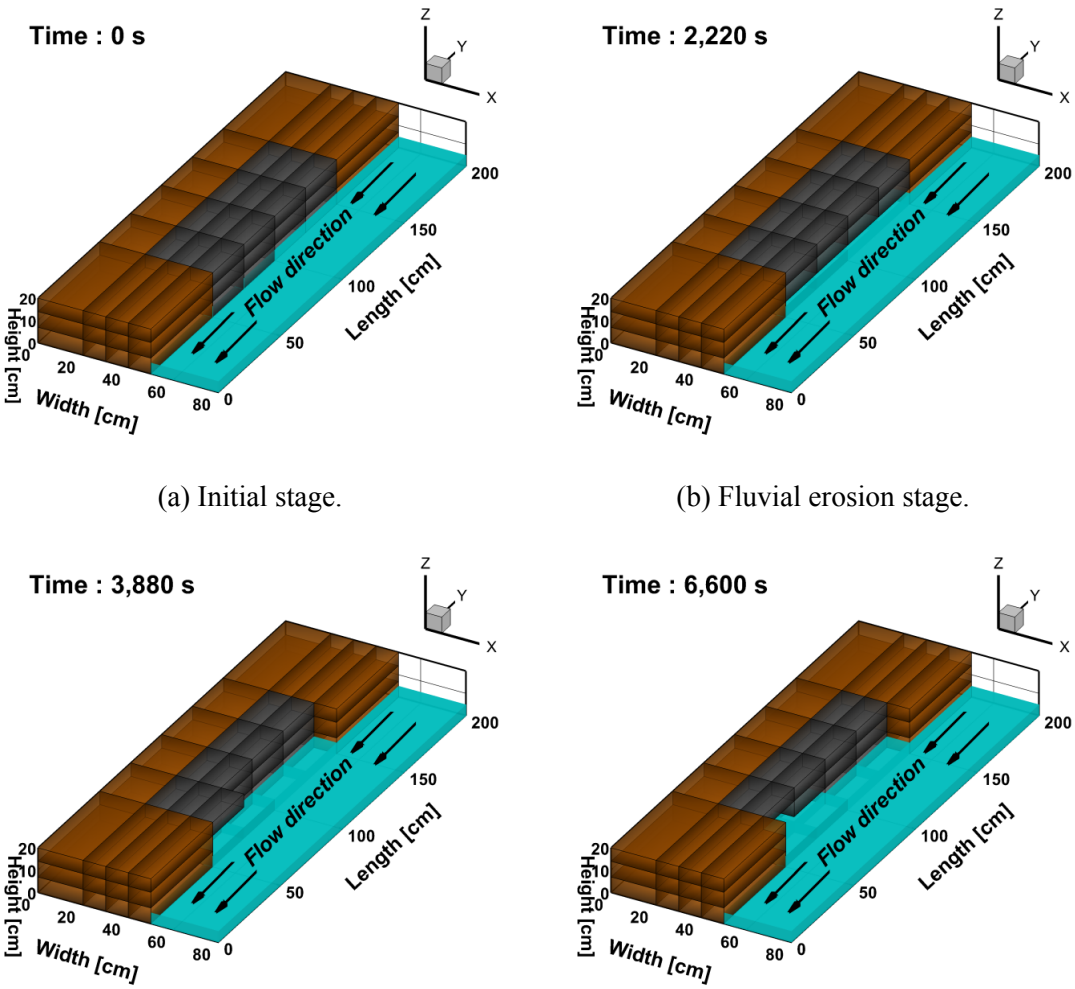


(a) Initial stage.

(b) Fluvial erosion stage.

(c) Beam-type failure stage.

(d) Equilibrium stage.

**Fig. 5.5** Example results of Case 2 (SC = 20%) using the acceleration sensors.

### 5.3.1 Case 1

In Case 1, fluvial erosion occurred immediately after the experiment started (see **Fig. 5.3(a)**). The first considerable tension crack and beam-type failure were observed from 7.4 to 134.7 cm from the upstream end at 296 s and at 300 s as shown in **Figs. 5.3(b)** and **5.3(c)**, respectively. Moreover, the failure block dimensions were 12.9 cm in width and 127.3 cm in length. For the first failure, the decomposition time, which is time of decay processes of the slump block on the bed channel, was 163 s. After beam-type failure, the riverbank slope reshaped toward an angle of 90°. A large tension crack and beam-type failure were then observed at the downstream end from 119.9 to 200.0 cm at 461 s. The slump block dimensions of this failure were 14.3 cm in width and 80.0 cm in length. Additionally, the decomposition time was 55 s. From 1,560 s to 9,420 s, six successive tension cracks and beam-type failures randomly developed along the cohesive riverbank. In addition, the decomposition time of the six successive failure blocks was within the range of 1,763 s to 3,981 s. Furthermore, the average water levels along the channel fluctuated between 5.0 cm and 5.5 cm during the experiment. Schematic diagrams of the temporal bank width of case 1 are showed in **Fig. 5.4(a)**. The experiment reached the equilibrium stage at 9,420 s (see **Fig. 5.3(d)**). Finally, a summary of experimental work is expressed in Table 5.3.

Table 5.3 Summary of failure times, failure block dimensions, failure block volumes and decomposition times (Case 1).

| Cantilever failure | Elapsed time (s) | Overhanging block failure | | | | Decomposition time (s) |
|---|---|---|---|---|---|---|
| | | Length (cm) | Width (cm) | Height (cm) | Volume ($cm^3$) | |
| I | 300 | 127.3 | 12.9 | 14.9 | 24,468.33 | 163 |
| II | 461 | 80.0 | 14.3 | 14.7 | 16,816.80 | 55 |
| III | 1,560 | 64.3 | 9.9 | 15.0 | 9,548.55 | 1,763 |
| IV | 3,300 | 51.8 | 8.6 | 14.5 | 6,459.00 | 2,960 |
| V | 5,760 | 54.7 | 14.2 | 14.6 | 11,340.00 | 2,899 |
| VI | 6,255 | 39.2 | 12.8 | 14.8 | 7,426.05 | 3,981 |
| VII | 7,200 | 32.4 | 10.4 | 14.8 | 4,987.00 | 2,277 |
| VIII | 9,420 | 17.5 | 11.5 | 14.7 | 2,958.37 | 3,917 |

### 5.3.2 Case 2

In Case 2, during the initial stage, fluvial erosion occurred along the cohesive riverbank but was more evident in the downstream region from the started time to 1,890 s as shown in **Fig. 5.3(e)**. In the first and second cantilever failures, the experiment showed a backward erosion process from 144.1 cm to 191.8 cm (at 1,890 s) and from 181.6 cm to 200.0 cm (at 3,120 s) from the upstream end. The third and fourth beam-type failures were then developed at the middle region of the cohesive riverbank from 33.3 cm to 138.3 cm from the upstream end at 3,510 s and at 3,880 s. The fourth tension crack is illustrated in **Fig. 5.3(f)**, and the fourth beam-type failure is shown in **Fig. 5.3(g)** using the video cameras and in **Fig. 5.5(c)** using the acceleration sensors. Tension cracks and beam-type failure were then observed in rapid succession at the downstream end again at 4,770 s and at 5,100 s from 122.8 cm to 168.8 cm and from 157.9 to 200.0 cm, respectively. Additionally, the last two beam-type failures developed at the upstream end at 5,505 s and at 6,600 s. For the failure block dimensions, the width and length of failure blocks were within the range of 5.7 cm to 13.5 cm and of 14.8 cm to 47.7 cm, respectively. The decomposition time for eight beam-type failures varied from 61 s to 904 s. Moreover, the average water level along the channel was in the range of 5.0 cm to 6.8 cm. Schematic diagrams of the temporal bank width of Case 2 are illustrated in **Fig. 5.4(b)**. The experiment reached the equilibrium stage at 6,600 s (see **Figs. 5.3(h)** and **5.5(d)**). Finally, a summary of experimental work (Case 2) is expressed in Table 5.4.

Table 5.4 Summary of failure times, failure block dimensions, failure block volumes and decomposition times (Case 2).

| Cantilever failure | Elapsed time (s) | Overhanging block failure | | | | Decomposition time (s) |
|---|---|---|---|---|---|---|
| | | Length (cm) | Width (cm) | Height (cm) | Volume ($cm^3$) | |
| I | 1,890 | 47.7 | 6.8 | 14.5 | 4,703.22 | 289 |
| II | 3,120 | 18.4 | 7.1 | 14.6 | 1,907.34 | 61 |
| III | 3,510 | 47.3 | 5.7 | 14.4 | 3,882.38 | 175 |
| IV | 3,880 | 73.8 | 10.9 | 14.7 | 11,824.97 | 290 |
| V | 4,770 | 45.9 | 12.3 | 13.5 | 7,621.69 | 269 |
| VI | 5,100 | 42.1 | 13.5 | 13.2 | 7,502.22 | 904 |
| VII | 5,505 | 42.4 | 8.2 | 13.5 | 4,693.68 | 118 |
| VIII | 6,600 | 14.8 | 5.7 | 14.7 | 1,240.09 | 107 |

The experimental results showed that fluvial erosion had the greatest effect on the occurrence of cantilever failure instability because such erosion increased the width of an overhanging block but decreased its stability. This process was captured using side view video cameras and the varied acceleration signal in the *x*-direction as shown in **Fig. 5.5(b)**. That was because fluvial erosion is related to loosening of weak bonds between the material particles. The observations from the present experiments were similar to those of previous studies (Abam, 1997; Darby et al., 2007; Patsinghasanee et al., 2015b, 2015c; Rinaldi & Nardi, 2013; Thorne & Tovey, 1981). Tension cracks then developed on the upper surface of the cohesive riverbanks. Such tension cracks seemed to develop only when the cantilever was already close to failure. After that, the cantilever failure occurred along the tension crack line. The dominant failure mechanism was observed to be beam-type failure clarified using the acceleration signal in the *y*-direction as shown in **Fig. 5.5(c)**. This was consistent with the findings of previous researchers, who have suggested that the beam-type failure may be prevalent (Nardi et al., 2012; Patsinghasanee et al., 2015b, 2015c),

## 5.4 DISCUSSION

For the flow conditions, the Reynolds numbers (Re) were within the range of 15,000 to 40,000 and the Froude numbers (Fr) were lower than one (Table 5.1), which corresponded to a turbulent flow and a subcritical flow regime, respectively. In general, the Froude numbers is adopted here to represent a

large number of alluvial rivers where the flow condition is subcritical flow (Dulal & Shimizu, 2010; Lewin, 1979; Patsinghasanee et al., 2015b, 2015c; Peakall et al., 2007).

The rate of fluvial erosion of the experimental results in Case 1 (SC = 30%) was greater than that in Case 2 (SC = 20%) under similar hydraulic conditions, as shown by the accumulated riverbank failure width in **Fig. 5.6**. The fluvial erosion rates at the equilibrium stages of Cases 1 and 2 were 0.0025 cm/s and 0.0014 cm/s, respectively. The main reason is that the riverbank with lower cohesive force are more susceptible to failure than those with higher cohesive force. Additionally, the silt-clay content could be expected to have some bearing on the susceptibility of the cohesive riverbanks to the subaerial erosion process, as the cohesive materials with a lower cohesive force (higher silt-clay content) have greater plasticity (and hence a capacity for swelling and shrinkage) (Couper, 2003; Dulal & Shimizu, 2010; Julian & Torres, 2006; Patsinghasanee et al., 2015b, 2015c).

The experiments were able to randomly reproduce cantilever failures—as illustrated in **Fig. 5.4**—and the experimental results showed a backward erosion process in Case 2 (high cohesive force), which was similar to previous observations (Hooke, 1980; Laubel et al., 2003; Patsinghasanee et al., 2015b, 2015c). In the present study, riverbank particles were detached from the downstream region through the effect of a second wooden panel by the generation of a reverse flow. This process is summarized as follows. The flow from the channel hits the second wood panel (III to IV) as shown in **Fig. 5.1** and is reversed, with high velocity, to erode the cohesive riverbanks at the downstream region. For that reason, this study considered only the center region and used streamwise-averaged data of cohesive riverbanks to reduce the effect of the wooden panel.

The slump block formation and decomposition were the new phenomena observed in the present experiments. The slump block seemed very complex, and its dependability was very important to the cantilever failure process at the experimental scale. In the present study, the effect and role of the slump block on cantilever failure were observed and described for the first time at the experimental scale. Moreover, the effect of slump blocks on the bed channel in front of the riverbank, where they formed a sediment buffer that reinforced the riverbank and reduced fluvial erosion, was observed. **Figs. 5.3c** and **5.3g** shows the slump blocks in the rectangular blocks. The average slump block dimensions in width, length and height for two different cohesive forces are presented in **Fig. 5.7**, which shows a decreasing trend for the width and length of the slump blocks in the case of the higher cohesive force. Therefore, the geometries of the slump block including its failure and decomposition mainly depended on the cohesive force of the cohesive riverbanks. A reduction of the cohesive force not only increased the fluvial erosion rate but also affected the dimensions of the slump blocks and their decomposition rates (see **Figs. 5.6** and **5.7**). The observation phenomena from the present work were consistent with previous studies in terms of changing cohesive force (silt-clay content) (Couper, 2003; Dulal & Shimizu, 2010; Julian & Torres, 2006; Patsinghasanee et al., 2015b, 2015c). **Fig. 5.8** shows the relationship between the volumes of slump blocks and their decomposition times in the present study. The relation seems to be almost random, without any identifiable rules governing this phenomenon because the decomposition process is dependent on the processes such as weathering, fluvial erosion, general disintegration, and removal (Wood et al., 2001). This random relationship between the volumes of slump blocks and their decomposition times has been reported in previous observations (Dulal & Shimizu, 2010).

Additionally, the armoring effect of the slump block was revealed in the experimental results. The detachment from the slump and re-suspension of the materials sank and deposited in the submerged

failure materials on the bed channel in front of the riverbank, which is shown as a layer at the top of failure materials (see **Fig. 5.9**). Therefore, this mechanism increased the strength of the bank-toe.

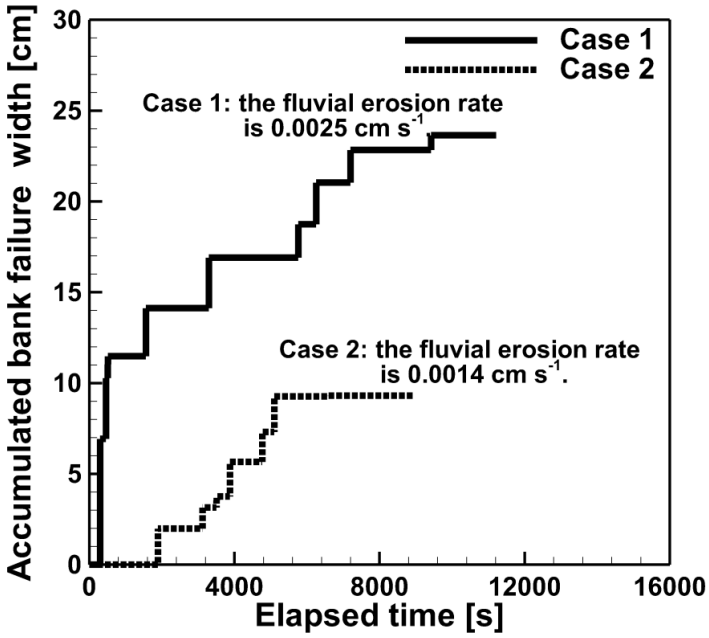


**Fig. 5.6** Comparison results of fluvial erosion rate in the experimental studies with the different silt-clay contents.

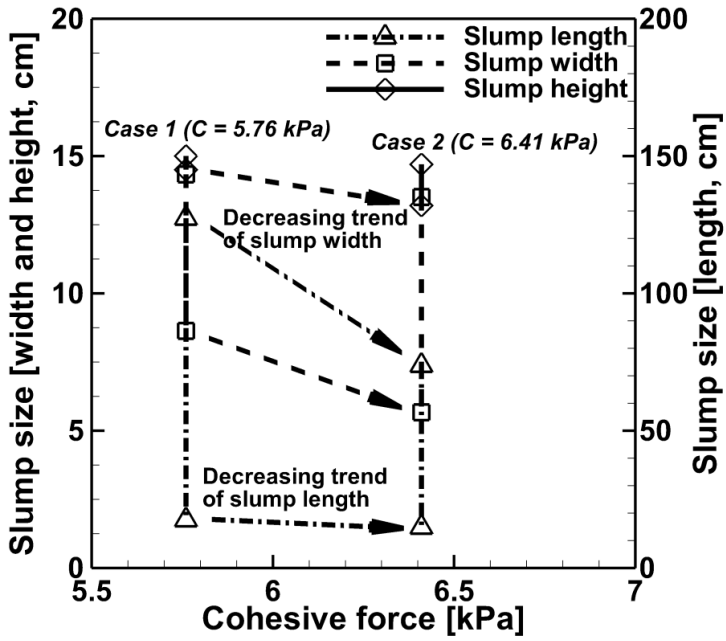


**Fig. 5.7** Variation of slump block dimensions with the different cohesive forces. (Dash-dotted and dashed lines show a decreasing trend for the length and width of the slump blocks, respectively.)

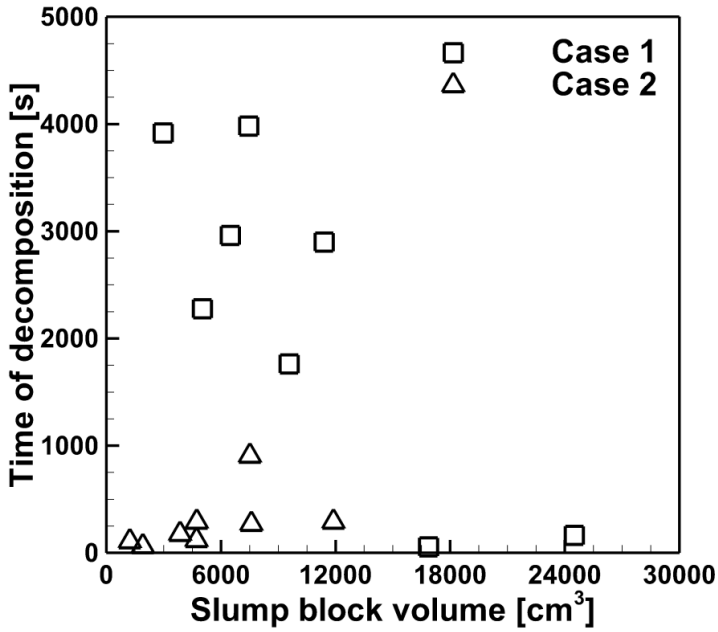


**Fig. 5.8** Slump decomposition of the various volumes with the different cohesive forces.

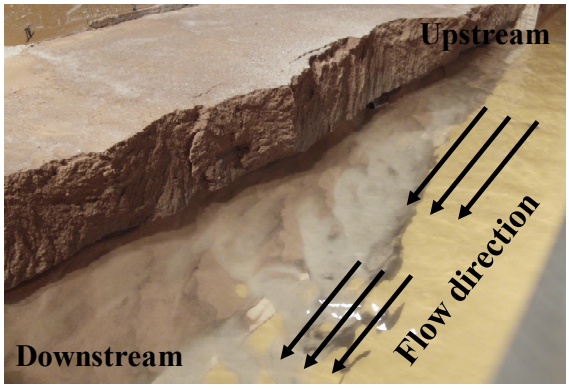


(a) The armoring effect during experimental run.

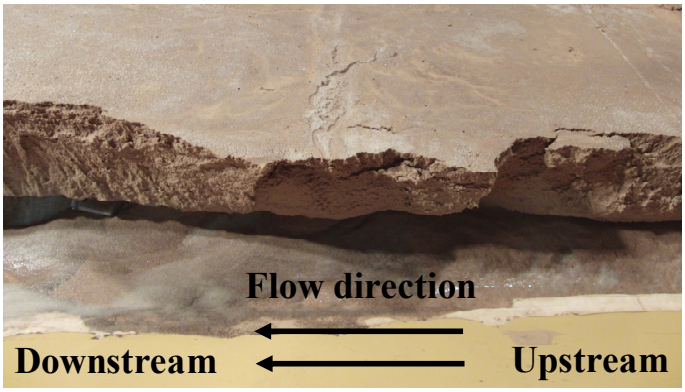


(b) The armoring effect after the equilibrium stage.

**Fig. 5.9** Armoring effect of the experimental results (Case 2).

## 5.5 SUMMARY

This study elucidated the complex mechanisms of cantilever failure with consideration given to the slump block by means of laboratory experiment. Two types of cohesive materials with different percentages of silt-clay content were investigated under similar hydraulic condition using the acceleration sensors to clarify the cantilever processes. The main summaries from the results are as follow.

For the complex mechanism of a cantilever failure, the experimental results expressed that fluvial erosion at the submerged zone generates an overhanging block in the upper part of the cohesive riverbanks. Tension cracks then developed on the upper surface of the cohesive riverbanks and the cantilever failure after that occurred along the tension crack line. The dominant failure mechanism was observed to be beam-type failure, which was clarified by using the acceleration sensors installed inside the cohesive riverbanks. The mechanisms of a cantilever failure are consistent with the finding of previous researches (e.g., Darby et al., 2007; Patsinghasanee et at., 2015b, 2015c; Samadi et al., 2013; Thorne & Tovey, 1981). In addition, the experimental results indicate that cohesive riverbanks with higher silt-clay contents are more susceptible to failure than those with lower silt-clay contents. These experimental observations are similar to previous works in term of changing silt-clay content (Couper, 2003; Dulal & Shimizu, 2010; Julian & Torres, 2006; Patsinghasanee et at., 2015b, 2015c). The slump block failure and decomposition phenomena are discussed for the first time with the cantilever failure experiments on channel flow. Slump blocks were observed on the bed channel in front of the riverbank, where they formed a sediment buffer that reinforced riverbanks and reduced fluvial erosion. The slump block phenomena for the formation and deformation showed a significant effect on the cohesive force of the riverbanks and affected the riverbank geometry. Therefore, a reduction of the silt-clay content leads to smaller slump block dimensions as well as faster decomposition. Observations from the other works are similar in terms of the relationship between the cohesive force and slump block dimensions as well as decomposition times (Dulal & Shimizu, 2010). The relationship between the slump block volumes and their decomposition times in the present study seems to be almost random, without any identifiable rules governing this phenomena. This random relationship between the slump block volumes and their decomposition times has been reported in previous observations (Dulal & Shimizu, 2010).

# Chapter 6

# NUMERICAL SIMULATION OF A CANTILEVER FAILURE WITH THE EFFECT OF SLUMP BLOCKS FOR COHESIVE RIVERBANKS

## 6.1 INTRODUCTION

A cantilever failure among the various riverbank failures is common phenomena observed in the natural rivers and it affects a wide range of physical, ecological and socioeconomic issues in the fluvial environment (Taghavi et al., 2010). However, the reproduction and simulation of a cantilever failure mechanism using a numerical model are a challenging task for understanding riverbank failure phenomenon before any new construction works such as ripraps, gabions, mattresses and pipe line crossings, etc.

For previous studies, researchers have been unable to analyze a cantilever failure and have focused mainly on simple bank failures such as rotational slip failure, toppling failure and mass wasting failure (ASCE, 1998; Duan, 2005; Osman & Thorne, 1988). Only a few studies have applied stability analyses based on the safety factor of the portion with cantilever failure, upon which three types of possible cantilever failure mechanisms have been defined: shear-type, beam-type and tensile-type failures (Abam, 1997; Thorne & Tovey, 1981). After cantilever failure, the overhanging blocks crumble down in a shape like slump blocks and cover the bank-toe. It is thought that the fluvial erosion rate decreased because of the failure of slump blocks (Dulal et al., 2010). The simplified process of slump blocks was developed in a two-dimensional depth-averaged model for reproducing meandering evolution process in small-scale experiments (Dulal et al., 2010) and natural rivers (Parker et al., 2011). The previous studies (Dulal et al., 2010; Parker et al., 2011) employed the simple bank failure concept with the slump block effect based on submerged angle of repose. In such model, when the riverbed near the riverbank erodes and the cross sectional gradient of the riverbank slope becomes steeper than the angle of repose, the slump block is assumed to be generated. After that, the slump block is deposited at the bank-toe and the riverbank is then armored. However, the simple bank failure concept cannot reproduce the complex mechanisms of a cantilever failure (Patsinghasanee et al., 2015b, 2015c). Therefore, the previous slump block concepts cannot apply for simulating cantilever failure phenomena. Furthermore, simplified hypotheses have been addressed to general slump block dimensions deposited at the bank-toe. However, the impact of slump blocks was not considered on the bank geometry (Motta et al., 2014).

For numerical model, a coupled model of fluvial erosion and mass wasting was developed to reproduce fluvial erosion processes in a bank-toe, degradation in a channel bed and destabilization of an upper bank (Darby et al., 2007; Duan & Julien, 2010; Langendoen et al., 2008; Motta et al., 2014; Rinaldi et al., 2008). In a cantilever failure model, the numerical model was developed to identify the overhanging block dimensions and cohesive force, which are highly significant for a cantilever

stability (Samadi et al., 2011). Additionally, the overhanging block model was applied for computing the safety factor by limited equilibrium method, defined as the ratio between stabilizing and destabilizing forces (Samadi et al., 2013). However, these previous studies have limitations in the coupling fluvial erosion and cantilever failure.

A coupling fluvial erosion and cantilever failure model was recently proposed to simulate the subsequent failure of the overhanging block as expressed in Chapter 3 and 4 (Patsinghasanee et al., 2015a, 2015b, 2015c, 2016d). The limitation of the recent modeling (Patsinghasanee et al., 2015b, 2015c) was in the quantification of the fluvial erosion rate ($\varepsilon$) derived from the erodibility coefficient ($k_d$) because the determination of $k_d$ still remains complex, depended on several factors (i.e., water content, cohesive force and silt-clay content) (Couper, 2003; Grabowski et al., 2011; Julian & Torres, 2006). Thus, for the determination of $\varepsilon$, the relationship of $k_d$ and $\tau_{bc}$ are needed to be measured locally. However, these previous study (Chapter 3 and 4) has the another limitation in the coupling fluvial erosion and cantilever failure with the slump block effect (Patsinghasanee et al., 2015a, 2015b, 2015c, 2016d) and simulations coupling fluvial erosion, cantilever failure and slump block consideration therefore need to be conducted.

To deal with the limitations in the previous numerical models of the processes for a cantilever failure, a novel coupled numerical model by considering the effects of fluvial erosion, cantilever failure, slump block and bedload sedimentation was developed to simulate the cantilever failure mechanism in the experimental scale (Chapter 5).

## 6.2 METHODOLOGY

As noted previously, the previous studies had limitations in the coupling fluvial erosion and cantilever failure with the slump block effect. Therefore, the main objective of the present coupling model is to reproduce the physical mechanisms of fluvial erosion, tension crack, cantilever failure, slump block, and bedload sedimentation of the cohesive banks.

A cantilever failure model was developed by implementing a triple-grid approach, consisting of a coarse one-dimensional (1D) grid for the flow field in the lateral direction; a fine 1D grid for sediment transport and bed deformation in lateral direction; and a 2D grid for cantilever failure, and slump block in the vertical and lateral directions (**Fig. 6.1**). During the initial stage of the computation (**Fig. 6.2**), the model reproduces fluvial erosion at the lower part around the wetted perimeter of the cohesive bank, which is shown by the dash-dotted line in zone I. Next, the tension crack in zone II and the cantilever failure in zone III (the dashed vertical line along the riverbank) are captured. For beam-type failure, the failure block is turned into the channel at $90^{\circ}$ in the anti-clockwise direction and dropped at bed channel (see **Fig. 6.3(a)**). The pivot of the rotation is located at the lowest edge of the failure block along the overhanging failure plane. In contrast, the overhanging failure block directly comes to rest at the intermediate drop point for shear-type failure (**Fig. 6.3(b)**). The slump block failure and decomposition are then developed at the toe of the bank slope in zone IV (**Fig. 6.2**). This approach involves applying the four submodels—fluvial erosion, cantilever failure, slump block and bedload sedimentation—at each of a series of discrete timesteps. A logic diagram of the computational sequence used for the coupled mechanism is illustrated in **Fig.6.4**.

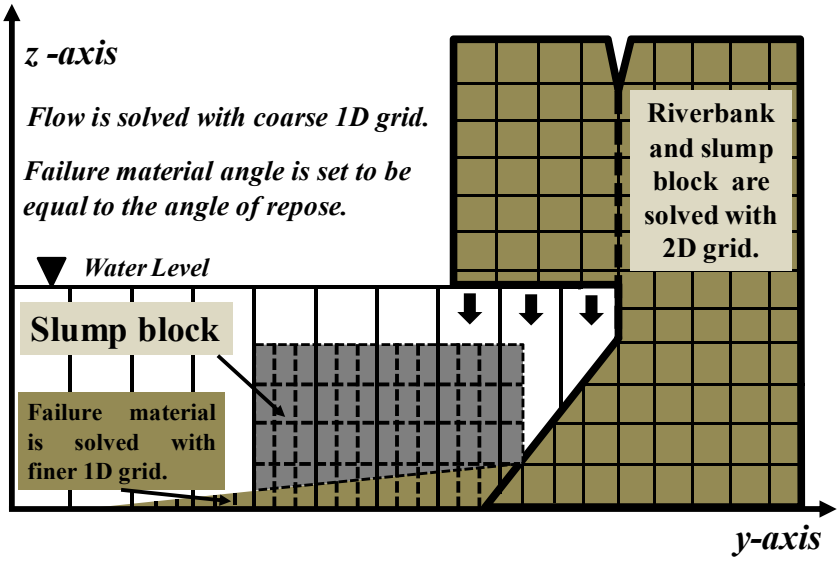


**Fig. 6.1** Framework of triple-grid approach of cantilever failure model with the slump block consideration.

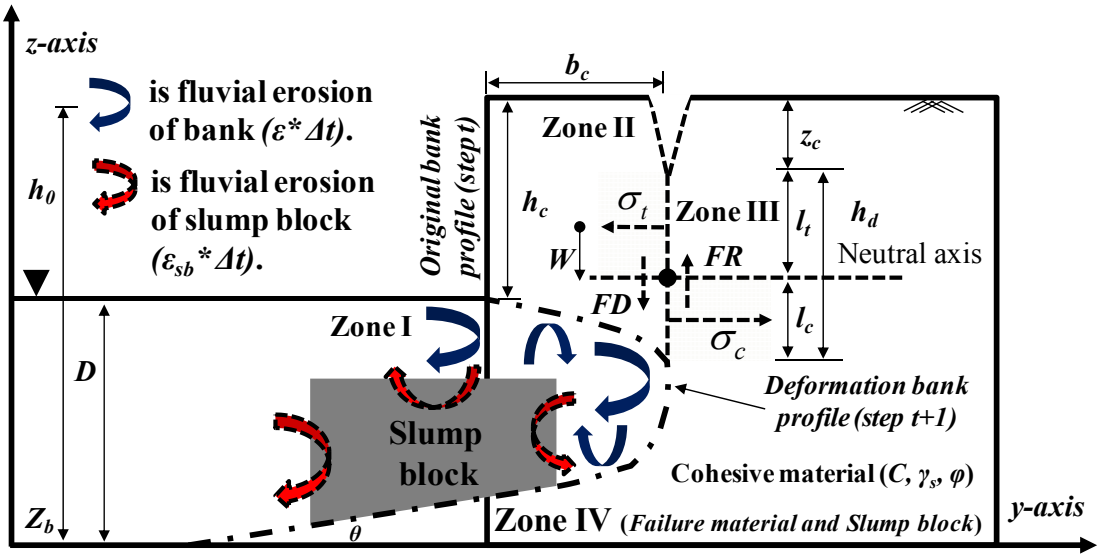


**Fig. 6.2** Overhanging geometry with the slump block consideration and forces exerted on the incipient failure block. $h_0$ is initial bank height (m), $h_c$ is overhanging block height (m), $b_c$ is overhanging block width (m), $z_c$ is tension crack depth (m), $\tau_{bo}$ is actual shear stress (Pa), $\tau_{bc}$ is critical shear stress (Pa), $l_t$ is tensile zone length (m), $l_c$ is compressive zone length (m), $D$ is water depth (m), $Z_b$ is bed elevation in calculation grid cell (m), $W$ is overhanging block weight (kN), $C$ is the cohesive force (Pa),$\sigma_t$ is tensile stress (kN/m$^2$), $\sigma_c$ is compressive stress (kN/m$^2$), $FR$ and $FD$ are resultant resisting and driving forces acting on the overhanging failure block, $\theta$ is angle of repose, $\phi$ is internal friction angle, $\gamma_s$ is unit weight of soil (kN/m$^3$), $\varepsilon$ is the fluvial erosion rate (m/s) and $\varepsilon_{sb}$ is the fluvial erosion rate of the slump block (m/s).

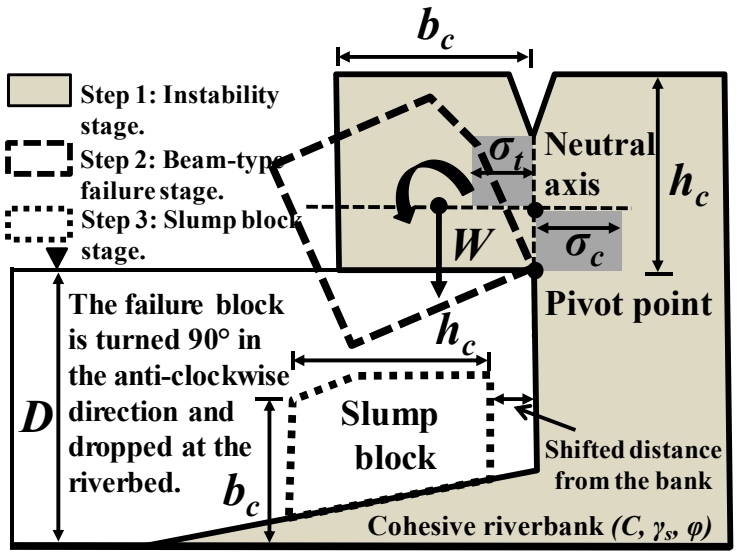


(a) Beam-type failure.

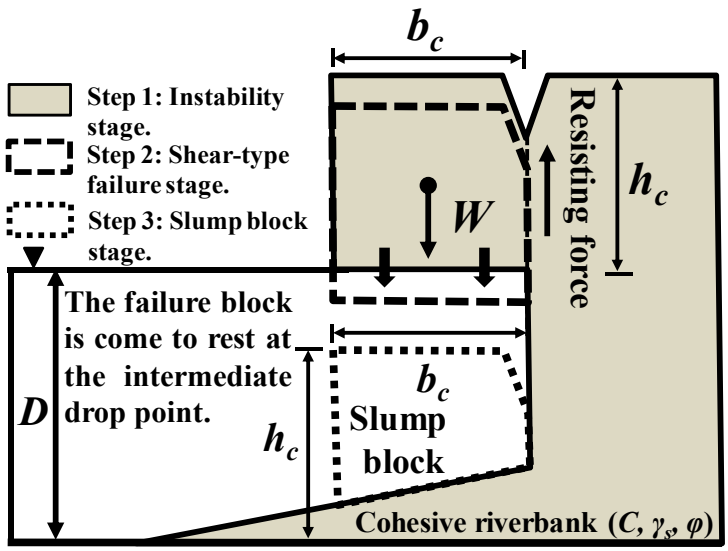


(b) Shear-type failure.

**Fig. 6.3** Slump block locations and dimensions.

### 6.2.1 Fluvial Erosion Rate

The flow field is calculated using a uniform flow model on a coarse lateral 1D grid cell (Process 1 in **Fig. 6.4**) (Sturm, 2001). In order to avoid the small grid cell width in the vicinity of the cohesive bank, the grid cell division is defined from the edge of the bank instead the left side of the computational domain. Therefore, the flow field equation can considers the complicated shape of the fluvial erosion near the bank by evaluating the hydraulic radius in a coarse lateral grid cell.

$$u_j = \frac{1}{n} R_j^{2/3} i^{1/2} \tag{6.1}$$

where $u_j$ is the velocity in each calculated cell, n is the Manning roughness parameter along the channel (0.011) calculated using the Manning–Strickler equation ($k_s^{1/6}/7.66g^{1/2}$) in which $g$ is the gravitational acceleration (9.81 m/s$^2$), and $k_s$ is the roughness height defined as 1-3$d_{50}$, $R_j$ is the hydraulic radius in each calculated cell ($A_j/P_j$), where $A_j$ being the cross-sectional area in each calculated cell, and $P_j$ being the perimeter length in each calculated cell, i is the bed slope, and j is the lateral calculated cell number.

The fluvial bank erosion rate is quantified using an excess shear stress formula around the wetted perimeter (Process 2 in **Fig. 6.4**), including bottom, lateral and top sides of the cohesive bank (see the blue arrows in **Fig. 6.2**) as given below (Arulanandan et al., 1980; Partheniades, 1965).

$$\varepsilon = k_d \left( \tau_{b0} - \tau_{bc} \right)^a \tag{6.2}$$

where $\varepsilon$ is the fluvial erosion rate of the bank (m/s), $k_d$ is the erodibility coefficient (m$^3$/(N s)), $\tau_{b0}$ is the actual shear stress applied by the flow (Pa), $\tau_{bc}$ is the critical shear stress (Pa), and a (dimensionless) is the exponent generally assumed to equal one. In Eq. 6.2, the positive value of excess shear stress is only considered for fluvial erosion estimation. Although Eq. 6.2 appears simple, it includes a complicated parameter ($k_d$). The value of $k_d$ is determined through the comparison with the results of the preliminary experimental studies (Darby et al., 2007; Kamaker & Dutta, 2011).

The actual shear stress is determined by the function of hydraulic radius and channel slope in each calculated cell, as shown in Eq. 6.3. The empirical equation of the critical shear stress for the function of the percentage of silt-clay content (SC) is employed as expressed in Eq. 6.4 (Julian & Torres, 2006; Vanoni, 1977).

$$\tau_{b0} = \rho g R_j i \tag{6.3}$$

$$\tau_{bc} = 0.1 + 0.1779(SC) + 0.0028\left(SC^2\right) - 2.34E^{-5}\left(SC^3\right) \tag{6.4}$$

where $\rho$ is the density of water (1,000 kg/m$^3$).

To characterize the fluvial erosion rate eroded around the wetted perimeter of the bank, the fluvial erosion rate (Eq. 6.2) is evaluated in each timestep by the function of the $k_d$, $\tau_{b0}$ and $\tau_{bc}$ to erode the bank in the vertical, and lateral directions. For actual shear stress, this procedure is a simple method to evaluate the near-bank shear stress by neglecting the lateral shear stress because the secondary current in straight experimental flume show velocities of approximately 2% of the streamwise velocity (Blanckaret et al., 2010; Nezu et al., 1993). In addition, the shear stress distribution on the bank instead of a constant shear stress does not significantly change the simulation results (Motta et al., 2014). As a result, this procedure is an idealization of the fluvial erosion rate estimation, and was used simply to simulate the coupled numerical model of cantilever failure phenomena.

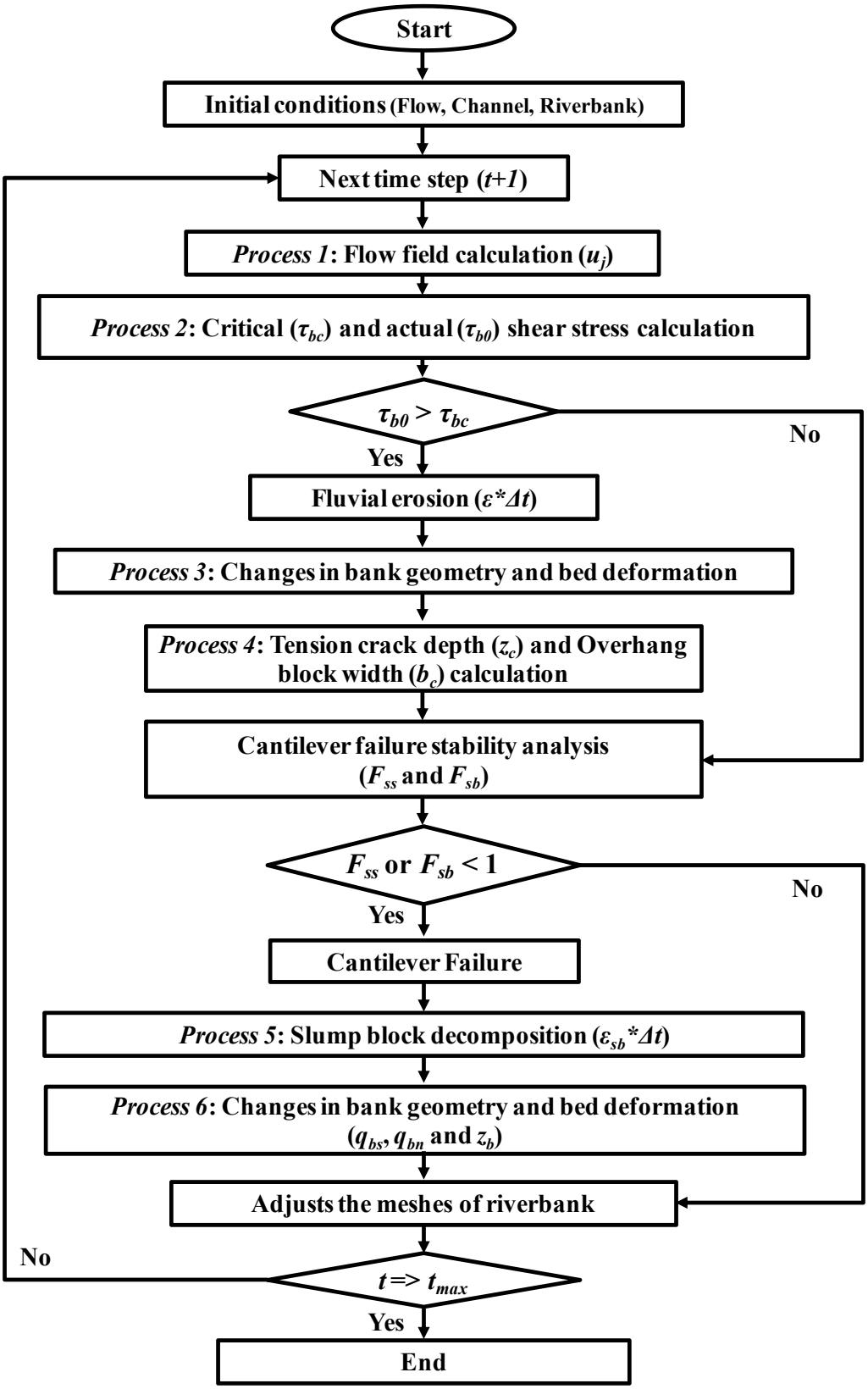


**Fig. 6.4** Logic diagram of the computational sequence of a cantilever failure with slump block effect.

For the computational process of fluvial erosion, the bank profiles are deformed in accordance with the fluvial erosion simulated at the end of each discrete timestep (Process 3 in **Fig. 6.4**). Therefore, the undisturbed cell occupation rate ($\Omega_t$) is achieved, as expressed in Eq. 6.5 through two possible schemes (see **Fig. 6.5**).

$$\Omega_t = \frac{[V_{org} - \sum_{t=1}^{n} V_{erd}]}{V_{org}} \tag{6.5}$$

where $V_{org}$ is the initial grid cell volume of a cohesive bank ($m^3$), and $V_{erd}$ is the simulated fluvial erosion volume in each timestep ($m^3$).

For the first scheme, if the accumulated fluvial erosion volume is less than the initial grid cell volume of the bank, the boundary nodes are not shifted horizontally inward through the fluvial erosion (**Fig. 6.5(a)**). For the second scheme, if the accumulated fluvial erosion volume is equal to or larger than the initial grid cell volume of the bank, the new grid cells are assigned to update the new bank profile nodes (**Fig. 6.5(b)**).

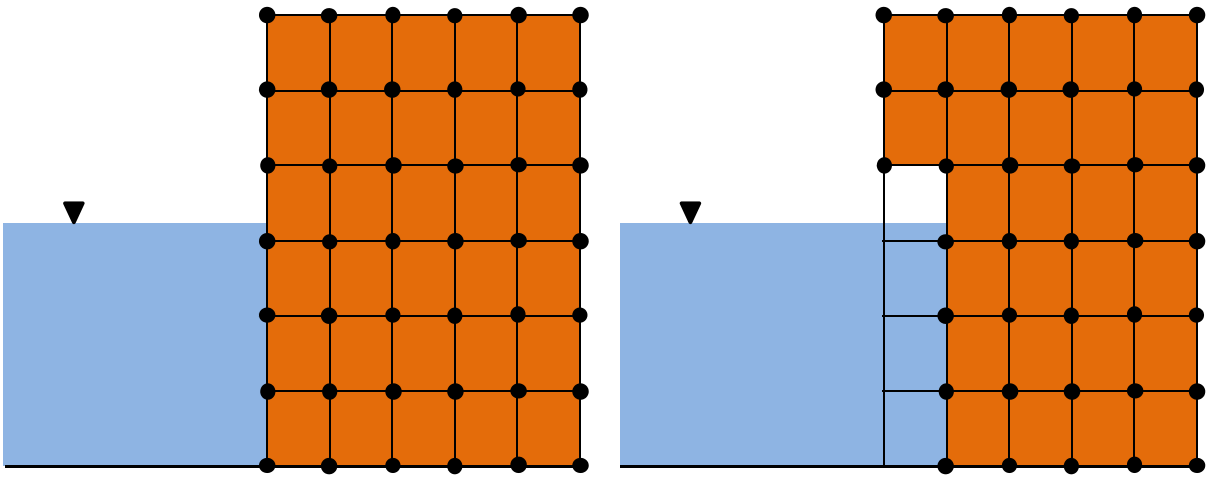

(a) The first scheme. (b) The second scheme.

**Fig. 6.5** Illustration of the two schemes used to adopt the boundary nodes by the effect of fluvial erosion.

### 6.2.2 Cantilever Failure

For a cantilever failure, the overhanging failure blocks were defined by considering the factor of safety for the two types of failure (i.e., based on shear-type, and beam-type failure mechanisms); tensile failure was omitted because such failure have rarely been observed along natural rivers (Darby et al., 2007). A cantilever failure will occur if any of the overhanging blocks have a safety factor of less than one (Process 4 in **Fig. 6.4**). The two types of cantilever failure mechanisms applied in this study are described by Thorne & Tovey, (1981) for shear-type failure and Micheli & Kirchner, (2002) for beam-type failure. In addition, the advantage of this numerical model is that this study developed the coupled fluvial erosion and cantilever failure with the two types of failure mechanism because the previous numerical models only considered the shear-type failure for the reproduction of overhanging block failure (Darby et al., 2007; Duan & Julien, 2010; Langendoen et al., 2008; Motta et al., 2014; Rinaldi et al., 2008; Samadi et al., 2013).

Shear-type failure involves shear stress along the vertical plane. Such failure is expected when the shear stress along the vertical plane from the overhanging block weight (*FD*) exceeds the resisting force of cohesive riverbank (*FR*), as shown in **Figs. 6.2** and **6.3(b)**. The safety factor of shear-type failure ($F_{ss}$) is described as

$$F_{ss} = \frac{C\,h_d}{\gamma_s A_b} \tag{6.6}$$

where $C$ is the cohesive force (Pa), $h_d$ is the effective length (m), $\gamma_s$ is the unit weight of soil (kN/m$^3$), and $A_b$ is the cross-sectional area of overhanging block (m$^2$).

Beam-type failure is related to unstable overhanging blocks by rotation around a neutral axis (**Figs. 6.2** and **6.3(a)**). Above the axis failure is in tension and below it, in compression. Failure occurs when the rotational moment of overhanging block overcomes the resistive moments of soil's strength in the tension and compression zones. Then, the safety factor of beam-type failure ($F_{sb}$) can be described as

$$F_{sb} = \frac{\sigma_c\, l_c^2 + \sigma_t\, l_t^2}{\gamma_s\, h_c\, b_c^2} \tag{6.7}$$

with $h_d = l_c + l_t$ and $\sigma_c/\sigma_t = l_t / l_c$, where $l_c$ and $l_t$ are the overhanging length under compressive and tensile strength (m), respectively; $\sigma_c$ and $\sigma_t$ are the compressive and tensile strength (kN/m$^2$), respectively. To link the cohesion and tensile strength of cohesive material, the equation of Fang & Hirst, (1973), and Fang & Daniels, (2006) was employed as

$$\sigma_t = \frac{C}{\xi} \tag{6.8}$$

where $\xi = 1/[0.34+0.01I_w]$ where $\xi$ is the ratio of tensile strength to cohesion, and $I_w$ is the plasticity index. Finally, based on the Chen-Drucker modified Mohr-Coulomb criteria (Chen & Drucker, 1969), the compressive strength ($\sigma_c$) is computed using:

$$\sigma_c = 2C\tan\left(45 + \frac{\phi}{2}\right) \tag{6.9}$$

where $\phi$ is the internal friction angle.

The tension crack depth ($z_c$) is assumed to be 0.5 of the overhanging block height because the ratio of tension crack depth and overhanging block height from 0.3 to 0.7 does not typically change the factor of safety by more than 10% (Thorne & Abt, 1993).

### 6.2.3 Slump Block Effect

For slump block effect, a novel slump block scheme was proposed in this chapter. The overhanging block immediately drops into bed channel and becomes a slump block following a cantilever failure. Previous slump block study mentioned that the overhanging block dimensions show the formation patterns according to the governing fluvial erosion and cantilever failure type (Wood, 2001). Here, this complexity is implicitly represented by the following assumption. The slump block dimensions are assumed to be equal to the overhanging block dimensions ($h_c$ and $b_c$). However, the settled

dimensions and positions of the slump block are different characteristics between shear-type and beam-type failures (see **Fig. 6.3**). The decomposition processes (Process 5 in **Fig. 6.4**) of the slump block are then induced by the fluvial erosion at the submerged surface of the slump block (see zone IV in **Fig. 6.2**). The erosion rate of slump block is calculated as

$$\varepsilon_{sb} = k_{sb} * \varepsilon \tag{6.10}$$

where $\varepsilon_{sb}$ and $\varepsilon$ are the fluvial erosion rate of the slump block and bank (m/s), respectively; and $k_{sb}$ is the coefficient of the fluvial erosion rate (1.2) that forced the best agreement between the calculated and measured streamwise average bank width because the coefficient of the fluvial erosion rate depends on the dynamics of slump blocks and flow characteristics (Motta et al., 2014).

### 6.2.4 Bedload Transport and Bed Deformation

Following fluvial erosion, cantilever failure, and slump block decomposition, the failure materials were dropped or forwarded into the bed channel, and were assumed to be non-cohesive materials and bedload (Process 6 in **Fig. 6.4**). The equations describing the bedload transport, and bed deformation are as follow.

The sediment transport rate in the streamwise direction ($q_{bs}$) was calculated using the formula proposed by Ashida & Michiue, (1972):

$$q_{bs} = 17\tau_*^{3/2}\left(1-\frac{\tau_{*c}}{\tau_*}\right)\left(1-\sqrt{\frac{\tau_{*c}}{\tau_*}}\right)\sqrt{Ggd_{50}^3} \tag{6.11}$$

where $\tau_*$ is the non-dimensional bed shear stress ($u_*^2/(G\,g\,d_{50})$), $u_*$ is the shear velocity ($\sqrt{g\,R_j\,i}$), $G$ is the specific weight of sediment (2.65), and $\tau_{*c}$ is the non-dimensional critical bed shear stress, using the formula of Iwagaki, (1956).

The sediment transport rate in lateral direction ($q_{bn}$) was calculated using the formula of Hasegawa, (1984) for distributing the failure sediments in the lateral direction by using the function of the bed elevation in the calculated cell ($Z_b$), and the coordinate components in the lateral axis (y) in each calculated grid cell and by neglecting the effect of secondary current as follows:

$$q_{bn} = -q_{bs}\sqrt{\frac{\tau_{*c}}{\mu_s\mu_k\tau_*}}\frac{\partial z_b}{\partial y} \tag{6.12}$$

where $\mu_s$ is the static friction coefficient (1.0), and $\mu_k$ is the kinetic friction coefficient (0.45).

The bed deformation was calculated using a continuity equation of sedimentation transport in an orthogonal coordinate and is expressed as

$$\frac{\partial Z_b}{\partial t} + \frac{1}{1-\lambda}\left(\frac{\partial q_{bn}}{\partial y}\right) = 0 \tag{6.13}$$

where $t$ is time and $\lambda$ is the porosity of the material (0.4).

## 6.3 RESULTS AND DISCUSSION

This section expresses and discusses the results between the computational and experimental results. The experiments were carried out in a fixed bed rectangular straight flume. The water and sediments were recirculated using a constant head tank of water placed at the upstream end of flume. Moreover, to reproduce a steady uniform flow, the water discharge remained constant at 6.45 l/s. The dimensions of the experimental flume were 0.8 m in width, 8.0 m in length and 0.4 m in height, and the channel slope was set 0.001. In the upstream region of the flume (0.0 to 3.0 m from the upstream), a wooden board was installed to avoid fluvial erosion. At the middle reach of the flume (3.0 to 5.0 m from the upstream), a cohesive bank was set. The cohesive bank was 0.5 m wide, 2.0 m long, and 0.2 m high. Downstream of the cohesive bank, a second wooden board was installed. The cohesive materials were composed of sand and silt with a mean diameter of 0.23 mm and 28.4 μm, respectively. The materials were well mixed by slowly adding water. The sediment mixtures were initially wetted with water to achieve a water content in a range of 32.2% and 39.6% for the silt-clay contents of 20% and 30% (see more details of the experimental setup in Chapter 5). The cohesive riverbank properties used in the experiments are summarized in Table 6.1.

Numerical simulations for duration of approximately 6 h (real time) were performed under the same conditions with the experimental studies. In **Fig. 6.6**, the numerical, and experimental results of the streamwise averaged bank width are compared with a perfect agreement line, which fell within the range of 15% error line in Case 1, and 10% error line in Case 2. The numerical results of Case 1 were approximately 1.2 times higher than the experimental results at the nearly equilibrium stage as a result of high bank protection of the armoring effect in the experimental flume. Moreover, the main error in Case 2 occurred from the fifth to seventh failures. The main reason of the overestimation is that the numerical model has the limitation of decomposing the large slump block volume (the fourth failure) on the bed channel.

The fluvial erosion rate in Case 1 (SC = 30%) was greater than that in Case 2 (SC = 20%) at 270 s, as shown in **Fig. 6.7**, indicating that banks with higher silt-clay content are more susceptible to failure than those with lower silt-clay content. The numerical results are consistent with the experimental results with regards to change the percentage of silt-clay content (Chapter 5). The observations of the this work were similar to the previous studies in term of changing silt-clay content (Couper, 2003; Dulal & Shimizu, 2010; Julian & Torres, 2006; Patsinghasanee et al., 2015b, 2015c). **Fig. 6.8** shows the comparison of the spatial-averaged bank width between the numerical results with, and without slump block consideration, together with the experimental results. The numerical results with slump block show good agreement with the experimental results. The results clearly show that the cantilever failures are suppressed by the effect of slump block. In contrast, the numerical results without slump block cannot replicate the complex mechanism of a cantilever failure. In terms of failure rate, the failure rate of experimental work (Case 1) is equal to 0.0025 cm/s (See **Fig. 6.8(a)**), whereas those in the numerical results with and without slump block consideration are 0.0023 and 0.005 cm/s, respectively. This is expressed that the failure rate in numerical modeling without slump block consideration is about two time larger than the numerical result with slump block consideration. In addition, the similar effects of slump block consideration are also showed in the numerical results of Case 2 (**Fig. 6.9(b)**). Therefore, the slump block effect on a cantilever failure model has highly significant effect for reproducing the coupling fluvial erosion and cantilever failure.

**Figs. 6.9(a)** and **6.9(c)** illustrate cross sectional views at the failure stages with a slump block, simulated using the present numerical model. These figures show the occurrence of fluvial erosion at

both slump block and bank in the submerged zone. This process occurs through the fluvial erosion at the slump block, and undermining of the bank. In present stage, the slump block was eroded on three sides (left, right and top sides). During slump block decomposition, the fluvial erosion rate of the bank is less than the initial rate as a result of the armoring effect (Crosato, 2008; Dulal & Shimizu, 2010; Motta et al., 2014; Parker et al., 2011). In contrast, in **Figs. 6.9(b)** and **6.9(d)**, the numerical model without the slump block effect cannot reproduce the complicated mechanisms of a cantilever failure. Additionally, the numerical results show the overestimated results in terms of the fluvial erosion and cantilever failure rates.

Beam-type failure is the dominated failure mechanism in the numerical results. The numerical results are similar with the experimental results, showing that the beam-type failure is the dominant failure mechanism. In addition, the width of overhanging block in the numerical results were within the range of 5.7 to 6.0 cm, while those in the experimental results are within the range of 5.7 and 14.3 cm. Therefore, this chapter can conclude that the simulated results were consistent with the experimental results (Chapter 5) in terms of the dimensions of overhanging blocks. Furthermore, the inclusion of slump block bank protection in a cross-sectional 2D model can capture the impact of slump blocks on channel evolution.

As in the numerical model, the present model is a cross-sectional 2D model. Such a model is limited in its ability to simulate the complex flow characteristics near the cohesive banks, non-uniform cantilever failure, the longitudinal gradient of sediment transport and pore water pressure. The proposed model should thus be improve in the future research.

Table 6.1 Summary of the existing large-scale experimental conditions.

| Case | Silt-clay contents (%) | Water content (%) | Cohesive force (kPa) | Internal friction angle (°) | Critical shear stress (kPa) | Erodibility coefficient ($m^3/(N\ s)$) |
|---|---|---|---|---|---|---|
| 1 | 30 | 39.6 | 5.76 | 34.3 | 0.57 | 105.6 |
| 2 | 20 | 32.2 | 6.41 | 41.3 | 0.38 | 42.8 |

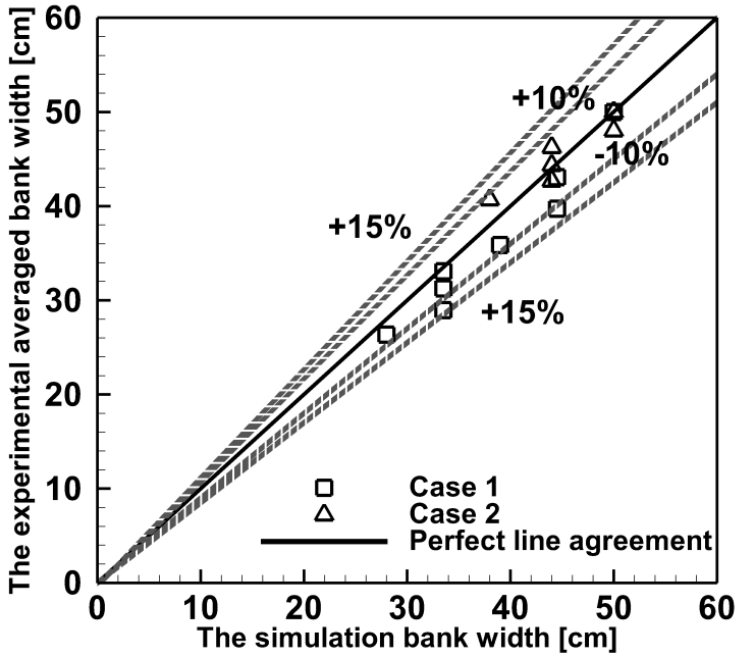


**Fig. 6.6** Comparison between numerical and experimental results in the streamwise averaged bank width.

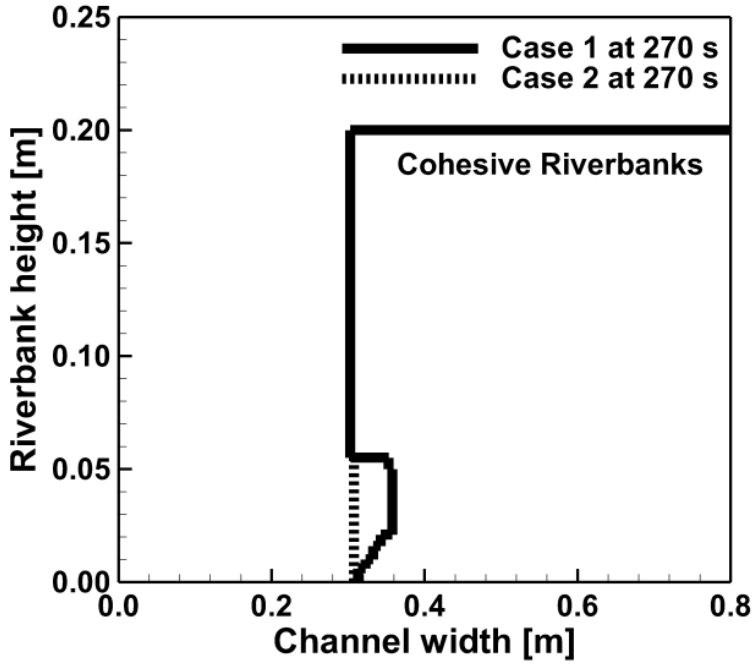


**Fig. 6.7** Riverbank geometry of the numerical results.

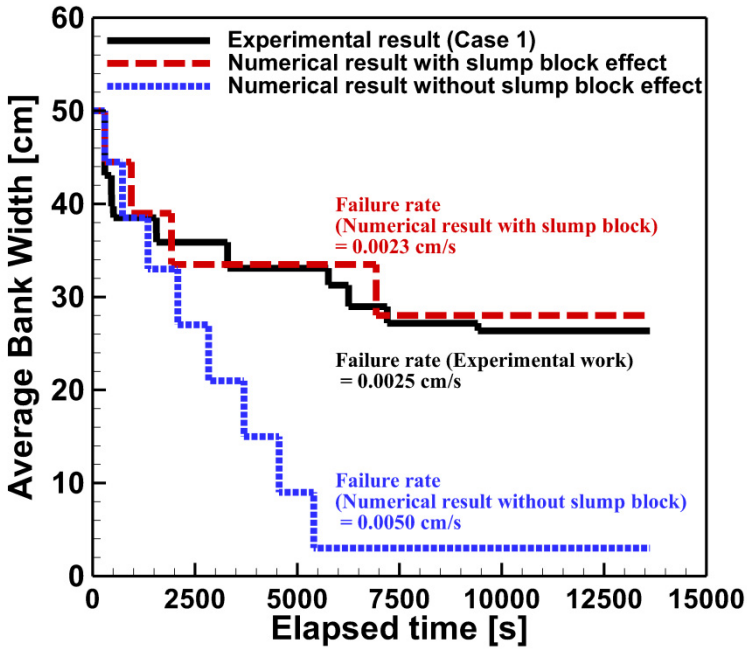


(a) Case 1.

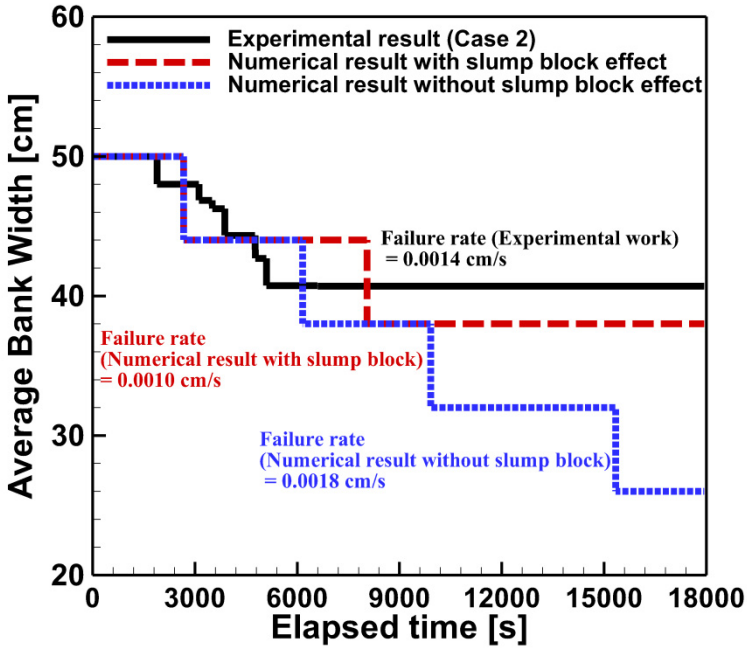


(b) Case 2.

**Fig. 6.8** Comparison of spatial-averaged bank width with and without slump block consideration, together with the experimental results.

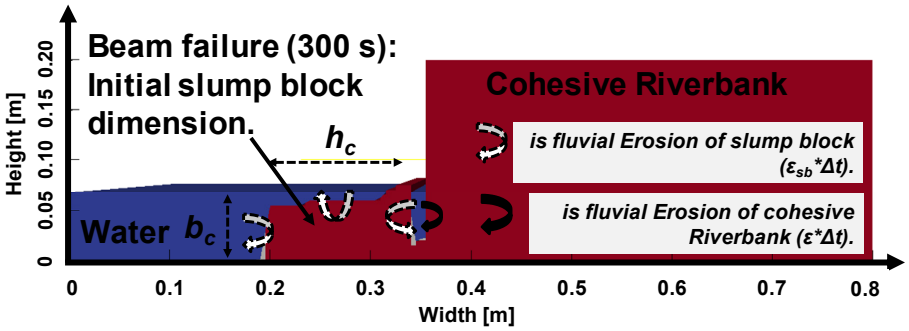


(a) Slump block on the bed channel after failure.

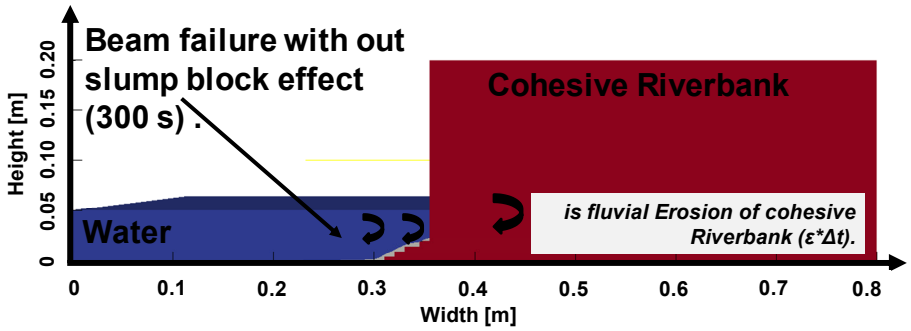


(b) No slump block on the bed channel after failure.

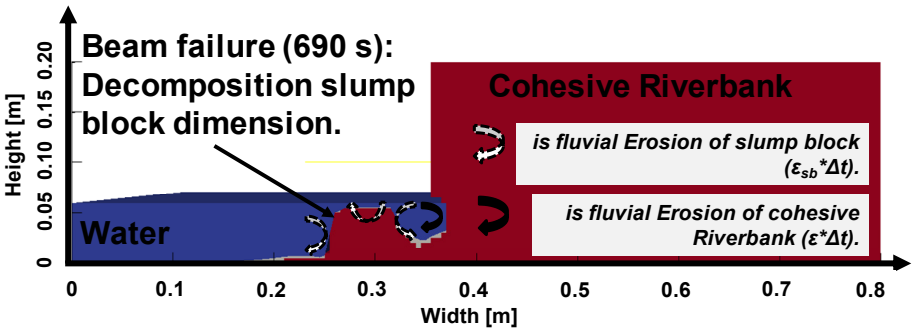


(c) Slump block decomposition on the bed channel.

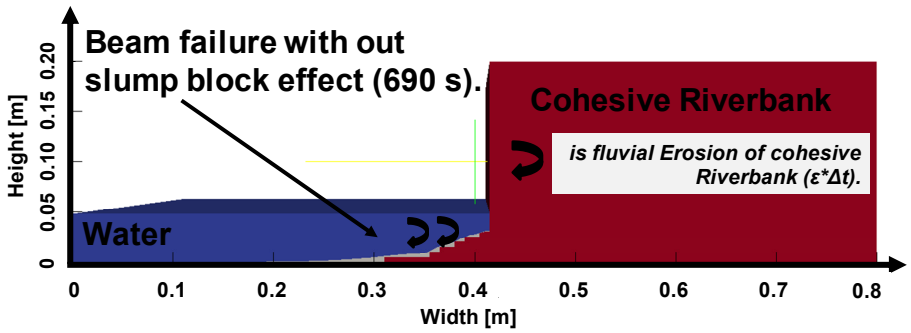


(d) No slump block decomposition on the bed channel.

**Fig. 6.9** Cross-sectional views of computational results in Case 1 with slump block effect (a and c), and without slump block effect (b and d) (brown: undisturbed cohesive material, gray: non-cohesive bedload, blue: water).

## 6.4 SUMMARY

The novel numerical modeling of the coupling fluvial erosion, cantilever failure, and slump block implemented by the triple-grid approach was developed in this study and was validated by the experimental results (Chapter 5). The main conclusion from the results are as follows.

The numerical modeling with slump block effects satisfactorily reproduced the fluvial erosion, cantilever failure, and bank protection by the slump blocks. Moreover, the numerical results showed good agreement with the experimental results in terms of the spatial-averaged bank width. On the other hand, the numerical results without slump block effects showed the excessive fluvial erosion and cantilever failure rates compared to the experimental results. Therefore, the effect of the bank protection due to the slump block are clearly demonstrated in this study. Additionally, the beam-type failure is the dominated failure mechanism in the numerical results. The numerical results are similar to the experimental results, showing that the beam-type failure is the dominant failure mechanism. In addition, the widths of overhanging block in the numerical results are consistent with those of the overhanging blocks in the experimental results. Furthermore, this study can conclude that the present numerical model is a powerful tool to analyze and predict the complex mechanism of a cantilever failure with slump blocks. Finally, the present numerical model still has limitations in simulating the complex flow characteristics near the cohesive banks, non-uniform cantilever failure, longitudinal gradient of sediment transport, a pore water pressure inside the banks. The proposed model might be highly important in improving future research, and to compare with natural rivers in terms of a cantilever failure with slump block process.

# Chapter 7

# CONCLUSIONS AND SUGGESTIONS FOR FUTURE RESEARCH

## 7.1 CONCLUSIONS

Riverbank failure is a key process in the river morphodynamic and can cause severe environmental and economic problems such as loss of agriculture area, destruction of infrastructures, turbidity problem, and sediment, nutrient and contaminant problems. However, because a cantilever failure involves a rapid channel widening and delivers a large volume of sediment into the channel, such a failure is a serious issue in river engineering. The complex mechanism of cantilever failure along cohesive riverbank have made the challenging research on riverbank failure processes. However, the available coupled methods for the analysis of fluvial erosion, cantilever failure, slump block effect and bedload sediment transportation are not sufficient to analyze and model the cohesive riverbank evolution processes. Since these methods have been originally developed for simple bank failure model ignoring overhanging formation, cantilever failure and slump block effect (for example, Dulal et al., 2010; Iwasaki et al., 2012; Jang & Shimizu, 2005; Nagata et al., 2000; Parker at al., 2011). During intermediate flow stage (not bank full stage), fluvial erosion does proceed and causes retreat of cohesive riverbank mainly thought a chain of fluvial erosion at the bank-toe, undercutting, tension crack, cantilever failure and slump block effect. Ignoring such processes in the computational processes of riverbank failure result in overestimation of riverbank migration.

This dissertation is a contribution to gain knowledge on riverbank failure processes including the simple riverbank failure mechanism of non-cohesive materials under homogeneous and heterogeneous conditions in the experimental scale (Patsinghasanee et al., 2014) and the coupled processes of fluvial erosion, tension crack, cantilever failure, slump block effect and bedload transportation of cohesive materials in the experimental flume (Patsinghasanee et al., 2015b, 2015c, 2016a, 2016b, 2016c) and the natural river (U-Tapao River, Thailand) (Patsinghasanee et al., 2015a, 2016d).

For simple riverbank failure mechanism, a numerical model for bed deformation and riverbank failure under homogenous and heterogeneous conditions was simulated to predict channel morphology processes by using a two-dimension boundary-fitted curvilinear coordinate system, an equilibrium sediment transport and a simple bank failure model. It was found that both grain size conditions can reproduce the experimental results by using an appropriate values of the angle of repose. It should be noted that a good agreement can be observed in homogeneous condition in the case of mild slope channel. In the heterogeneous condition, the results of bank erosion rate showed a satisfactory agreement with the experimental data but showed an unsatisfactory agreement for the bed deformation. This is a reason that the armoring effect is developed to protect bank erosion on the top of bank-toe after 60 minutes of simulation time (Patsinghasanee et al., 2014). Furthermore, the simple riverbank failure model was employed to simulate the cantilever failure mechanism of the experimental flume (Patsinghasanee et al., 2015b, 2015c). The comparisons showed that the

simplified model cannot reproduce the mechanism of cantilever failure, because the simple bank failure model does not consider the cantilever failure mechanism.

This study elucidated the complex mechanisms of cantilever failure by mean of laboratory experiment. The cohesive riverbanks were formed in the small-scale and large-scale experimental flumes with different percentages of silt-clay contents, water contents and hydraulic conditions (Patsinghasanee et al., 2015b, 2015c, 2016a, 2016c). The experimental results expressed that fluvial erosion at the submerged zone generates an overhanging block in the upper part of the cohesive riverbanks. Tension cracks then developed on the upper surface of the cohesive riverbanks and the cantilever failure after that occurred along the tension crack line. The dominant failure mechanism was observed to be beam-type failure, which was clarified by using the acceleration sensors installed inside the cohesive riverbanks. In addition, the experimental results indicated that cohesive riverbanks with higher silt-clay contents are more susceptible to failure than those with lower silt-clay contents. The slump block failure and decomposition phenomena were discussed for the first time with the cantilever failure experiments on channel flow. Slump blocks were observed on the bed channel in front of the riverbank, where they formed a sediment buffer that reinforced riverbanks and reduced fluvial erosion. The slump block phenomena for the formation and deformation showed a significant effect on the cohesive force of the riverbanks and affected the riverbank geometry. Therefore, a reduction of the silt-clay content leads to smaller slump block dimensions as well as faster decomposition. Moreover, the relationship between the slump block volumes and their decomposition times in the present study seems to be almost random, without any identifiable rules governing this phenomena.

The mechanisms of a cantilever failure were elucidated by means of the analytical study with the experimental results and the U-Tapao River, Thailand (Patsinghasanee et al., 2015a, 2016d). For fluvial erosion results, the comparison results of the erodibility coefficient ($k_d$) between the previous relationships and the experimental results showed a poor agreement. This is due to the fact that the previous equations were tuned under the natural river conditions, while the present study was conducted in the experimental channel. Moreover, the erodibility coefficient estimated by the previous equations and the measurements of the U-Tapao River gave the significantly different values because of the different material properties, covered vegetation, measured region of channel and consolidation load acted on the upper surface of the cohesive riverbank between the previous study areas and the U-Tapao River. Therefore, the relationship between the erodibility coefficient and the critical shear stress of this research indicated that they do not follow the previous relationships. As a result, the analysis of the erodibility coefficient and the critical shear stress specified that these parameters significantly vary from one site to another site. Thus, for the fluvial erosion estimation, the relationship of the erodibility coefficient and the critical shear stress are needed to be measured locally. For cantilever failure, the results showed that the dominant cantilever failure mechanisms of the experiment and the U-Tapao River are the beam-type failure and shear-type failure, respectively.

For numerical modeling, three series of cantilever failure model were developed in this dissertation. Firstly, a numerical model of cantilever failure was developed using a triple-grid approach to simulate the behavior of a cantilever within the framework of fluvial erosion and cantilever's subsequent failure. The simulated results show good agreement with the small-scale experimental results in terms of spatial-averaged bank width and water level along cohesive riverbank (Patsinghasanee et al., 2015b, 2015c). The second numerical model (Patsinghasanee et al., 2015a, 2016d) was then developed by employed the appropriate previous empirical and analytical equations of the actual shear stress, critical shear stress, fluvial erosion rate, erodibility coefficient, and factor of safety of shear-

type and beam-type failures. The second numerical results show better agreement than the first numerical result. This is due to the reason that the second numerical model employed the erodobility coefficient ($k_d$) from the experimental values. Additionally, the second numerical model can reproduce the first cantilever failure with high precision in terms of the occurred time and overhanging block width. For the first and second numerical model, the significant errors were occurred after the cantilever failure stage because the failure materials were dropped into channel and reinforced the riverbank from new fluvial erosion at the bank-toe. Therefore, the slump block effect is needed to consider in this study. After that, the third numerical modeling of a cantilever failure was developed using a triple-grid approach to simulate the behavior of a cantilever within the framework of fluvial erosion, the cantilever's subsequent failure, slump block effect and bedload sedimentation (Patsinghasanee et al., 2016b, 2016c). Two cases of cohesive materials in the large-scale experiment with the different percentages of silt-clay content were simulated under the similar hydraulic conditions with and without slump block consideration. The simulated results in terms of the fluvial erosion and cantilever failure showed significantly difference due to inclusion of slump block consideration. The third numerical model with slump block consideration satisfactorily reproduced the riverbank failure phenomena and showed good agreement with the large-scale experimental results in terms of the spatial-averaged bank width along the riverbanks. On the other hand, the numerical results without slump block effects showed the excessive fluvial erosion rate more than the large-scale experimental results. Therefore, the effects of the riverbank protection due to the slump block were clearly demonstrated in this study. Finally, this study can conclude that the third numerical model is a powerful tool to analyze and predict the complex mechanism of a cantilever failure with slump blocks.

## 7.2 SUGGESTIONS FOR FUTURE RESEARCH

### 7.2.1 Laboratory Measurement

For the investigation of the cantilever failure mechanism and the effect of pore water pressure distribution on the different types of fluvial erosion as well as cantilever failure, registering the time and dimensions of overhanging failure block are important issues. Therefore, it is suggested to increase the number of acceleration sensors installed inside the cohesive riverbank, especially in the upstream and downstream regions of the cohesive riverbank. Moreover, due to the lack of proper tool for observing the complex 3D geometries of cohesive riverbank, the 3D scanner is necessary to observe the cohesive riverbank geometry in the fluvial erosion, tension crack and cantilever failure. Finally, it is recommended to install mini-tensiometers in the overhanging zone of the cohesive riverbank to improve the understanding of the mechanism of cantilever failure in relation to the pore water pressure dynamic.

### 7.2.2 Numerical Modeling

The present model is a cross-sectional 2D model. Such a model is limited in its ability to simulate the complex flow characteristics near the cohesive riverbanks, non-uniform cantilever failure, the longitudinal gradient of sediment transport and pore water pressure. Therefore, a 2D depth-averaged model is needed to reproduce the complex mechanism of cantilever failure along a channel. The proposed model should thus be improve in the future research.

# APPENDIX A-PUBLICATION LISTS

Peer-Reviewed Papers:

1. Patsinghasanee, S., Kimura, I., and Shimizu Y. Experimental and numerical study on overhanging failure of river bank. *Journal of Japan Society of Civil Engineers, Ser. B1 (Hydraulic Engineering)*, Vol.70 No. 4, I_127-I_134, 2015. DOI.org/10.2208/jscejhe.71.I_127.

2. Patsinghasanee, S., Kimura, I., Shimizu, Y., and Nabi, M. Cantilever failure investigations for cohesive riverbanks. *Proceedings of the Institution of Civil Engineers - Water Management*, 2015, 1-16, 2015. DOI:10.1680/jwama.15.00033.

3. Patsinghasanee, S., Kimura, I., and Shimizu, Y. Coupled study of fluvial erosion and overhanging failure for cohesive riverbanks. *Journal of Japan Society of Civil Engineers, Ser. A2 (Applied Mechanics (AM))*, Vol.71 No.2 (Special Feature Vol.18), I_533-I_544, 2015. DOI.org/10.2208/jscejam.71.I_533.

4. Patsinghasanee,S., Kimura, I., Shimizu, Y., and Todate, T. Experimental investigation on cantilever failure for cohesive riverbanks. *Journal of Japan Society of Civil Engineers, Ser. B1 (Hydraulic Engineering)*, Vol.72 No. 4, I_769-I_774, 2016.

5. Patsinghasanee, S., Kimura, I., and Shimizu, Y. Numerical simulation of a cantilever failure with the effect of slump blocks for cohesive riverbanks. *Journal of Japan Society of Civil Engineers, Ser. B1 (Hydraulic Engineering)*, Vol.72 No. 4, I_493-I_498, 2016.

6. Patsinghasanee, S., Kimura, I., Shimizu, Y., Nabi, M. and Chup-Uppakarn T. Coupled studies of fluvial erosion and cantilever failure for cohesive riverbanks: Case studies in the experimental flumes and U-Tapao River. *Journal of Hydro-environment Research*, 2016. (**Submitted**)

7. Patsinghasanee, S., Kimura, I., Shimizu, Y., and Nabi M. Cantilever failure investigations with slump block effect for cohesive riverbank. *Journal of Hydraulic Research*, 2016. (**Submitted**)

Presentations on Conferences (as participant):

8. Patsinghasanee, S., Kimura, I., Shimizu, Y., and Hasegawa K. Computational modeling of bank erosion by a 2-D depth averaged model under homogeneous and heterogeneous conditions. *The 17th Applied Mechanics Symposium*, May 10-11, 2014, University of the Ryukyus, Okinawa, Japan.

9. 木村 一郎, Patsinghasanee, S. and 清水 康行. 河岸のオーバーハングと間欠的崩落を考慮した河岸浸食モデル. *土木学会第69回年次学術講演会(平成26年9月)*, September 10-12, 2014, Osaka University, Osaka, Japan.

10. Patsinghasanee, S., Kimura, I., Shimizu, Y., and Hasegawa, K. Computational modelling of bank erosion by a 2-D depth-averaged model under homogeneous and heterogeneous condition. *The 19th IAHR-APD Congress 2014*, September 21-24, 2014, Water Resources University, Hanoi, Vietnam.

11. Patsinghasanee, S., Kimura, I., and Shimizu, Y. Experimental and numerical study on overhanging failure of river bank. *The 59th Conference on Hydraulic Engineering*, March 10-12, 2015, Waseda University, Tokyo, Japan.

12. Patsinghasanee, S., Kimura, I., and Shimizu Y. An analytical approach to calculate the coupling fluvial erosion and overhanging failure of cohesive riverbanks. *The 18th Applied Mechanics Symposium*, May 10-11, 2015, Kanazawa University, Ishikawa, Japan.

13. Patsinghasanee, S., Kimura, I., Shimizu, Y., and Nabi, M. Experimental and numerical investigation of overhanging failures for cohesive riverbanks. *The 9th Symposium on River, Coastal and Estuarine Morphodynamics* (RCEM 2015), August 30 to September 3, 2015, Iquitos City, Peru.

14. Patsinghasanee, S., Kimura, I., and Shimizu, Y. Coupled studies of fluvial erosion and cantilever failure for cohesive riverbanks. *The 11th International Symposium on Ecohydraulics*, February 7-12, 2016, Melbourne, Australia.

15. Patsinghasanee,S., Kimura, I., Shimizu, Y., and Todate, T. Experimental investigation on cantilever failure for cohesive riverbanks. *The 60th Conference on Hydraulic Engineering*, March 14-16, 2016, Tohoku Institute of Technology, JAPAN.

16. Patsinghasanee, S., Kimura, I., and Shimizu, Y. Numerical simulation of a cantilever failure with the effect of slump blocks for cohesive riverbanks. *The 60th Conference on Hydraulic Engineering*, March 14-16, 2016, Tohoku Institute of Technology, JAPAN.

17. Patsinghasanee, S., Kimura, I., and Shimizu, Y. Experimental investigation of a cantilever failure for cohesive riverbanks. *The 13th International Symposium on River Sedimentation*, September 19-22, 2016, Stuttgart, Germany. **(Accepted)**

## REFERENCES


[1] Abam, T.K.S. Genesis of channel bank overhangs in the Niger Delta and analysis of mechanisms of failure. *Geomorphology,* 18(2)*,* 151-164, 1997. DOI:10.1016/S0169-555X(96)00010-4.

[2] Abe, Y., Takahashi, K., Hasegawa, K., and Nakanishi, S. Experiment on bed evolution with bank erosion of straight channel in the case of sediment diameter of mixture. *Proc. of the Hokkaido Branch, Japan Society of Civil Engineering*. 63, B-29 (CD-ROM), 2007. (in Japanese)

[3] Ajaz, A. *Stress-strain behaviour of compacted clays in tension and compression*, Ph.D. thesis*,* Department of Civil Engineering, Cambridge University, UK, 1973.

[4] Arimitsu, T., Ooe, K., Onda, S., Hosoda, T., and Shirai, H. Experimental and numerical investigation of river channel processes with bank erosion in steep curved channel. *Proc. of River, Coastal and Estuarine Morphodynamic: RCEM 2009-Vionnet et al. (eds.)*, 983-988, 2010.

[5] Arulanandan, K., Gillogley, E., and Tully, R. *Development of a quantitative method to predict critical shear stress and rate of erosion of natural undisturbed cohesive soils* (Rep. GL-8-3). Vicksburg, Miss: U.S. Army Engineer Waterways Experiment Station, 1980.

[6] Asada, H., and Ishikawa, H. Study on selective transportation of river material, *Central Research Institute of Electric Power Industry*, No.71015, 1972.

[7] ASCE (ASCE Task Committee on Hydraulics, Bank Mechanics, and Modeling of River Width Adjustment). River width adjustment. I: processes and mechanisms. *J. Hydraul. Eng.*, 124(9), 881-902, 1998. DOI:10.1061/(ASCE)0733-9429(1998)124:9(881).

[8] Ashida, K., and Michiue, M. Study on hydraulic resistance and bed-load transport rate in alluvial streams. *Proceedings of the Japan Society of Civil Engineers*, 206, 59-69, 1972. DOI:10.2208/jscej1969.1972.206_59. (in Japanese)

[9] ASTM D 2435-96. *Standard test method for one-dimension consolidation properties of soils*. ASTM International: West Conshohocken, PA, USA, 1-10, 1996.

[10] ASTM D 3080-98. *Standard test method for one-directional consolidation properties of soils*. ASTM International: West Conshohocken, PA, USA, 1-6, 1998.

[11] Bahar, S.M.H., and Fukuoka, S. Study of cohesive riverbank erosion mechanism through analysis of flow fields near and inside eroded bank. *Annual Journal of Hydraulic Engineering JSCE*, 46, 749-754, 2002.

[12] Blanckaert, K., Duarte, A., and Schleiss, A.J. Influence of shallowness, bank inclination and bank roughness on the variability of flow patterns and boundary shear stress due to secondary currents in straight open-channels. *Adv. Water Resour.*, *33(9)*, 1062–1074, 2010. DOI:10.1016/j.advwatres.2010.06.012.

[13] Chen, W. F., and Drucker, D. C. *Bearing capacity of concrete blocks or rock (69-1)*. Fritz Laboratory Reports. Paper 1993. http://preserve.lehigh.edu/engr-civil-environmental-fritz-lab-reports/1993, 1969.

[14] Couper, P. Effects of silt–clay content on the susceptibility of river banks to subaerial erosion. *Geomorphology*, 56(1-2), 95–108, 2003. DOI:10.1016/S0169-555X(03)00048-5.

[15] Crosato, A. *Analysis and modeling of river meandering,* Ph.D. thesis, Delft University of Technology, Delft, The Netherlands, 2008.

[16] Dapporto, S., Rinaldi, M., Casagli, N., and Vannocci, P. Mechanism of river failure along the Arno River, central Italy. *Earth Surf. Proc. Land.*, 28(12), 233-245, 2003. DOI: 10.1002/esp.550.

[17] Darby, S.E., Rinaldi, M., and Dapporto, S. Coupled simulations of fluvial erosion and mass wasting for cohesive river banks. *J. Geophys. Res. Earth Surf.*, 112, F03022. DOI:10.1029/2006JF000722, 2007.

[18] Department of Water Resources. *The master plan of integrated water resources management in the Songkhla Lake River Basin*. Department of Water Resources, Ministry of Natural Resources and Environment, Bangkok, Thailand, 2007. (in Thai)

[19] Duan, J.G. Analytical approach to calculate rate of bank erosion. *J. Hydraul. Eng.*, 131(11), 980-990, 2005. DOI: 10.1061/(ASCE)0733-9429(2005)131:11(980).

[20] Duan, J.G., and Julien, P.Y. Numerical simulation of meandering evolution. *J. Hydrol.*, 391(s1-2), 34-46, 2010. DOI:10.1016/j.jhydrol.2010.07.005.

[21] Dulal, K.P., Kobayashi, K., Shimizu, Y., and Parker, G. Numerical computation of free meandering channels with the application of slump blocks on the outer bends. *J. Hydro-environ. Res.,* 3(4), 239-246, 2010. DOI:10.1016/j.jher.2009.10.012.

[22] Dulal, K.P., and Shimizu, Y. Experimental simulation of meandering in clay mixed sediments. *J. Hydro-environ. Res*., 4(4), 329-343, 2010. DOI:10.1016/j.jher.2010.05.001.

[23] Eaton, B.C., Church, M., and Millar, R.G. Rational regime model of alluvial channel morphology and response. *Earth Surf. Proc. Land.*, 29(4), 511–529, 2004. DOI:10.1002/esp.1062.

[24] Engelund, F. Flow and bed topography in channel beds. *J.Hydraul.Div., Am. Soc. CivEng*, 100 (11), 1631-1648, 1974.

[25] Fang, H.Y., and Daniels, J.L. *Introductory Geotechnical Engineering: an Environmental perspective*, Taylor and Francis, London, UK, 2006.

[26] Fang, H.Y., and Hirst, T.J. A method for determining the strength parameters of soils. *Highway Research Record*, 463, 45-50, 1973.

[27] Francalanci, S., Bendoni, M., Rinaldi, M., and Solari, L. Ecomorphodynamic evolution of salt marshes: Experimental observations of bank retreat processes. *Geomorphology,* 195, 53–65, 2013. DOI:10.1016/j.geomorph.2013.04.026.

[28] Fukuoka, S. Erosion processes of natural river bank. *Proc. of the 1st Symposium on Hydraulic Measurement*, Beijing, China, 222-229, 1994.

[29] Fukuoka, S., Ishikawa, Y., Hibino, T., and Shimamoto, S. On the erosion and transportation in a channel formed with cohesive soil (gata soil). *Annual Journal of Hydraulic Engineering JSCE*, 40, 965-970, 1996. (in Japanese)

[30] Fukuoka, S., Watanabe, A., Katayama, T., et al. Erosion expansion mechanism of cohesive (silt) bank by the stream flow. *Annual Journal of Hydraulic Engineering JSCE*, 43, 695-700, 1999. (in Japanese)

[31] Fukuoka, S., Watanabe, A., Yamagata, S., and Kashiwagi, Y. Relation of flow velocity around riverbank and formation of overhanging bank. *Annual Journal of Hydraulic Engineering JSCE*, 44, 759-764, 2000. (in Japanese)

[32] Grabowski, R.C., Droppo, I.G., and Wharton, G. Erodibility of cohesive sediment: The importance of sediment properties. *Earth-Sci. Rev.*, 105(3-4), 101-120, 2011. DOI:10.1016/j.earscirev.2011.01.008.

[33] Hanson, G.J. Surface erodibility of earthen channels at high stresses: Part II. Developing an in situ testing device. *Transactions of the ASAE*, 33(1), 132-137, 1990. DOI:10.13031/2013.31306.

[34] Hanson, G.J., and Simon, A. Erodibility of cohesive streambeds in the loess area of the Midwestern USA. *Hydrol. Process.*, 15(1), 23-38, 2001. DOI:10.1002/hyp.149.

[35] Hagerty, D.J., Spoor, M.F., and Unrich, C.R. Bank failure and erosion on the Ohio River. *Engineering Geology*, 17(3), 141-158, 1981. DOI:10.1016/0013-7952(81)90080-6.

[36] Hasegawa, K. *Hydraulic research on planimetric forms, bed topographies and flow in alluvial river.* Ph.D. thesis, Hokkaido University, Sapporo, Japan, 1984. (in Japanese)

[37] Hooke, J.M. Magnitude and distribution of rates of river bank erosion. *Earth Surf. Proc. Land.*, 5(2)*,* 143–157, 1980. DOI:10.1002/esp.3760050205.

[38] Iwagaki, Y. Hydrodynamical study on critical tractive force. *Transactions of the Japan Society of Civil Engineers*, 41, 1–21, 1956. DOI:10.2208/jscej1949.1956.41_1. (in Japanese)

[39] Iwasaki, T., Shimizu, Y., and Kimura, I. Numerical simulation on bed evolution and channel migration in rivers. *Proc. of the the River Flow 2012-Murillo (eds.)*, 673-679, 2012.

[40] Jang, C.L., and Shimizu, Y. Numerical simulation of relative wide, shallow channels with erodible banks. *J. Hydraul. Eng.*, 131(7), 565-575, 2005. DOI:10.1061/(ASCE)0733-9429(2005)131:7(565).

[41] Julian, J.P., and Torres, R. Hydraulic erosion of cohesive riverbanks. *Geomorphology,* 76(1-2)*,* 193–206, 2006. DOI:10.1016/j.geomorph.2005.11.003.

[42] Julien, P.Y. *River mechanics.* Cambridge University Press, New York, USA, 2002.

[43] Kakinuma, T., and Shimizu, Y. Large-scale experiment and numerical modeling of a riverine levee breach. *J. Hydraul. Eng.*, 140(9), 04014039, 2014. DOI:10.1061/(ASCE)HY.1943-7900.0000902.

[44] Karmaker, T., and Dutta, S. Erodibility of fine soil from the composite river bank of Brahmaputra in India. *Hydrol. Process.*, 25(1), 104-111, 2011. DOI:10.1002/hyp.7826.

[45] Langendoen, E., and Alonso, C. Modeling the evolution of incised streams: I. Model formulation and validation of flow and streambed evolution components. *J. Hydraul. Eng.*, *134*, 749-762, 2008. DOI:10.1061/(ASCE)0733-9429(2008)134:6(749).

[46] Laubel, A., Kronvang, B., Hald, A.B., and Jensen, C. Hydromorphological and biological factors influencing sediment and phosphorus loss via bank erosion in small lowland rural stream in Denmark. *Hydrol. Process.*, 17(17), 3443-3463, 2003. doi:10.1002/hyp.1302.

[47] Lewin, J. Initiation of bed forms and meanders in coarse grained sediments. *Geol. Soc. Am. Bull.,* 87(2)*,* 281-285, 1976.

[48] Li, Y.T., Wang, F., Tang, J.W., and Zhu, L.L. Mechanism and prediction of bank failure. *Proc. of Advances in River Sediment Research-Fukuoka et al. (eds.)*, 21-34, 2013.

[49] Micheli, E.R., and Kirchner, J.W. Effects of wet meadow riparian vegetation on streambank erosion. 2. measurements of vegetated bank strength and consequences for failure mechanics. *Earth Surf. Proc. Land.*, 27(7), 687–697, 2002. doi:10.1002/esp.340.

[50] Muir, W.D. *Geotechnical modelling. Applied Geotechnics: Physical modelling*, Spon Press, London, UK, 2004.

[51] Motta, D., Langendoen, E.J., Abad, J.D., and Garcia, M.H. Modification of meander migration by bank failures. *J. Geophys. Res. Earth Surf.*, 199(5), 1026–1042, 2014. DOI: 10.1002/2013JF002952.

[52] Nagata, N., Hosoda, T., and Muramoto, Y. Numerical analysis of river channel processes with bank erosion. *J. Hydraul. Eng.*, 126(4), 243-252, 2000. DOI:10.1061/(ASCE)0733-9429(2000)126:4(243).

[53] Nakanishi, S., Hasegawa, K., and Takahashi, K. One-dimensional analysis of bed evolution accompanying bank erosion. *Proc. of River, Coastal and Estuarine Morphodynamic: RCEM 2005-Parker&Garcia (eds.)*, 937-942, 2006.

[54] Nardi, L., Rinaldi, M., and Solari, L. An experimental investigation on mass failures occurring in a riverbank composed of sandy gravel. *Geomorphology*, 163-164(Special issue), 56-69, 2012. DOI:10.1016/j.geomorph.2011.08.006.

[55] Nezu, I., Tominaga, A. and Nakagawa, H. Field measurements of secondary currents in straight rivers. *J. Hydraul. Eng.*, *119(5)*, 598–614, 1993. DOI:10.1061/(ASCE)0733-9429(1993)119:5(598).

[56] Onda, S., Shirai, H., Hosoda, T., Arimitsu, T., and Ooe, K. Numerical simulation of river channel processes with bank erosion in steep curved channel. *Proc. of River Flow 2010-Dittrich, Koll, Aberle&Geisenhainer (eds.)*, 993-1,000, 2010.

[57] Osman, A.M., and Thorne, C.R. Riverbank stability analysis. I: theory. *J. Hydraul. Eng.*, 114(2), 134-150, 1988. DOI:10.1061/(ASCE)0733-9429(1988)114:2(134).

[58] Parker, G., Shimizu, Y., Wilkerson, G.V., et al. A new framework for modeling the migration of meandering rivers. *Earth Surf. Proc. Land.*, 36(1), 70-86, 2011. DOI:10.1002/esp.2113.

[59] Partheniades, E. Erosion and deposition of cohesive soils. *J. Hydraul. Div. Am. Soc. Civ. Eng.*, 91, 105-139, 1965.

[60] Patsinghasanee, S., Kimura, I., and Shimizu, Y. Coupled study of fluvial erosion and overhanging failure for cohesive riverbanks. *Journal of Japan Society of Civil Engineers, Ser. A2 (Applied Mechanics (AM))*, Vol.71 No.2 (Special Feature Vol.18), I_533-I_544, 2015a. DOI.org/10.2208/jscejam.71.I_533.

[61] Patsinghasanee, S., Kimura, I., and Shimizu Y. Experimental and numerical study on overhanging failure of river bank. *Journal of Japan Society of Civil Engineers, Ser. B1 (Hydraulic Engineering)*, Vol.70 No.4, I_127-I_134, 2015b. DOI.org/10.2208/jscejhe.71.I_127

[62] Patsinghasanee,S., Kimura, I., Shimizu, Y., and Todate, T. Experimental investigation on cantilever failure for cohesive riverbanks. *Journal of Japan Society of Civil Engineers, Ser. B1 (Hydraulic Engineering)*, Vol.72 No.4, I_769-I_774, 2016a.

[63] Patsinghasanee, S., Kimura, I., and Shimizu, Y. Numerical simulation of a cantilever failure with the effect of slump blocks for cohesive riverbanks. *Journal of Japan Society of Civil Engineers, Ser. B1 (Hydraulic Engineering)*, Vol.72 No.4, I_493-I_498, 2016b.

[64] Patsinghasanee, S., Kimura, I., Shimizu, Y., and Hasegawa, K. Computational modelling of bank erosion by a 2-D depth-averaged model under homogeneous and heterogeneous condition. *Proc. of the 19th IAHR-APD Congress 2014*, Hanoi, Vietnam, 2014.

[65] Patsinghasanee, S., Kimura, I., Shimizu, Y., and Nabi, M. Cantilever failure investigations for cohesive riverbanks. *Proc. Inst. Civil. Eng.-Water Manag.*, 1-16, 2015c. DOI:10.1680/jwama.15.00033.

[66] Patsinghasanee, S., Kimura, I., Shimizu, Y., and Nabi, M. Cantilever failure investigations with slump block effect for cohesive riverbank. *J. Hydraul. Res.*, 2016c. (Submitted)

[67] Patsinghasanee, S., Kimura, I., Shimizu, Y., Nabi, M., and Chup-Uppakarn T. Coupled studies of fluvial erosion and cantilever failure for cohesive riverbanks: Case studies in the experimental flumes and U-Tapao River. *J. Hydro-environ. Res.*, 2016d. (Submitted)

[68] Peakall, J., Ashworth, P.J., and Best, J.L. Meander-bend evolution alluvial architecture, and the role of cohesion in sinuous river channel: a flume study. *J. Sediment. Res.,* 77(3), 197-212, 2007. DOI:10.2110/jsr.2007.017.

[69] Reneau, S.L., Drakos, P.G., Katzman, D., et al. Geomorphic controls on contaminant distribution along an ephemeral stream. *Earth Surf. Proc. Land.*, 29(10), 1209–1223, 2004. DOI:10.1002/esp.1085.

[70] Rinaldi, M., and Darby, S.E. *Advances in modelling river bank erosion process, In Gravel-Bed Rivers 6: From Process Understanding to River Restoration. Series Development in Earth Surface Processes-Habersack, H., Piégay, H., and Rinaldi, M., (eds.)*, Elsevier, The Netherland, 213-239, 2008.

[71] Rinaldi, M., Mengoni, B., Luppi, L., et al. Numerical simulation of hydrodynamics and bank erosion in a river bend. *Water Resour. Res.*, 44(9),W09428, 2008. DOI:10.1029/2008WR007008.

[72] Rinaldi, M., and Nardi, L. Modeling interactions between riverbank hydrology and mass failures. *J. Hydraul. Eng.*, 18(10), 1231-1240, 2013. DOI:10.1061/(ASCE)HE.1943-5584.0000716.

[73] Samadi, A., Amiri-Tokaldany, E., Dovoudi, M.H., and Darby, S.E. Identifying the effects of parameter uncertainty on the reliability of modelling the stability of overhanging, multi-layered, river banks. *Geomorphology*, 134(3-4), 483-498, 2011. DOI:10.1016/j.geomorph.2011.08.004.

[74] Samadi, A., Amiri-Tokaldany, E., Dovoudi, M.H., and Darby, S.E. Experimental and numerical investigation of the stability of overhanging riverbanks. *Geomorphology,* 184, 1-19, 2013. DOI:10.1016/j.geomorph.2012.03.033.

[75] Schumm, S.A. Fluvial geomorphology in river mechanics. *Water Resources Publication*, Fort Collins, CO, USA, 365-395, 1971.

[76] Schumm, S.A. Patterns of alluvial rivers. *Annu. Rev. Earth Planet. Sci.*, 13, 5-27, 1985.

[77] Semmad, S. *Stability study of U-Tapao riverbank, Songkhla Province*. Master thesis, Department of Civil Engineering, Prince of Songkla University, Thailand, 2010. (in Thai)

[78] Shimada, T., Watenabe, Y., Yokoyama, H., & Tsuji, T. An experiment on overflow-induced cross-levee breach at the Chiyoda Experimental Channel. *Proc. of River, Coastal and Estuarine Morphodynamic: RCEM 2009-Vionnet et al. (eds.)*, 475-481, 2009.

[79] Smerdon, E.T., and Beasley, R.T. Critical tractive forces in cohesive soils. *Agricultural Engineering*, 42(1), 26-29, 1961.

[80] Sturm, T.W. *Open channel hydraulic: Uniform flow*. McGraw-Hill, Singapore, 2001.

[81] Sutarto, T., Papanicolaou, A.N., Wilson, C.G., and Langendoen, E.J. Stability analysis of semicohesive streambanks with CONCEPTS: Coupling field and laboratory investigations to quantify the onset of fluvial erosion and mass failure. *J. Hydraul. Eng.* 140, 2014. DOI:10.1061/(ASCE)HY.1943-7900.0000899.

[82] Taghavi, M., Dovoudi, M.H., Amiri-Tokaldany, E., and Darby, S.E. An analytical method to estimate failure plane angle and tension crack depth for use in riverbank stability analyses. *Geomorphology*, 123(1-2), 74-83, 2010. DOI:10.1016/j.geomorph.2010.06.017.

[83] Terzaghi, K., Peck, R.B., and Mesri, G. *Soil Mechanics in Engineering Practice*, 3rd edn. Wiley, New York, USA, 1996.

[84] Thoman, R.W., and Niezgoda, S.L. Determining erodibility, critical shear stress, and allowable discharge estimation for cohesive channels: case study in the Power River Basin of Wyoming. *J. Hydraul. Eng.*, 134(2), 1677-1687, 2008. DOI:10.1061/(ASCE)0733-9429(2008)134:12(1677).

[85] Thorne, C.R., and Abt, S. Analysis of riverbank instability due to toe scour and lateral erosion. *Earth Surf. Proc. Land.*, 18(9), 835–843, 1993. DOI:10.1002/esp.3290180908.

[86] Thorne, C.R., and Tovey, N.K. Stability of composite river banks. *Earth Surf. Proc. Land.*, 6(5), 469–484, 1981. DOI:10.1002/esp.3290060507.

[87] Vanoni, V.A. *Sedimentation Engineering ASCE*. New York, USA, 1977.

[88] Watanabe, A., Fukuoka, S., Yasutake, Y., and Kawaguchi, H. Groin arrangements made of natural willows for reducing bed deformation in curved channel. *Advances in River Engineering*, 7, 285-290, 2001. (in Japanese)

[89] Wood, A. L. *A geomorphological analysis of bank toe processes: The fate of failed blocks stored in the basal zone of incised channels,* Ph.D. thesis, University of Nottingham, Nottingham, England, 2001.

[90] Wood, A. L., Simon, A., Downs, P. W. & Thorne, C.R. Bank-toe processes in incised channels: The role of apparent cohesion in the entrainment of failed bank materials. *Hydrol. Process.*, 15(1), 39–61, 2001. DOI:10.1002/hyp.151.

[91] Wynn, T. *The effects of vegetation on streambank erosion*. Ph.D. thesis, Department of Biological Systems Engineering, Virginia Tech, Blacksburg, Va, USA, 2004.

[92] Yalin, M.S., and Karahan, E. Inception of sediment transport. *J. Hyd. Div. ASCE.*, 105(11), 1433-1443, 1979.

[93] Zhang, R.J., Xie, J.H., Wang, M.F., and Huang, J.T. Dynamic of fluvial sediment transport, *China Water Power Press*, 1989. (in Chinese)